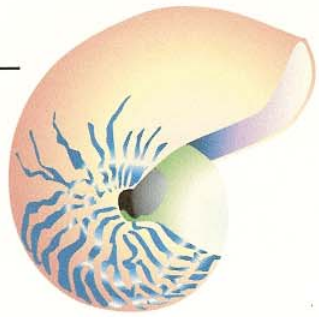

Coastal Marine Institute

University of Alaska

# Sea Ice-Ocean-Oilspill Modeling System (SIOMS) for the Nearshore Beaufort and Chukchi Seas: Parameterization and Improvement (Phase II)


Jia Wang
Principal Investigator

Co-principal Investigators:
Kohei Mizobata
Meibing Jin
Haoguo Hu


Final Report
OCS Study MMS 2008-021

February 2010


**Minerals Management Service**
**Department of the Interior**

**and the**

**School of Fisheries & Ocean Sciences**

**University of Alaska Fairbanks**

This study was funded in part by the U.S. Department of the Interior, Minerals Management Service (MMS) through Cooperative Agreement No. 1435-01-02-CA-85294, Task Order No. 35407 and No. 1435-01-98-CA-30909, Task Order No. 15178, between MMS, Alaska Outer Continental Shelf Region, and the University of Alaska Fairbanks.

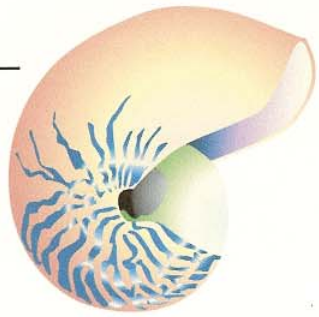

Coastal Marine Institute

University of Alaska

# Sea Ice-Ocean-Oilspill Modeling System (SIOMS) for the Nearshore Beaufort and Chukchi Seas: Parameterization and Improvement (Phase II)


Jia Wang
Principal Investigator

Co-principal Investigators:
Kohei Mizobata
Meibing Jin
Haoguo Hu


Final Report
OCS Study MMS 2008-021

February 2010


**Minerals Management Service**
**Department of the Interior**

**and the**

**School of Fisheries & Ocean Sciences**

**University of Alaska Fairbanks**

**Contact Information**

email: sharice@sfos.uaf.edu
phone: 907.474.7208
fax: 907.474.7204
postal: Coastal Marine Institute
School of Fisheries and Ocean Sciences
University of Alaska Fairbanks
Fairbanks, AK 99775-7220

## Table of Contents

## List of Figures

## List of Tables

## Project Summary

This report describes our Coastal Marine Institute Minerals Management Service research project and its accomplishments during the last three-year funding period, May 2004-April 2007. The following has been accomplished. 1) We developed and implemented a Sea Ice-Ocean-Oilspill Modeling System (SIOMS) that consists of a 3.8-km, 3-D Coupled Ice-Ocean Model (CIOM) and a 2-D ice-associated oilspill model. 2) We improved the CIOM by implementing tides and its mixing, and parameterizations for lateral melting and wind-wave mechanical mixing. 3) The CIOM was validated using both in situ observations and satellite measurements. 4) Model integrations were conducted using both monthly atmospheric forcing for seasonal climatology and daily forcing for year-to-year variability from 1990 to 2006. 5) We conducted simulations of oilspill trajectories released on Prudhoe Bay landfast ice region on March 15, 2002. 6) Sensitivity experiments were conducted with regard to the impacts of the Bering Strait inflow, onshore wind stress, lateral melting parameterization, and tides on the sea ice and coastal ocean current, in particular on the landfast ice, in the nearshore Chukchi and Beaufort seas.

The 3.8-km CIOM successfully reproduces many observed phenomena in the region, including the Bering-inflow-originated coastal current that splits into three branches: Alaska Coastal Water (ACW), Central Channel, and Herald Valley branches. Other phenomena include the Beaufort Slope Current (BSC), the Beaufort Gyre, the East Siberian Current (ESC), mesoscale eddies, seasonal landfast ice, sea ice ridging, shear, and deformation. Many of these downscaling processes can only be captured by using a high-resolution CIOM, nested in a global climate model.

The seasonal cycles for sea ice concentration, thickness, velocity, and other variables are well reproduced with solid validation by satellite measurements. The seasonal cycles for upper ocean dynamics and thermodynamics are also well reproduced, which include the formation of the cold saline layer due to the injection of salt during sea ice formation, the BSC, and the subsurface upwelling in winter that brings up warm, even more saline Atlantic Water along the shelfbreak and shelf along the Beaufort coast. The CIOM also reproduces reasonable interannual variability in sea ice, such as producing anomalous open water (less sea ice) during the positive Dipole Anomaly (DA) years, vice versa during the negative DA years. The year-to-year variability in ocean circulation and thermodynamics can be also fairly reproduced.

Sensitivity studies show the CIOM responds reasonably well to the change in important parameters (such as lateral melting, albedo, etc.) and processes (nonlinear terms, tides, wind forcing, Bering inflow, or boundary conditions). Furthermore, the experiments show that landfast

ice and the coastal current system are determined by wind, lateral melting, the Bering inflow, and other parameters as well.

It was learned that a 3.8-km mesh might be the limit for the isotropic sea ice model with viscous-plastic rheology. An algorithm solution to sea ice dynamics (such as explicit scheme) with EVP (elastic-viscous-plastic) and a better model representation of anisotropic property of sea ice should be explored to advance high resolution sea ice modeling.

## 1. Introduction

The Beaufort and Chukchi seas (Figure 1) are an important region where North Pacific water via the Bering Strait encounters the Western Arctic water with seasonal ice in the Chukchi Sea, and both seasonal and perennial ice in the Beaufort Sea. The Chukchi Sea is mainly featured by the continental shelf, while the Beaufort Sea is characterized by a relatively narrow continental shelf and a deep basin with a narrow, steep shelf slope. More importantly, the Beaufort Sea also features continuous landfast ice along the Alaska Arctic coast, parallel to the 20-m isobath (Eicken et al. 2005). In comparison, the landfast ice along the western Alaska coast in the Chukchi Sea is discontinuous. All these features have challenged both observationalists and modelers.

The ocean circulation system in the Beaufort and Chukchi seas is very complex and consists of the Bering inflow that separates into three branches: ACW, Central Channel and Herald Valley branches (see Figure 1). There are the anticyclonic Beaufort Gyre, the Beaufort Slope Current (BSC), and the East Siberian Current (ESC). The BSC has a spatial scale of about several dozen kilometers (Weingartner et al. 1998; Pickart 2004), and Barrow Canyon Current has a similar spatial scale of about 30 km (Shimada, personal comm.). Another important feature in the Beaufort Sea is the small-scale mesoscale eddies of several dozen kilometers in diameter (Manley and Hunkins 1985; Muench et al. 2002; Chao and Shaw 2002), with anticyclones outnumbering the cyclones. Again, these small-scale features challenge both observation and modeling capability. Particularly, coarse resolution observation arrays and model meshes cannot resolve these processes.

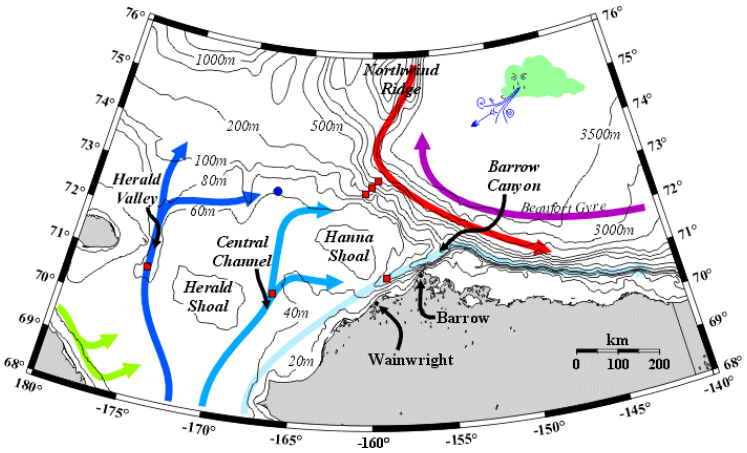


**Figure 1. A schematic diagram for coastal circulation in the Chukchi-Beaufort Seas (light blue: Alaskan Coast Current with the origin of freshwater; Courtesy of Tom Weingartner).**

In the shallow Chukchi Sea, tidal current and its mixing should be important (Nihoul et al. 1993; Kowalik and Proshutinsky 1994). The wind-derived surface waves are also important mechanical sources to vertical mixing. These dynamic sources should be seriously taken into account in both observational and modeling studies.

The winter atmospheric wind pattern is mainly controlled by the anticyclonic (clockwise) Beaufort High, while the summer wind stress is relatively weak due to the weakened Beaufort High. The northward propagating summer storms occasionally move to the Chukchi Sea via the Bering Strait (Zhang et al. 2004), producing strong wind and mixing. The winter anticyclonic wind stress associated with the Beaufort High has many important effects, such as 1) surface Ekman drift that advects the Beaufort coastal freshwater into the Beaufort Gyre (Yang 2006), 2) sub-surface upwelling that brings the warm, saline Arctic intermediate water (i.e., the Atlantic Water) into the Beaufort Sea shelf break, melting surface sea ice (Melling 1993), and 3) formation of landfast ice (Mahoney et al. 2007a, b).

An ocean-only model for the Bering-Chukchi shelves was developed during the Inner Shelf Transfer and Recycling in the Bering-Chukchi Seas (ISHTAR) Program by Nihoul et al. (1993). Though the ISHTAR model included both tidal and wind forcing, the deep basin was excluded (i.e., the Alaskan Stream, Bering Slope Current, Alaskan Coastal Current, and Kamchatka Current were excluded). Thus the heat and freshwater fluxes were neglected, leaving much to understand concerning this ocean system. Because Nihoul et al. used an ocean-only model, the simulation was conducted only in the ice-free seasons (spring-summer). There is no seasonal cycle simulation available for a realistic study of biological cycling. A biological-physical model was also developed, based on Nihoul's ocean model, by Shuert and Walsh (1993). The model had the same domain as Nihoul's model, but was confined to the northern Bering Sea and southern Chukchi Sea shelves, again without ice. The shelf break processes and the exchange between the deep basin and continental slope were also ignored as well as other important processes, such as upwelling and mesoscale eddies. The full seasonal cycle of the ecosystem has not yet been simulated.

In the Chukchi Sea and the Western Arctic Ocean, extensive interdisciplinary surveys were conducted under the National Science Foundation Shelf-Basin Interactions (SBI) project in the last several years (Grebmeier et al. 2006). These datasets are available for model-data comparison.

Idealized ocean only modeling was conducted by Winsor and Chapman (2004) to study mechanisms of how wind stress affects the Chukchi Sea current system. An early study by Rutgers University, supported by MMS, also used an ocean only model to simulate ocean circulation in the Beaufort and Chukchi seas. Due to coarse resolution models and other factors, many of the phenomena mentioned above were not resolved.

In general, most sea-ice models on basin scales use relatively simple thermodynamics and ice thickness distributions. These models approximate sea ice as slabs of one to a few mean thicknesses and open water (Hibler 1979; Wang et al. 1994a). While sufficient for simulating Arctic Ocean pack ice for climate study purposes, most present models lack the ability to sufficiently resolve the spectrum of ice thickness from thin, new ice to thick, ridged ice, or to resolve landfast ice anchored along the coast. Wang et al. (2002a, 2005) developed a pan-Arctic Coupled Ice-Ocean Model with a resolution of 27.5km, which, of course, is not sufficient to resolve coastal processes and its dynamics.

During 2000-2003, MMS/CMI sponsored a research task titled “Nowcast/Forecast Model-Beaufort Sea Ice-Ocean-Oilspill System (NFM-BSIOS)” (Wang et al. 2002b, 2003a). This model uses 3.8km resolution grids for both ocean and sea ice. Sea ice is categorized into seven types, from thin to thick (Yao et al. 2000). The preliminary results show the model’s potential to study coastal sea ice and ocean dynamics (Wang et al. 2003a). However, because the nested domain is relatively small, the ability of the model to deal with coastal circulation variability and landfast ice is still not satisfactory. Much has been learned since.

A workshop on small-scale Sea Ice and Ocean Modeling for the nearshore Beaufort and Chukchi seas was held at the International Arctic Research Center of the University of Alaska Fairbanks (IARC/UAF) during August 7-9, 2002. The workshop produced a working plan for small-scale ice-ocean modeling over the next five years. The recommendations are summarized as follows (Wang 2003; Wang el al. 2003b):

1) Although a viscous-plastic (VP) ice model is generally good for large-scale climate modeling, the recommendation is that an elastic plus VP (EVP) ice model (Hunke and Dukowicz 1997) would be better for both large-scale and small scale modeling.
2) Sea ice distribution for ridged ice and rafted ice should be used to better study sea ice of different types (multiple categories such as new ice, first year ice, and multi-year ice).
3) Landfast ice is crucial to the coastal processes. Thus, landfast ice models including scouring and anchoring processes should be developed. At the same time, parameterization of landfast ice is also necessary.
4) Discontinuous Lagrangian ice models such as granular models should be compared to the continuum models such as Eulerian (VP and EVP) models to find out the advantages and disadvantages of each.
5) As spatial scale becomes less than 10km, satellite observations show that sea ice has a strong anisotropic property, whereas most models used so far are isotropic. Thus, anisotropic models should be developed to better capture sea ice properties such as sea ice fractures, stresses, ridging, rafting, etc.

6) A coupled ocean-ice model should consider mixing by ocean tides and surface waves. The coupling of sea ice stress and convergence/divergence to the upper ocean (imbedded vs. levitated ice) should be taken into account (Hibler and Bryan 1987). A turbulence closure model should be implemented in the ocean model.
7) Ocean model resolution has to be eddy resolving to resolve coastal eddies, upwelling/downwelling, dense water formation (Wang et al. 2003c), and the Arctic halocline ventilation.
8) For climate atmosphere-sea ice-ocean models with a grid size larger than 10km, a parameterization of 10km processes for an anisotropic model is necessary.

During 2004-2007, MMS/CMI continuously sponsored this project titled “Sea Ice-Ocean-Oilspill Modeling System for the Nearshore Beaufort and Chukchi Seas: Parameterization and improvement (Phase II).” The goal of this project was to build a state-of-the-art, stand-alone coupled ice-ocean model to resolve many of these important small-scale dynamic and thermodynamic features of both the ocean circulation and sea ice. The end-product is to provide ocean and sea ice information to MMS to conduct hypothetical oilspill impact assessments on the environment in the Beaufort and Chukchi seas. This final report summarizes major accomplishments in the last three years.

## 2. Model description

This coupled ice-ocean model was described in great detail in the model development and application to the pan-Arctic region (Wang et al. 2002a). In the following, we only describe the parts necessary for the completeness of this report.

### *2.1 Sea-ice model*

The sea ice component of the coupled model is a thermodynamic model based on multiple categories of ice thickness distribution function (Thorndike et al. 1975; Hibler 1980) and a dynamic model based on a viscous-plastic sea ice rheology (Hibler 1979).
The evolution of the thickness distribution function satisfies a continuity equation

$$\frac{\partial g}{\partial t} + \nabla \cdot (\vec{V} g) = -\frac{f g}{\partial h} + \psi \qquad (1)$$

where $\vec{V}$ is velocity vector (*u, v*), ***f(h)*** is the thermodynamic vertical growth rate of ice, ***g*** is the sea ice thickness distribution function, and ***g(h)dh*** is defined as the fraction of area covered by

the ice with thickness between ***h*** and ***h***+***dh***. The averaged thickness $\bar{h}$ and concentration ***A*** of sea ice in a grid is expressed from **g(*h*)** as

$$A = \int_{0+}^{h} g(h)dh \qquad (2)$$

and

$$\bar{h} = \int_{0}^{h} g(h)hdh \qquad (3)$$

**ψ** is the mechanical redistribution function, which represents the creation of open water and ridging during ice deformation. The redistribution process conserves ice volume. The redistribution function is parameterized as described by Yao et al. (2000). The vertical growth rate ***f(h)*** of ice thickness is determined by the ice thermodynamics.

The model thermodynamic interactions between ice, ocean, and atmosphere are shown in Fig. 2. The heat budget on the upper ice surface is

$$Q_{AI}=Q_{Si}+Q_{Ei}+Q_L+(1-\alpha_i)I_0-\varepsilon_i\sigma T_0^4 \qquad (4)$$

where $\alpha_i$ is the albedo of sea ice (0.75 during the freezing period from October to March, 0.65 during the melting period from April to September). When snow exists, ice albedo is replaced by the snow albedo $\alpha_S$ (0.9); $\varepsilon_i$ is the emissivity of ice. $I_0$ is the short wave solar radiation reaching the ice surface; $Q_{Si}$, $Q_{Ei}$ , and $Q_L$ are the sensible heat flux, the

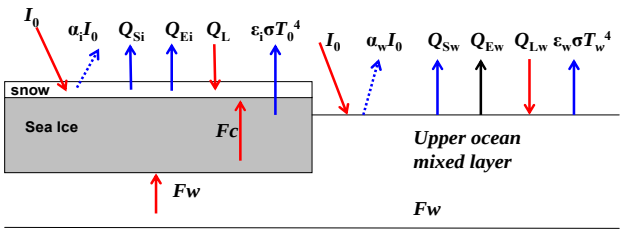


**Figure 2. Interactions among the air, ice, and ocean system in terms of heat budget.**

latent heat flux, and the effective longwave radiation flux from ice surface, respectively. $Q_{Si}$, $Q_{Ei}$ and $Q_L$ are parameterized by the following formulae,

$$Q_{Si} = \rho_a C_p C_s |\vec{V}_a|(T_a - T_0) \qquad (5)$$

$$Q_{Ei} = \rho_a Le Ce |\vec{V}|(q_a - q_0) \quad (6)$$

$$Q_L = \varepsilon_a \sigma[(1-k_c C_L)(a-b\sqrt{e_a})T_a + 4(T_0 - T_a)]T_a^3 \quad (7)$$

where $q_a$ and $T_a$ are the specific humidity and air temperature of air; $q_0$ is the saturated specific humidity on ice; $T_0$ is the surface ice temperature; $e_a$ is the atmospheric vapor pressure. $C_p$ is the specific heat of air at constant pressure. $Le$ is the latent heat sublimation on the ice surface. $Cs$ and $Ce$ are the sensible heat and latent heat bulk transfer coefficients, respectively. $\varepsilon_a$ is the emissivity of air. $\sigma$ is Stefan-Boltzmann constant. $k_c$ is the cloud factor, and $C_L$ is the cloud fraction. $T_a$ (in Kelvin) is the air temperature, $a$ and $b$ are empirical constants ($a$=0.254, $b$=4.95×10$^{-3}$). The surface ice temperature $T_0$ is determined from the surface heat balance equation,

$$Q_{AI} - Q_c = 0 \quad (8)$$

where $Q_c$ is the internal conductive heat flux through ice. A linear ice temperature profile and a constant thermal conductive coefficient $k_i$ are used in this study. Thus, for the ice category with thickness $h$,

$$Q_c = -k_i(T_0 - T_f)/h \quad (9)$$

where $T_f$ is the freezing temperature of seawater on bottom ice surface, which is a function of the salinity of seawater (=-0.0544$S_0$+273.15$K$, where $S_0$ is the salinity of upmost ocean grid, in practical salinity unit, psu). For the snow-covered ice, the conductive coefficient will be replaced by $\frac{k_i k_s}{h k_s + h_s k_i}$, where $h_s$ is the snow depth.

If the calculated $T_0$ is found to be over 0$^oC$, it is forced to be 0$^oC$. The extra heat of equation (8) is used to melt the ice at the upper surface, and the melted water will drain to the ocean immediately. The volume flux of melting water $W_{AI}$ is

$$W_{AI} = [Q_{AI} - Q_c]/L \quad (10)$$

The growth rate at the bottom of the sea ice is

$$W_{IW} = [Q_c - F_T]/L \quad (11)$$

where $L$ is the volume latent heat of fusion, and $F_T$ is the oceanic heat flux out of the ocean surface (assumed to be uniform over a model grid cell). Thus, the growth rate $f(h)$ for sea ice with thickness $h$ is the sum of (10) and (11), i.e.

$$f(h) = (Q_{AI} - F_T)/L \quad (12)$$

For the open water in the ice zone, the growth rate of sea ice is

$$W_{AW}=(Q_{AW}-F_T)/L \qquad (13)$$

where $Q_{AW}$ is the heat budget between the atmosphere-ocean interface, excluding the solar radiation that is absorbed in the water column. $Q_{AW}$ is calculated using a similar parameterization to (4) but without the solar radiation terms, i.e.

$$Q_{AW}=Q_{Sw}+Q_{Ew}+Q_{Lw}-\varepsilon_w\sigma T_w^4 \qquad (14)$$

where $\varepsilon_w$ is the emissivity of water. $T_w$ is the sea surface temperature (SST). $Q_{Sw}$, $Q_{Ew}$, and $Q_L$ are the sensible heat flux, the latent heat flux, and the effective longwave radiation flux from water surface, which are parameterized similar to formulae (5)-(7). When the $W_{AW}$ is negative, the "melting" of ice to water is implied. In this case, the equivalent heat is redistributed to melt the remaining ice. The total ice growth rate is integral over various ice thicknesses with weight $g(h)$.

The ice velocity $\vec{V}$ $(u_I, v_I)$ is determined from the momentum equation

$$m\frac{d\vec{V}}{dt}+mf\vec{k}\times\vec{V}=-mg\nabla H+\vec{\tau}_a-\vec{\tau}_w+\vec{F} \qquad (15)$$

or in terms of scalar format,

$$\frac{\partial u_I}{\partial t}+u_I\frac{\partial u_I}{\partial x}+v_I\frac{\partial u_I}{\partial y}-fv_I=-g\frac{\partial H}{\partial x}+\frac{\tau_{ax}}{\rho_I}-\frac{\tau_{Wx}}{\rho_I}+\frac{F_x}{\rho_I}$$

$$\frac{\partial v_I}{\partial t}+u_I\frac{\partial v_I}{\partial x}+v_I\frac{\partial v_I}{\partial y}+fu_I=-g\frac{\partial H}{\partial y}+\frac{\tau_{ay}}{\rho_I}-\frac{\tau_{Wy}}{\rho_I}+\frac{F_y}{\rho_I}$$

where $f$ is the Coriolis parameter, and $m$ is the ice mass in a grid. $\nabla H$ is the gradient of sea surface elevation, $\vec{F}$ is the internal stresses (see Hibler 1979; Wang et al. 1994a), and $\vec{\tau}_a$ and $\vec{\tau}_w$ are the air and water stresses, respectively. They are determined by the bulk formulae

$$\vec{\tau}_a=\rho_a C_a|\vec{V}_a|\vec{V}_a \qquad (16)$$

$$\vec{\tau}_w=\rho_w C_w|\vec{V}_w-\vec{V}_i|(\vec{V}_w-\vec{V}_i) \qquad (17)$$

where $\vec{V}_a$ is the wind velocity vector. $\vec{V}_w$ is the current velocity vector of the upmost ocean layer. $C_a$ (=1.2×10$^{-3}$) and $C_w$ (=5.5x10$^{-3}$ ) are the bulk coefficients of wind stress and water stress, respectively. $\rho_a$ is the air density, and $\rho_w$ the seawater density. $\vec{F}$ is the two-dimensional

internal ice stress tensor, which is derived from the viscous plastic rheology with elliptical yield curve rate ***e***=2 of Hibler (1979) and involves a compressive ice strength

$$P=P^{*}\,\bar{h}\,\exp[-C(1-A)] \qquad (18)$$

where ***P**** and ***C*** are empirical constants (here $2.5\times10^{4}\mathrm{Nm}^{-2}$ and 20, respectively). ***e*** is the ratio of principal axes of the ellipse, $P^{*}$ is the ice strength, and ***C*** is the ice strength decay constant. This formulation requires that the ice strength strongly depends on the amount of thin ice, characterized by ***(1-A)***, which also allows the ice to strengthen as it becomes thicker, as measured by thickness $\bar{h}$. The redistribution function is parameterized as described by Thorndike et al. (1975) and Yao et al. (2000), differing from the treatment by Hibler (1980), who used a given thickness to ridged ice of a single thickness (the multiplication factor is chosen as 15). Table 1 lists the parameters, their values and units that are used in this model.

**Table 1. Constants used in CIOM**

(Note temperature is in Kelvin, $^{0}$K, $0\,^{0}$C=273.15 $^{0}$K)

| Symbols | Description | Values | Units |
|---|---|---|---|
| a | empirical constant | 0.254 | |
| b | empirical constant | $4.95\times10^{-3}$ | |
| $\alpha_i$ | albedo of sea ice | 0.65-0.75 | |
| $\alpha_S$ | albedo of snow | 0.9 | |
| $\alpha_w$ | albedo of sea water | 0.1 | |
| C | ice decay constant | 20 | |
| $C_a$ | wind stress bulk coef. | $1.2\times10^{-3}$ | |
| $C_w$ | water stress bulk coef. | $5.5\times10^{-3}$ | |
| $C_e$ | latent heat bulk transfer coef. | $1.75\times10^{-3}$ | |
| $C_S$ | sensible heat bulk transfer coef. | $2.32\times10^{-3}$ | when Ts<Ta |
| | | $1.75\times10^{-3}$ | when Ts>=Ta |
| $C_P$ | specific heat of air | 1410 | $\mathrm{J\,kg^{-1}\,K^{-1}}$ |
| $C_{P,W}$ | specific heat of sea water | 3903 | $\mathrm{J\,kg^{-1}\,K^{-1}}$ |

| | | | |
|---|---|---|---|
| e | yield curve eccentricity | 2 | |
| $e_i$ | emission of sea ice | 0.65-0.75 | |
| L | volume latent heat of fusion | | |
| $L_e$ | latent heat sublimation on ice surface | $3.32 \times 10^{-3}$ | J $kg^{-1}$ |
| k | von Karman constant | 0.4 | |
| $k_C$ | cloud factor | 0.62 | |
| $k_i$ | thermal conductive coef. | 2.04 | |
| $P^*$ | ice strength | $2.5 \times 10^4$ | $Nm^{-2}$ |
| Pr | molecular Prantl number | 12.9 | |
| $\rho_a$ | air density | 1.3 | kg $m^{-3}$ |
| $\rho_i$ | sea ice density | 910 | kg $m^{-3}$ |
| $\rho_w$ | seawater density | 1025 | kg $m^{-3}$ |
| $S_I$ | sea ice salinity | 5 psu | |
| Sc | Schmidt number | 2432 | |
| $\sigma$ | Stefan-Boltzmann constant | $5.67 \times 10^{-8}$ | |
| $\Delta x=\Delta y$ | model horizontal grid size | 3800 | m |
| $\Delta T$ | time step for eternal mode | 20 | seconds |
| $\Delta t$ | time step for internal mode and ice | 400 | seconds |

In this sea ice model, we introduced a thermodynamical process: lateral melting, which relates to a variable of the bulk heat transfer coefficient, $\boldsymbol{K_b}$, depending on wind speed proposed by Ohshima and Nihashi (2005).

$$K_b = C_h u_* \qquad (19)$$

$$u_* = \sqrt{C_d}\, u_{rel} \qquad (20)$$

where $\boldsymbol{C_h}$ and $\mathbf{u}_*$ are the heat transfer coefficient and friction velocity, respectively. $\mathbf{u}_*$ is derived from (20) using drag coefficient $\boldsymbol{C_d}$ and relative velocity $\boldsymbol{u_{rel}}$ (1 % of geostrophic wind velocity). The melting resulting from heat input by wind is expressed as

$$\frac{dC}{dt} = -\frac{C_w \rho_w K_b C(T_0 - T_f)}{L \rho_i h_0} \quad (21)$$

Note that the lateral melting is about twice as large as bottom melting during the melting season. The parameters used in the CIOM along with their units are listed in Table 1.

### *2.2 Ocean model*

The Princeton Ocean Model (Blumberg and Mellor 1987; Mellor 2004; Wang 2001) is used as the ocean component of the coupled mode in this study. The model has a free surface, uses sigma coordinates in the vertical, and employs a mode-split technique. The model embeds a second-order turbulence closure sub-model. Smagorinsky diffusivity along sigma surfaces is employed in the horizontal diffusion.

The governing equations of ocean dynamics in Cartesian-coordinate are as follows:

$$\frac{\partial u}{\partial t} + u\frac{\partial u}{\partial x} + v\frac{\partial u}{\partial y} + w\frac{\partial u}{\partial z} - fv = -g\frac{\partial \eta}{\partial x} + \frac{\partial}{\partial x}(A_H \frac{\partial u}{\partial x}) + \frac{\partial}{\partial y}(A_H \frac{\partial u}{\partial y}) + \frac{\partial}{\partial z}(A_Z \frac{\partial u}{\partial z})$$

$$\frac{\partial v}{\partial t} + u\frac{\partial v}{\partial x} + v\frac{\partial v}{\partial y} + w\frac{\partial v}{\partial z} + fu = -g\frac{\partial \eta}{\partial y} + \frac{\partial}{\partial x}(A_H \frac{\partial v}{\partial x}) + \frac{\partial}{\partial y}(A_H \frac{\partial v}{\partial y}) + \frac{\partial}{\partial z}(A_Z \frac{\partial v}{\partial z})$$

$$\frac{\partial u}{\partial x} + \frac{\partial v}{\partial y} + \frac{\partial w}{\partial z} = 0$$

The temperature and salt equations in sigma-coordinates are

$$\frac{\partial T}{\partial t} + \nabla \cdot (\vec{V}_w T) + \frac{\partial \omega T}{\partial \sigma} = \frac{\partial}{\partial \sigma}(K_H \frac{\partial T}{\partial \sigma}) + F_T - (1-\alpha_w)\frac{\partial I_0}{\partial \sigma} \quad (22)$$

$$\frac{\partial S}{\partial t} + \nabla \cdot (\vec{V}_w S) + \frac{\partial \omega S}{\partial \sigma} = \frac{\partial}{\partial \sigma}(K_H \frac{\partial S}{\partial \sigma}) + F_S \quad (23)$$

and the surface heat flux is

$$Q_{AW} = Q_{Sw} + Q_{Ew} + Q_{Lw} - \varepsilon_w \sigma T_w^4 \quad (24)$$

in the ice-free grid cell , and

$$AF_T + (1-A)Q_{AW} \quad (25)$$

in the ice-covered grid cell.

### *2.3 Ice-ocean coupling*

Heat and salt fluxes at the ice-ocean interface are governed by the boundary processes as discussed by Mellor and Kantha (1989). The new level 2.5 closure turbulence model is employed

according to Kantha and Clayson (1994). In grid cells in which ice is present, the heat flux out of the ocean is

$$F_T=-\rho_w C_p C_{Tz}(T_f-T) \qquad (26)$$

where $C_p$ is the specific heat of seawater, and $T$ is the ocean temperature at the uppermost model grid (in our model the midpoint of the uppermost ocean layer). The heat transfer coefficient $C_{Tz}$ is given by

$$C_{Tz}=\frac{u_*}{P_{rt}\ln(-z/z_0)/k+B_T} \qquad (27)$$

$$B_T=b(z_0u_*/v)^{1/2}P_r^{2/3}$$

where $u_*$ is the friction velocity, $P_{rt}$ is a turbulent Prantl number, $z$ is the vertical coordinate corresponding to the temperature $T$, $z_0$ is the roughness length, and $k$ is the von Karman constant. The molecular sublayer correction is represented by $B_T$ where $P_r$ is a molecular Prantl number, $v$ is the kinematic viscosity, and $b$ is an empirical constant (= 3). The salt flux out of the ocean is

$$F_S=(W_{AI}+W_{IW}+W_{AW})(S_I-S)+(1-A)S(P-E) \qquad (28)$$

where $S_I$ is the salinity of ice (=5 psu), $S$ is the salinity at the uppermost model grid point, and $(P-E)$ is the volume flux of precipitation minus evaporation.

Analogous to the heat flux (26), the salt flux is defined as

$$F_S=-C_{Sz}(S_0-S) \qquad (29)$$

where $S_0$ is the salinity at the ice-ocean interface. The salt transfer coefficient $C_{Sz}$ is

$$C_{Sz}=\frac{u_*}{P_{rt}\ln(-z/z_0)/k+B_S} \qquad (30)$$

$$B_S=b(z_0u_*/v)^{1/2}Sc^{2/3}$$

where $Sc$ is the Schmidt number. Since $Sc$ =2432, and $P_r$=12.9, and $C_{Tz}>C_{Sz}$, this can lead to the production of frazil ice in the water column as discussed by Mellor and Kantha (1989). Frazil ice is immediately added to the floating ice.

The ice-water stress is

$$\tau_w/\rho_w=\frac{ku_*}{\ln(z/z_0)}(\vec{V}_i-\vec{V}_w)$$

where $\vec{V}_w$ is the ocean velocity vector at the uppermost model grid.

### *2.4 Configuration of high-resolution CIOM and atmospheric forcing*

The CIOM should refer to the studies of Yao et al. (2000) and Wang et al. (2002a, b; 2003a, b; 2004, 2005). The ocean model used is the Princeton Ocean Model (POM) (Mellor 2004), and the ice model used is a full thermodynamic and dynamics model (Hibler 1980) that prognostically simulates sea-ice thickness, sea ice concentration (SIC), ice edge, ice velocity, and heat and salt flux through sea ice into the ocean. The model has been successfully applied to the Bering Sea (Hu and Wang 2008; Wang et al. 2008), the Beaufort Sea (Wang et al. 2003d), and in the northern China seas (Q. Liu, personal comm.).

**Ocean Model:**

- horizontal spherical grid with 3.8 km resolution in longitude and latitude covering the Chukchi-Beaufort seas;
- 24 sigma levels in the vertical;
- open boundaries (velocity, T, and S) are embedded by a climate (atmosphere-ice-ocean-land) GCM from Japan with a resolution of about 25 km (Watanabe et al. 2006) with volume transport conservation principle and radiation property (Wang et al. 2001a).
- river runoff is applied at the mouth of the Mackenzie River (Wang et al. 1999);
- inclusion of parameterization of wind-wave mechanic mixing;
- atmospheric forcing uses National Centers for Environmental Prediction (NCEP) Reanalysis products: heat flux, mass (moisture) flux, and six-hourly wind stress.

**Ice Model:**

- full thermodynamics with 2-layer ice and 1-layer snow;
- full dynamics with plastic-viscous rheology (Hibler 1979, 1980; Wang et al. 1994a) under the NCEP forcing;
- multi-category ice model (Thorndike et al. 1975; Yao et al. 2000) fully coupled to an ocean model (Mellor and Kantha 1989; Kantha and Clayson 1994);
- inclusion of lateral melting of sea ice (Ohshima and Nihashi 2005);
- prognostic and diagnostic variables: Ice velocity, compactness, ice edge, thickness, heat budget, salt budget, ice stress, etc.

In this study, ten ice categories (0, 0.2, 0.5, 1, 1.5, 2, 3, 4, 5, and 6 m) are used, each having a percentage in a grid point. Thus, a thickness equation for each category is calculated. Then, the summation of each category thickness is the total thickness at each grid. Thus, sea ice

concentration and thickness at each grid are calculated from the sum of the ten ice categories.

The model was spun up with the PHC temperature and salinity (Steele et al. 2001), sea ice climatology, January concentration, and motionless sea ice and ocean for the first four years under NCEP reanalysis monthly atmospheric forcing, which were derived from 1958 to 1997. At the bottom layer, both temperature and salinity are restored to the monthly climatology with the same time scale of 60 days. At the surface, salinity, with freshwater flux forcing from *P-E*, is restored to the observed monthly salinity fields at a time scale of 30 days for prescribing freshwater runoff into the Arctic Basin using the flux correction method of Wang et al. (2001a). After a four-year spinup, a dynamic and thermodynamic seasonal cycle is established. Then, we re-ran the model for another four years using the fourth year output as the restart or initial conditions. During the four-year run, all the monthly atmospheric forcings remain the same. Then, the last year variables are used for examining the seasonal cycle in this study. We also use the daily NCEP forcing to drive the CIOM from 1990 to 2006 for year-to-year variability.

## 3. Description of observations

### 3.1 JAMSTEC (**J**apan **A**gency for **M**arine-earth **S**cience and **TEC**hnology) observations

JAMSTEC conducted its field campaigns with *R/V Mirai* in the Beaufort and Chukchi seas, as a bi-annual expedition (Figure 3). Data collection includes ship-board CTD, towed ADCP, moored ADCP, CTD, current meters, and biogeochemical sensors (http://www.jamstec.go.jp/arctic). The data we show here are from 1992 to 2000. The data after 2000 will be analyzed after we have permission. These data are used as independent observations to validate the CIOM.

### 3.2 Satellite measurements

Satellite remotely sensed datasets were employed to validate the CIOM. To compare the sea ice area, we used the sea ice concentration maps derived from the Special Sensor Microwave Imager (SSM/I) on board the Defense Meteorological Satellite Program (DMSP) F-13. This product is available at the National Snow and Ice Data Center (NSIDC) website (http://nsidc.org/data/sea_ice.html#SEA_ICE_CONCENTRATION). There are two algorithms for sea ice concentration: the NASA team algorithm (Cavalieri et al. 1990) and the Bootstrap

algorithm (Comiso 1990). The NASA team algorithm takes into account the multi-year ice fraction, while the Bootstrap algorithm assumes open water and ice.

**Figure 3. JAMSTEC observation stations.**

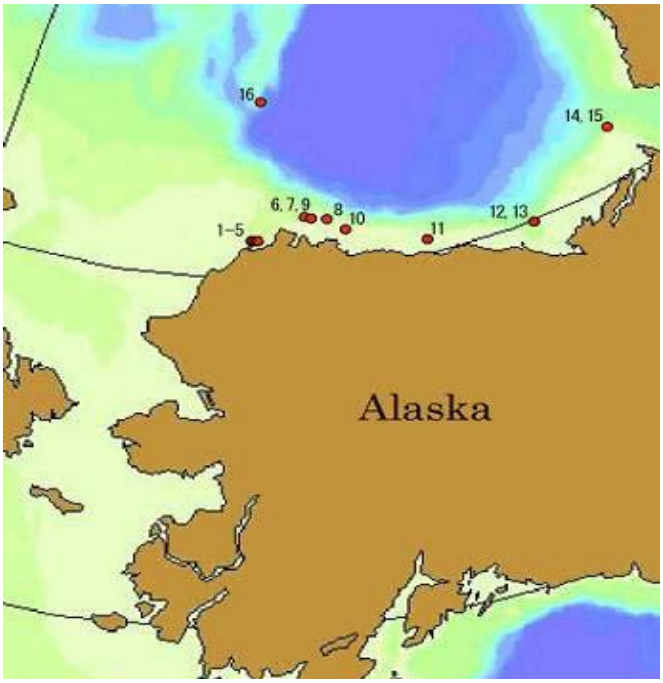


1-5: CBJ92—CBJ96 (Head of Barrow Canyon)
6: CBE96 (Mouth of Barrow Canyon)
7: CBE99 (Mouth of Barrow Canyon)
8: CBW96 (Mouth of Barrow Canyon)
9: CBE00 (Mouth of Barrow Canyon)
10: BFK98 (Beaufort Sea)
11: BFS98 (Beaufort Sea)
12: MCJ99 (Mackenzie Canyon)
13: MCJ00 (Mackenzie Canyon)
14: AGJ99 (Mouth of Amundsen Gulf)
15: AGJ00 (Mouth of Amundsen Gulf)
16: NWR97 (Northwind Ridge)

In this project, the NASA team algorithm was selected to evaluate sea ice concentration from 1998 to 2005. Horizontal resolution is 25 km. Map projection is the polar stereographic. Extraction of data and converting from the Polar stereographic projection to the cylindrical projection (9 km) were done using Interactive Data Language (IDL).

To compare the CIOM temperature field with the satellite dataset, we used the AVHRR Oceans Pathfinder Global 4 km Equal-Angle All SST V5 (Vazquez et al. 1998) provided by the NASA/Jet Propulsion Laboratory/Physical Oceanography Distributed Active Archive Center (PO. DAAC; http://podaac.jpl.nasa.gov). The accuracy of this pathfinder SST is 0.3$^{o}$C. Horizontal resolution is 4 km. We also utilized the Moderate Resolution Imaging Spectroradiometer (MODIS) Level 3 mapped standard product suite SST. Data processing was conducted by the SeaWiFS Data Analysis System (SeaDAS 5.0; ttp://oceancolor.gsfc.nasa.gov/seadas/, Fu et al. 1998).

## 4. Model simulations: Climatology with monthly forcing and with no lateral melting

The CIOM was driven by the NCEP/NCAR Reanalysis monthly atmospheric forcing (air temperature, humidity, sea surface wind, sea level pressure, latent heat flux, sensible heat flux, net shortwave radiation, net long wave radiation and precipitation rate). Those atmospheric datasets were derived from the NOAA/CDC/NCEP/NCAR website (http://www.cdc.noaa.gov/cdc/reanalysis/reanalysis.shtml).

### 4.1 General ocean circulation pattern vs. in situ observations

The high resolution CIOM reproduced very fine structure of the Alaskan Coastal Current system (three branches) and the anticyclonic large-scale Beaufort Gyre superimposed by mesoscale eddies with anticyclones outnumbering cyclones (Figure 4). The first branch is the Alaska Coastal Water branch along the Alaska Arctic coast. This current flows mainly along the isobaths with relatively warm water, hugging to the Alaska coast. The second branch (middle) flows northward along the Central Channel and turns to the east, joining ACW/C. The ACW flows eastward all the way to the Canadian Beaufort Sea, encountering the Mackenzie River outflow, where the coastal current then turns sharply to the west and joins the Beaufort Gyre (westward) circulation. As a consequence, between the Beaufort Gyre and ACW current there is a strong horizontal shear, resulting in a deep trough in sea surface height (SSH). This phenomenon is found for the first time using this high resolution CIOM, and needs field measurements to confirm its existence. The third branch flows northwestward into the Chukchi Sea via a deep channel between the Wrangel Island and Herald Shoal. Part of this current turns to the east and joins the BSC (Pickart 2004). In addition, the ESC is also reproduced. These features are consistent with recent observations in the region (Woodgate et al. 2005).

The simulated Beaufort Gyre is confirmed by the high SSH (red) with anticyclones dominating due to baroclinic instability (Wang and Ikeda 1997; Chao and Shaw 2002). However, it is not well known whether or not the barotropic instability play a role in triggering mesoscale eddies. Thus, barotropic instability also deserves further investigation.

**Figure 4. Model-simulated upmost 50-m averaged ocean velocity on July 10 under climatological forcing, compared with the schematic ocean circulation pattern (imbedded on the lower right corner; courtesy of Weingartner). In the left panel, the color bar indicates the sea level height (SSH) with red being high SSH, while in the right panel, the color bar denotes the bottom topography in meters with red being shallow water.**

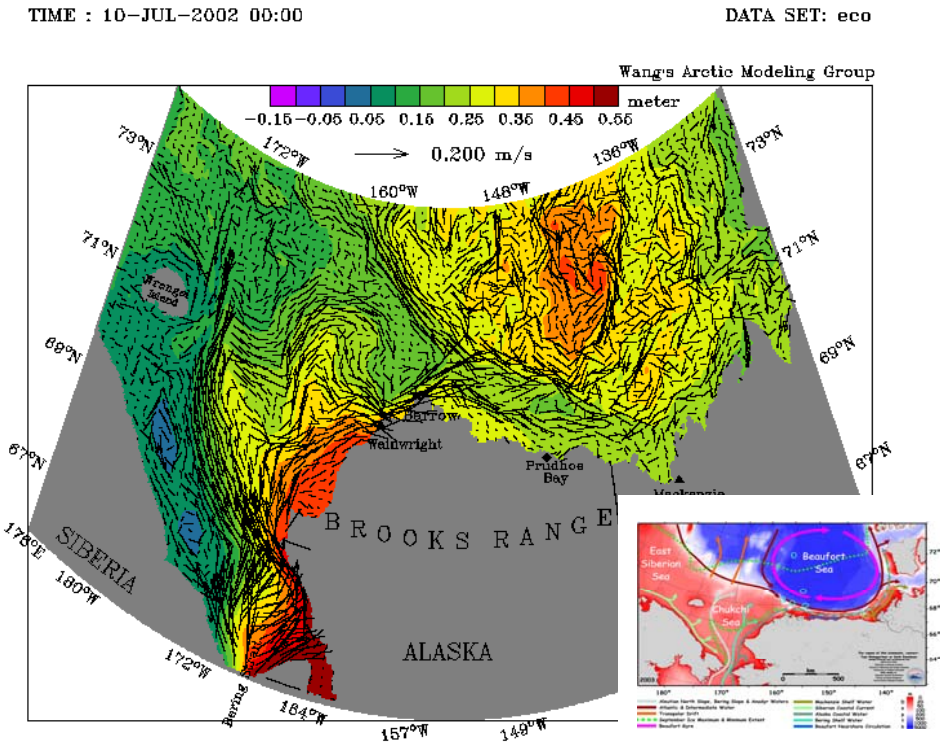


Sea Surface Elevation and Circulation

**Figure 5. Climatological annual mean velocity reproduced by the model (black arrows) are compared to the JAMSTEC ADCP- measured velocity (red arrows) at the 70 m depth in the Beaufort and Chukchi seas.**

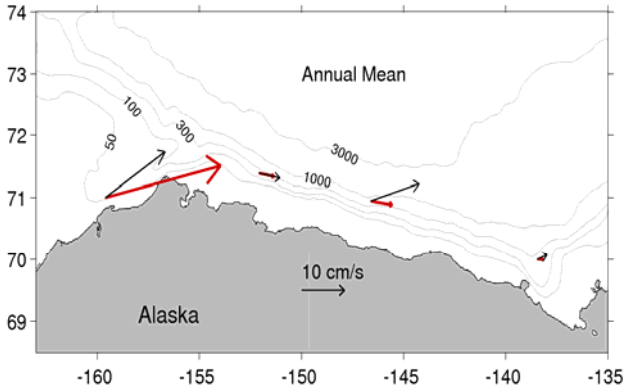


Both in-situ and satellite remote sensed data are used to validate the Beaufort Sea CIOM. Figure 5 shows the comparison between the model simulation velocity (black) and the ADCP mooring velocity (red) at a subsurface layer of 70 m. The ADCP data were taken from 1992 to 2001 by JAMSTEC. The simulated velocities are, in general, consistent with the observed. Nevertheless, there are discrepancies in both direction and magnitude, which may be due to the following facts: 1) the model topography/depth was smoothed, 2) the model vertical and horizontal resolution is still coarse, and 3) the model forcing is climatological monthly forcing, while the observations were taken from 1992 to 2001 by JAMSTEC. Therefore, simulations from year to year (such as from 1990 to present) under the daily forcing are necessary to objectively evaluate the model simulation skills.

We further validate the CIOM using historical transitional CTD measurements. There were several observational campaigns in the region by JAMSTEC, NSF's Shelf-Basin Interactions in the Western Arctic (SBI) project (Pickart 2004), Canadian Beaufort Sea project (Melling 1993) , and MMS-sponsored Beaufort Sea oceanographic survey (Weingartner et al. 1998) and landfast ice survey (Eicken et al. 2005). Comparisons were conducted using these available data.

Figure 6 shows a transect comparison off Barrow Canyon in the Chukchi Sea. In section 3 (see the inserted map in the lower left corner), the summer observations show that there is a very saline, thick subsurface layer (see the inserted map at the lower right corner), thought to be the winter dense water that can survive summer (Weingartner et al. 1998). Our model-simulated the monthly salinity maps show that in summer (see August and September maps), the thick, saline subsurface layer is reproduced by the model. Furthermore, the model clearly captures and explains how this saline layer forms from autumn to spring because formation of sea ice (with residual salinity of ~5 psu) injects salt to the ocean surface. This process results in coastal dense water formation (Wang et al. 2003c). Sea ice starts forming in October and continues to April, providing salty, cold water to form the saline layer. This phenomenon is one of the important coastal processes revealed by the CIOM. The temperature in transect 2 also shows that cold water formed during the winter seasons in the subsurface layer can survive the summer (not shown).

Figure 7 shows a winter section in the Canadian Beaufort Sea (see section 5 in Figure 6), as simulated by CIOM. The observations (Melling 1993, lower right panel) indicate upwelled, warm Atlantic Water with subsurface, dome-shaped structure. The surface winter water is around the freezing temperature during winter. The model also shows the upwelled Atlantic Water with an upwelled tongue, particularly in the winter.

Figure 8 shows the alongshore velocity to transect 6 (see the inserted panel in Figure 6 for the location) where velocity measurements were conducted by a high-resolution ADCP array (Pickart 2004). The observed subsurface core current or the so-called BSC was captured by the model, consistent with the measurements. The observations show three types of slope current structure. One is the westward at the surface and the eastward slope current at subsurface, which is captured from April to July by the CIOM. The second type of structure is the subsurface jet flowing to the east, which is captured by CIOM from January to March. The third type of structure has the surface eastward flow that the CIOM can reproduce from August to December. Note that the CIOM-simulated results are free of data assimilation.

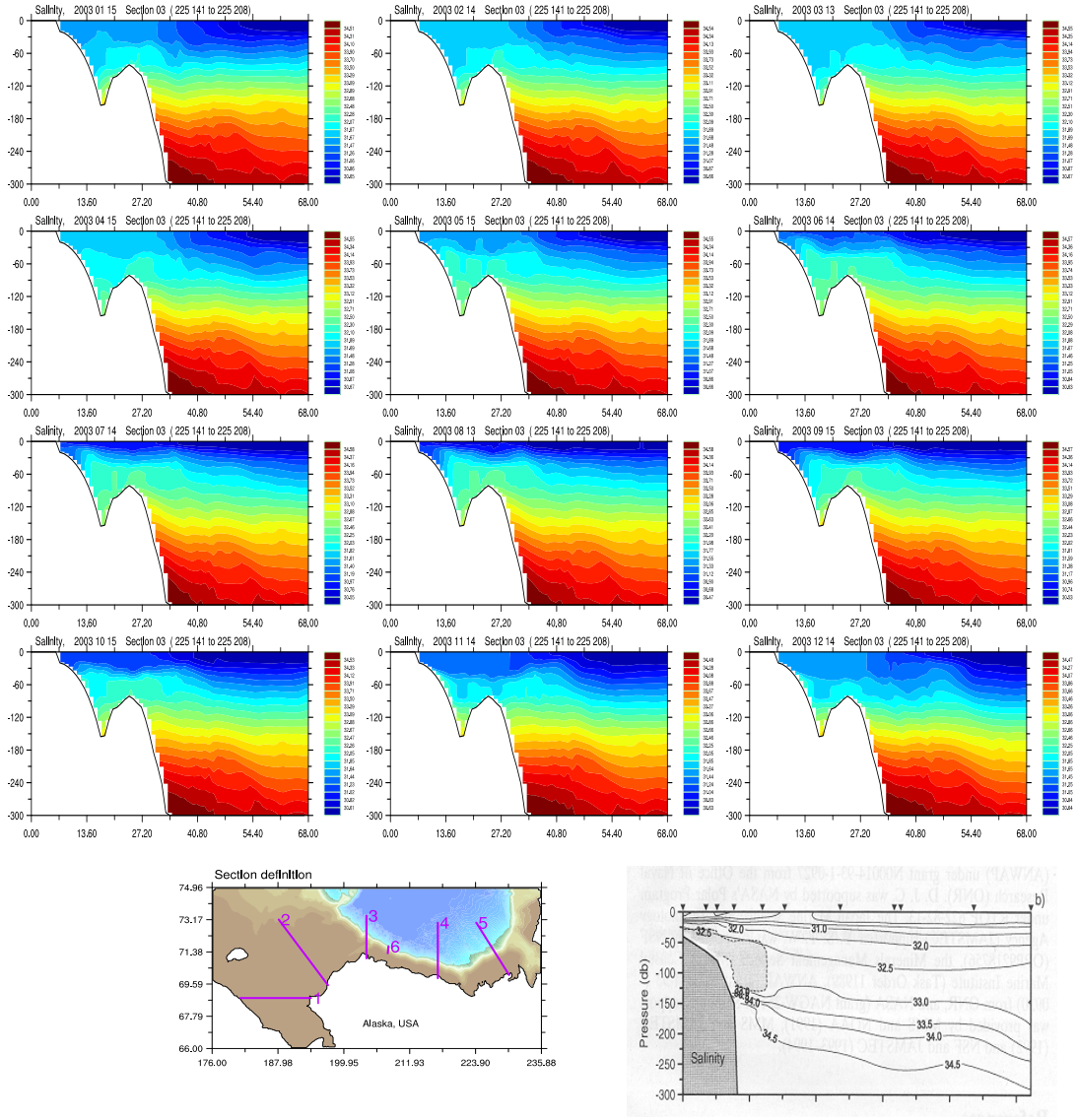


**Figure 6. The CIOM-simulated monthly salinity in transect 3 (see the lower left map) from left to right and top to bottom: Jan., Feb., Mar., … Dec., which reveals a thick, saline subsurface layer as observed in the summer survey by Weingartner et al. (1998, see the lower right map).**

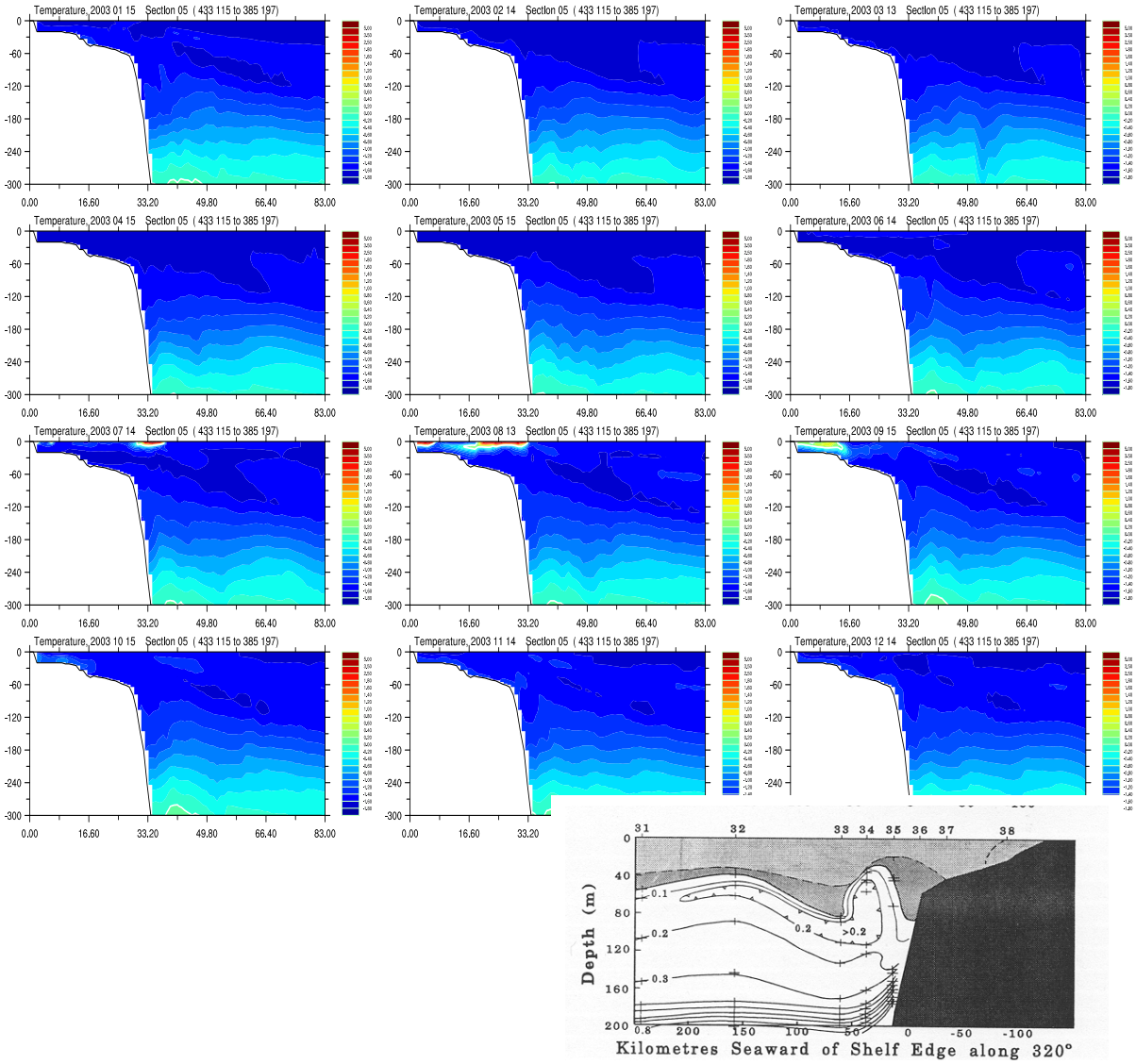


**Figure 7. The CIOM-simulated monthly temperature in transect 5 from left to right and top to bottom: Jan., Feb., Mar., … Dec., which reveals a winter upwelling along the Beaufort coast due to the anticyclonic wind forcing. Observations for winter 1990 are shown in lower right corner of the figure (Melling 1993).**

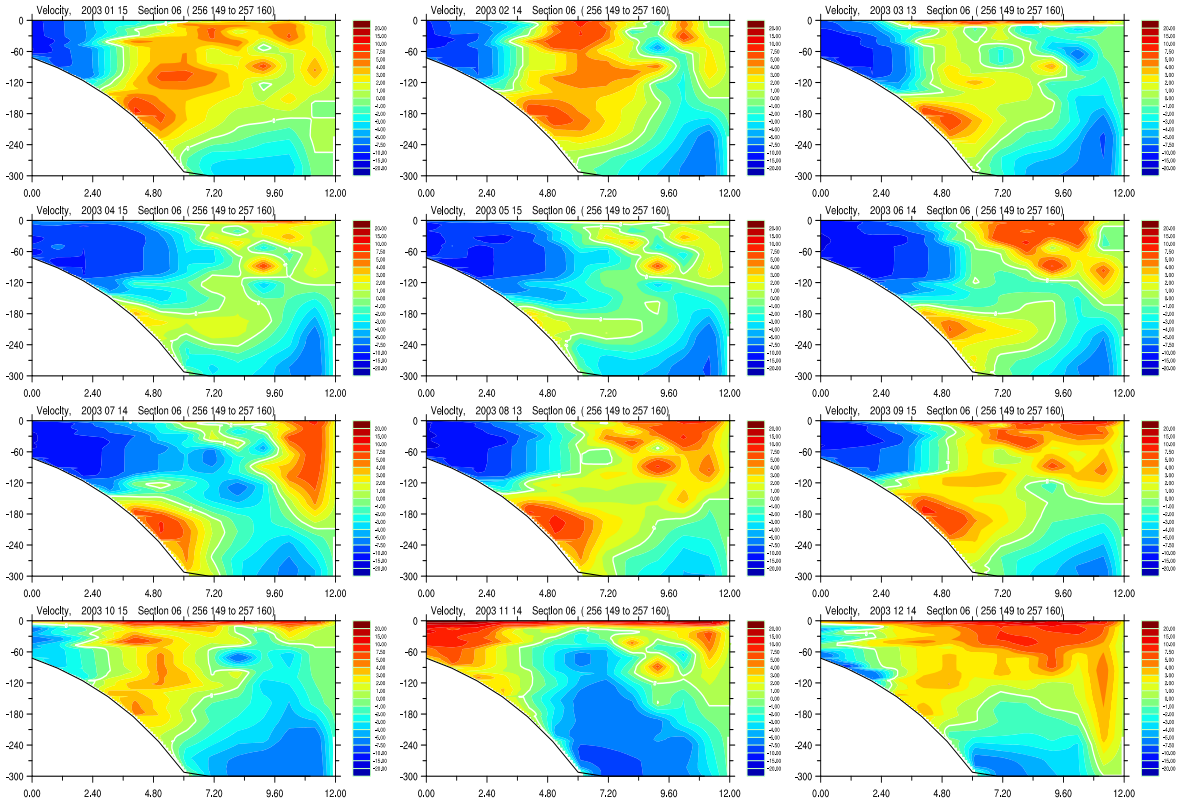


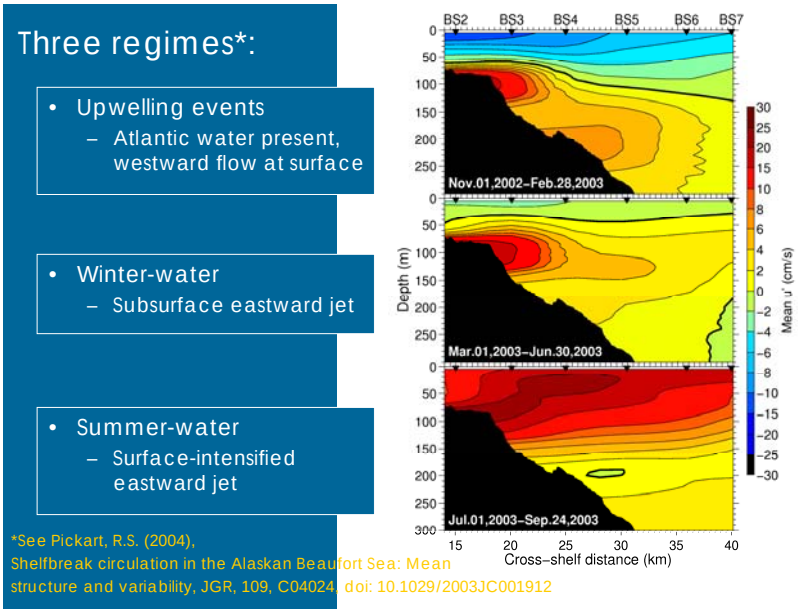


**Figure 8. (Upper) The CIOM-simulated the alongshore current at transect 6 (see the inserted panel in Figure 6 for the location) from left to right and top to bottom: Jan., Feb., Mar., … Dec., which reveals intraseasonal variation of the Beaufort Slope Current (BSC) (Lower) The subsurface core current was observed by a high resolution ADCP array at this transect by Pickart (2004).**

Pacific waters entering the Chukchi Sea enter the Arctic Ocean via three branches: ACW branch, Herald Valley branch and Central Channel branch (Weingartner et al. 2005), as discussed above (see Figures 1 and 4) and as will be further discussed in section 9. The oceanic heat transport via these three branches is the key for sea ice melting. In particular, the overwintering of the Pacific waters could be one of the major reasons for the recent ice reduction in the Western Arctic (Shimada et al. 2006).

Figures 9, 10, and 11 show the seasonal variations of temperature, salinity, and northward velocity, respectively, in transect 1. The salinity section captures a seasonal freshening in summer and salinization in winter due to saline injection, in particular along the ACW current. The ESC waters are freshest, while the ACW is the second freshest (Weingartner et al. 1999). We also observed that the bottom waters are saltier because the saltier waters come from Anadyr Current waters and form locally during fall-winter seasons (see October to April), consistent qualitatively with the measurements of Weingartner et al. (2005). The saltier waters are enhanced in summer, because the Bering inflow consists of the fresher, nutrient-poor ACW and the saltier, nutrient-rich Anadyr Current water. Along with the ESC, this section captures the encountering of these three water masses.

The temperature section (Figure 10) indicates the seasonal cooling-warming variations. The major features simulated include 1) the Bering Inflow advects warm water in summer and cold water in winter into the Chukchi Sea, 2) from fall to winter, the water column is well-mixed due to cooling and tidal stirring, 3) the Pacific waters can survive the winter (see maps of Jan. to May), and 4) ESC water is coldest year round. These simulated features coincide qualitatively with the available measurements (Weingartner et al. 1999, 2005).

The velocity section (Figure 11) shows the Bering inflow is dominant in summer. While the ACW current tends to be barotropic in nature, the ESC appears full of eddies, consistent with the buoyancy-driven characteristics described by Weingartner et al. (1999).

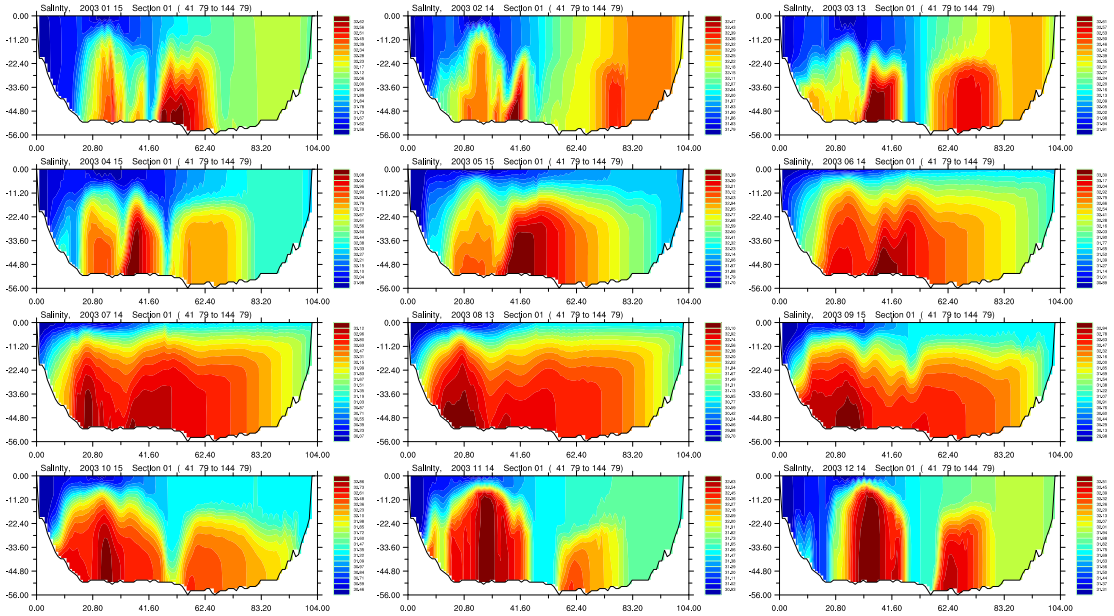


**Figure 9. Same as Figure 6, except for section 1 salinity.**

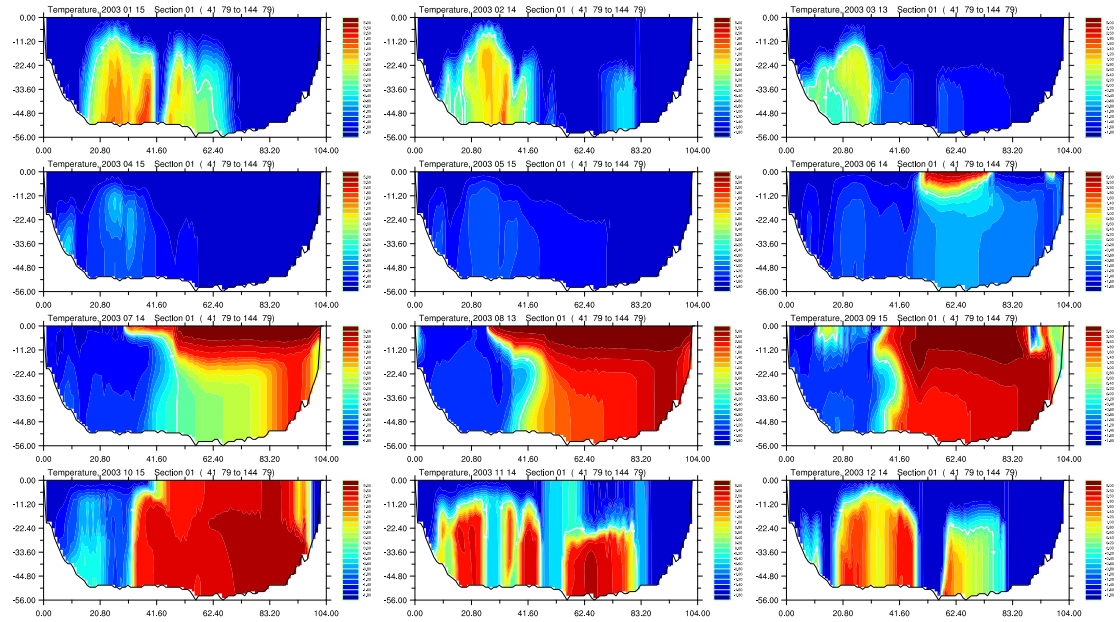


**Figure 10. Same as Figure 6, except for section 1 temperature.**

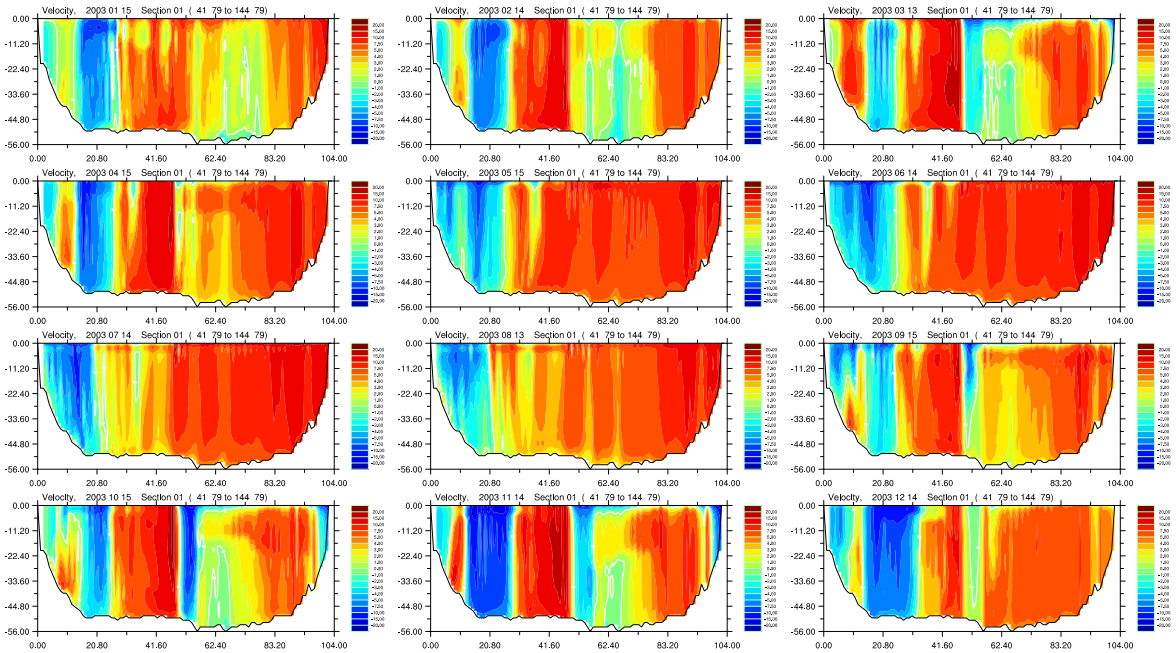


**Figure 11. Same as Figure 6, except for section 1 velocity: red (blue) denotes northward (southward).**

### *4.2 Sea ice ridging and landfast ice*

Figure 12 shows sea ice concentration (SIC) and thickness on July 10 under the climatological monthly forcing. The SIC map (Figure 12, upper) indicates various shapes of ice floes during the melting season. During spring, sea ice melts offshore first, and the pack ice gradually melts piece by piece into various shapes. Even in July, the Beaufort coast landfast ice remains, not melting completely until August. Sea ice arching, leads, and cracks can be observed from the simulated seasonal SIC maps (not shown). The reason for the late (August) melting of landfast ice may be due to the monthly forcing that is too weak, compared to the daily forcing.

The sea ice thickness map (lower panel of Figure 12) on July 10 shows sea ice ridging and rafting due to sea ice dynamic interaction with oceanic circulation pattern, shear, convergence, and divergence. Landfast ice along the Beaufort Sea coast is clearly simulated. Mechanics of formation and maintenance of landfast ice in the model may be attributed to the following factors: 1) a northeast wind due to the Beaufort High pressure system, 2) the eastward ACW current has a right-turning force due to the Coriolis effect, 3) high resolution topography and geometry, and 4) internal sea ice stress. However, how to identify and quantify these major factors remains open. Sensitivity experiments will be used to test these mechanisms in section 8.

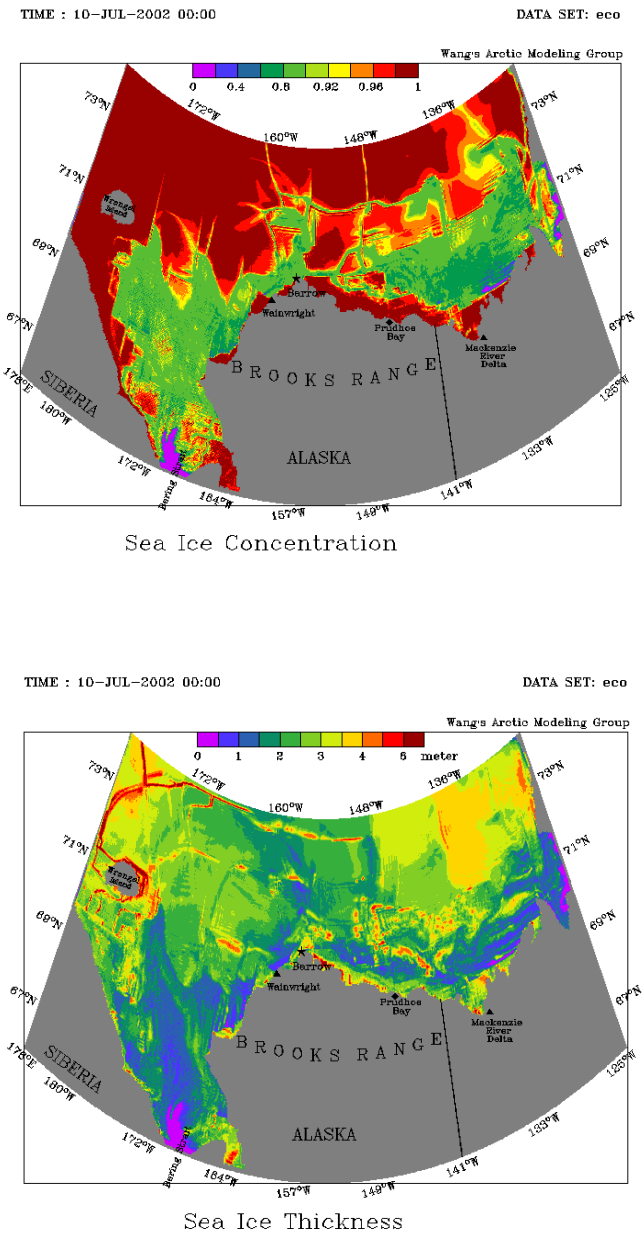


**Figure 12. The sea ice concentration (top; scale: from 0 to 1) and sea ice thickness (bottom panel) on July 10, as simulated by the high-resolution Coupled Ice-Ocean Model (CIOM; Wang et al. 2002a, 2005) that is nested to the Japan CCSR/NIES/FRCGC (Center for Climate System Research/National Institute of Environmental Studies/Frontier Research Center for Global Change) high-resolution global model. Sea ice breaks up offshore piece by piece; landfast ice remains untouched along the Beaufort Sea coast. Sea ice floes are irregular in shape and break away from pack ice. Sea ice ridging, rafting, and openings/leads can be well reproduced by sea ice thickness (bottom panel).**

### *4.3 Comparison of model simulation with satellite measurements*

The seasonal cycles of the Beaufort and Chukchi sea ice is well reproduced in comparison to the satellite-measured sea ice area as shown in Figure 13. Mizobata et al. (2008) not only collected and analyzed sea ice extent, SST via satellite, but they also collected chlorophyll *a* and the derived primary productivity data. Figure 13 indicates the model does not capture the summer minimum sea ice area, although the overall seasonal cycle is well reproduced. Note that the SSM/I does not identify ice ponds (i.e., melting water ponds on the sea ice) from sea water (R. Kwok, personal comm., 8/2006); thus, the satellite observed sea ice area minimum (black line) may underestimate the summer sea ice area (i.e., overestimate the open water). Nevertheless, CIOM still needs to be improved.

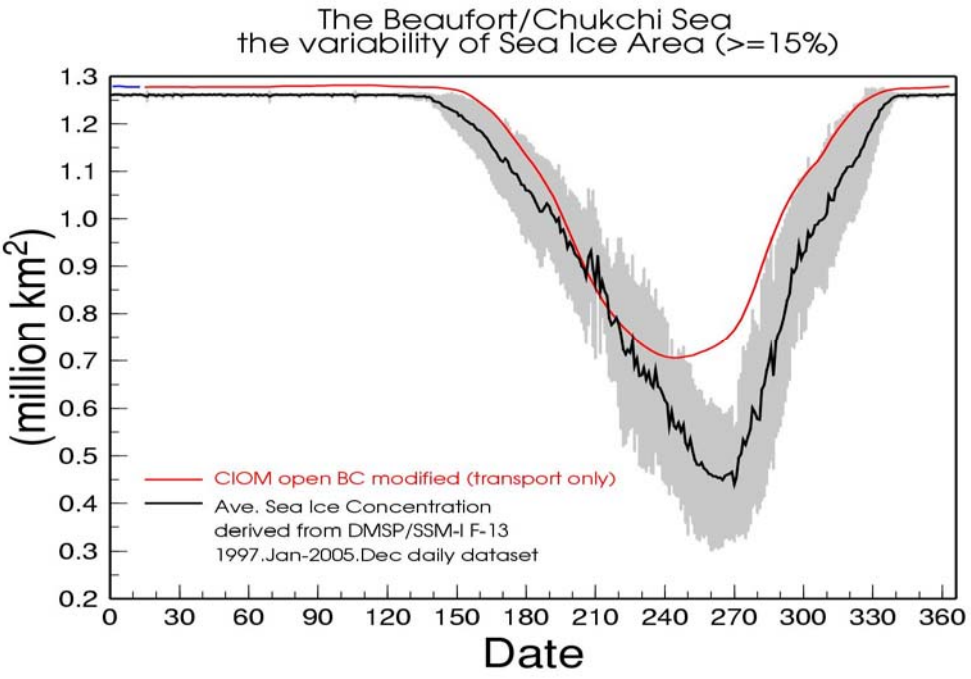


**Figure 13. Model-data comparison: Satellite-measured (black) and model-simulated (red) sea ice cover.**

**Figure 14. The comparison between the CIOM-simulated SIC (a) and SST (c) and satellite-measured SIC (b) and SST (d). Superimposed into the modeled SIC and SST maps are the surface ocean currents (a, c), while superimposed into the remote sensed SIC and SST maps are the NCEP wind vectors (b, d).**

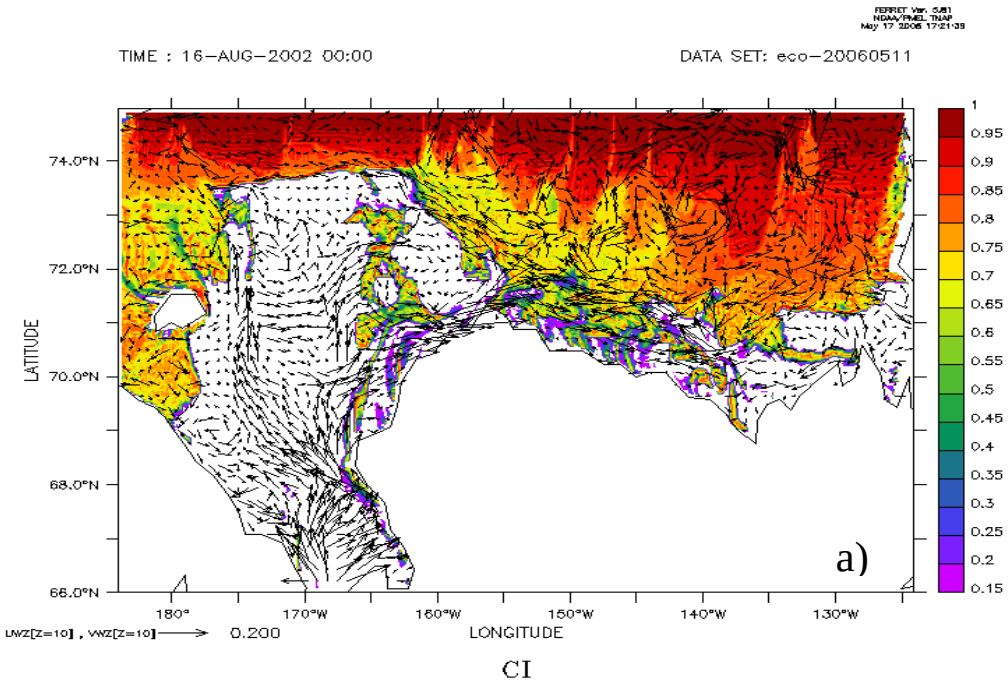


CI

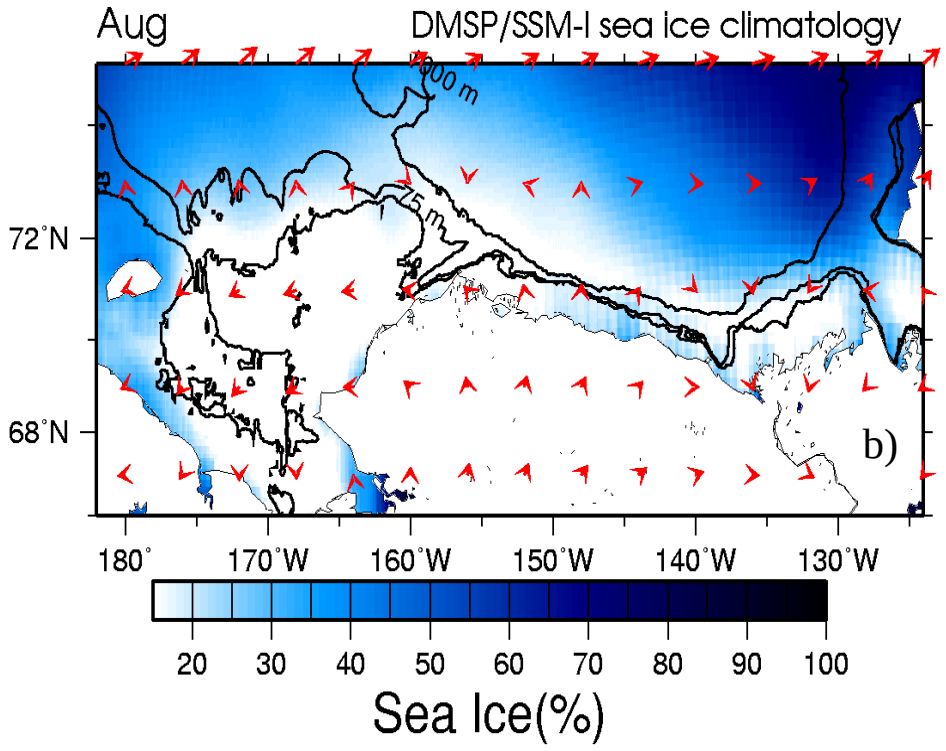

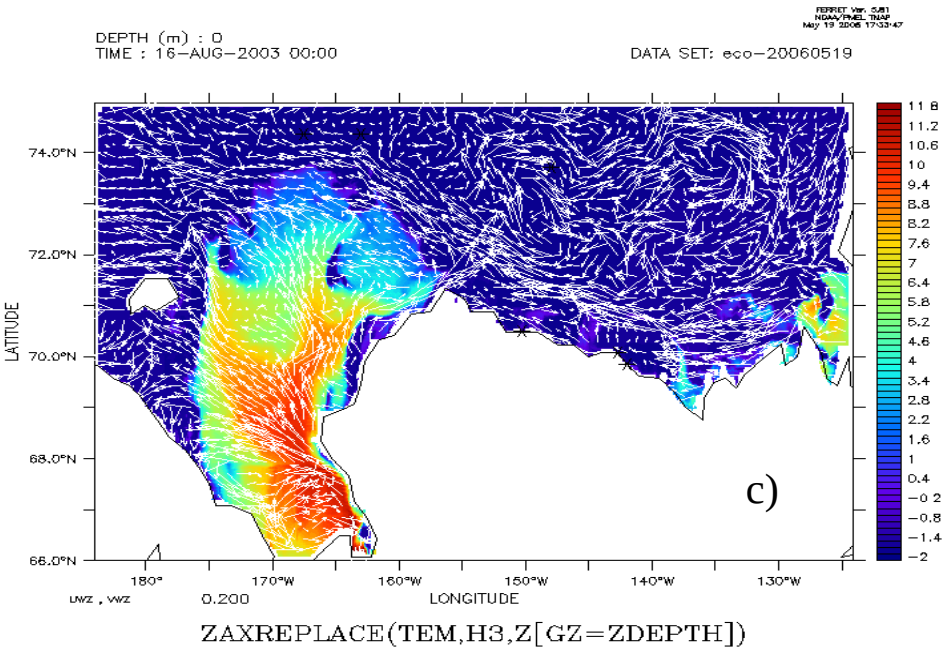
DEPTH (m) : 0
TIME : 16-AUG-2003 00:00
DATA SET: eco-20060519
74.0°N
72.0°N
70.0°N
68.0°N
66.0°N
LATITUDE
180°
170°W
160°W
150°W
140°W
130°W
LONGITUDE
0.200
11.8
11.2
10.6
10
9.4
8.8
8.2
7.6
7
6.4
5.8
5.2
4.6
4
3.4
2.8
2.2
1.6
1
0.4
-0.2
-0.8
-1.4
-2
c)
ZAXREPLACE(TEM,H3,Z[GZ=ZDEPTH])

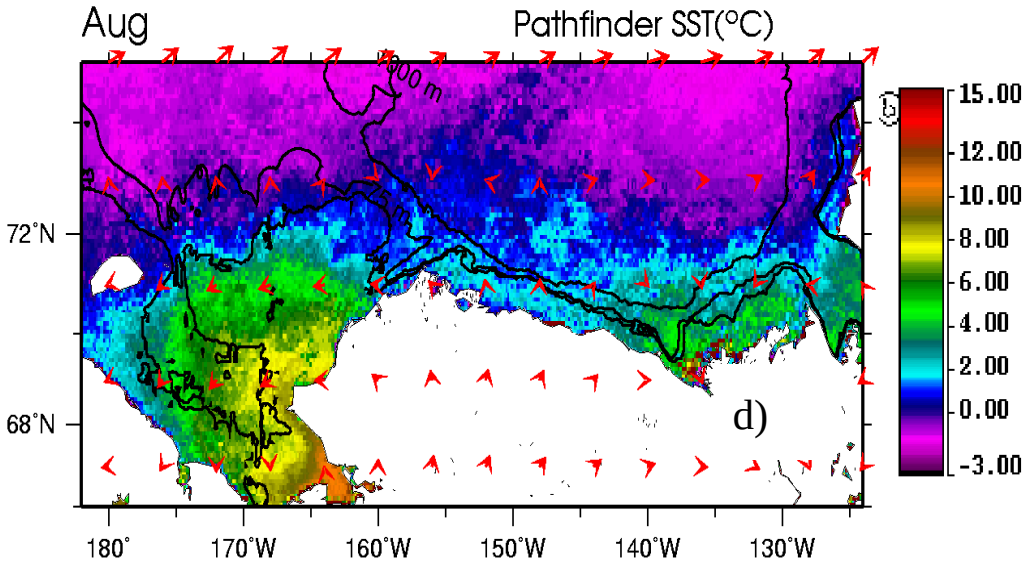
Aug
Pathfinder SST(°C)
200 m
72°N
68°N
180°
170°W
160°W
150°W
140°W
130°W
15.00
12.00
10.00
8.00
6.00
4.00
2.00
0.00
-3.00
d)

The model-simulated spatial patterns of sea ice extent and SST were compared to satellite measurements for July (not shown), August (Figure 14), and September (not shown). The August map indicates that the CIOM in general reproduces a reasonable spatial pattern of SIC and SST, except that the SST along the Beaufort Sea coast is underestimated. This results in the overestimate of sea ice along the Beaufort coast, particularly the landfast ice. The major reason should be that the monthly rather than daily forcing was used, because the monthly climatology is usually weak. This problem will be addressed in section 5. There may be several other reasons for the underestimate of SST: 1) the warm Bering Sea inflow is not well represented, 2) lateral melting is not included, and 3) tidal mixing is not included.

## 5. Model simulations with daily forcing and lateral melting

After the spin-up integration, we ran the CIOM under the NCEP/NCAR Reanalysis daily atmospheric forcing. Those daily datasets also originated from the NOAA/CDC/NCEP/NCAR website.

### *5.1 Validation of CIOM using in-situ observations*

The JAMSTEC measurements were used to validate the model results under the daily atmospheric forcing in a specific year, such as during 1998-99 measurements at Station 10 (BFK98, see location in Figure 3). We conducted a point-to-point comparison that has long challenged all ocean models (except for tide models), including CIOM. Nevertheless, the comparison between the averaged parameters is expected to be more reasonable.

Figure 15 shows the depth-time temperature comparison at BFK98 for the period of January-July 1999. The CIOM produces less temperature variability (Figure 15a) than in situ measurements, a common problem for models. This problem exists for all variables: salinity (Figure 15b) and velocity (Figure 15c). The point-to-point comparisons of T, S, and velocity time series are shown in Figure 16, indicating a large discrepancy exists in all the simulated variables with no data assimilation. The model basically captures the mean values (Figure 17), which is correct and encouraging on the first-order approximation, nevertheless, with less variability. This problem exists in all small-scale to large-scale circulation models, except for ocean tide simulations (Ford et al. 1990; Wang 1998).

There are many factors responsible for less variability derived from CIOM and from other models as well: 1) the boundary conditions use a coarse-resolution (1/4x1/6 degrees) global GCM monthly output, which filters out the high frequency and small-scale variability with smaller

magnitude, 2) smoothing of topography, 3) less spatial variability of the wind field, 4) numerical filtering in the model, 5) numerical diffusivity due to truncation errors, and many others. This problem can be improved, but may never be cured until high accuracy numerical schemes with natural (zero) numerical diffusivity can be developed and applied to ocean models without smoothing topography.

**Figure 15. Time-depth comparison of observed (upper) and modeled (lower) temperature (a), salinity (b), and velocity, u (c) and v (d) at BFK98 (station 10). The model captures the mean state, with less variability for all the variables.**

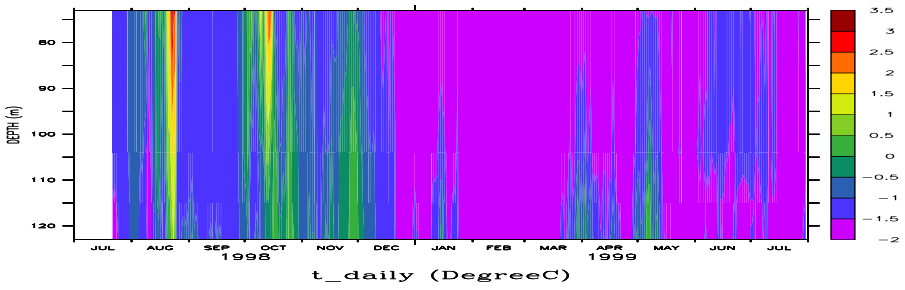


Observed

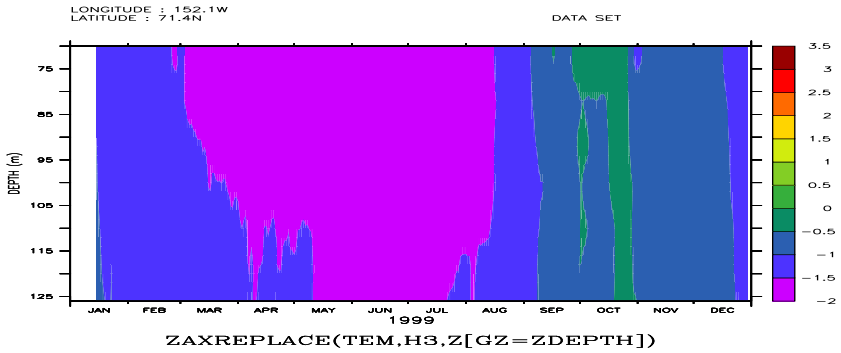


Modeled

(a) Temperature

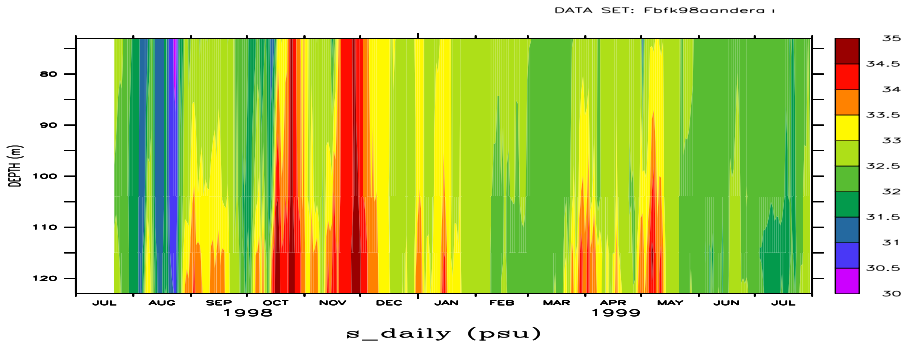


Observed

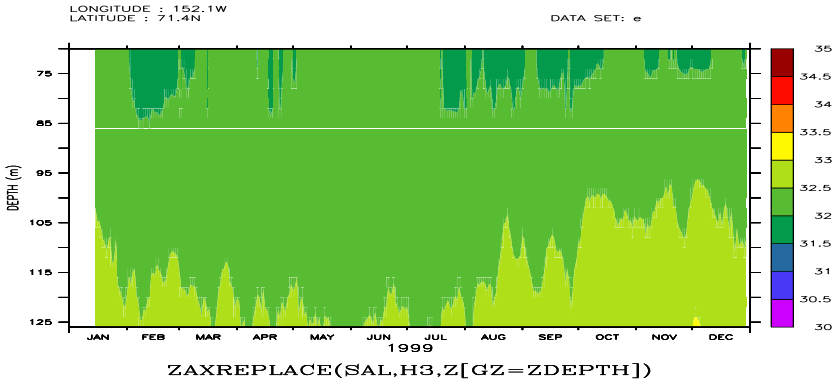


Modeled

(b) Salinity

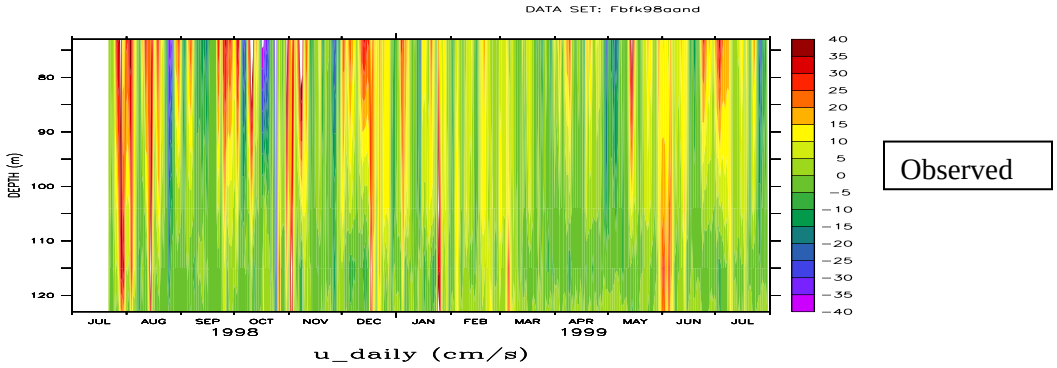


Observed

Modeled

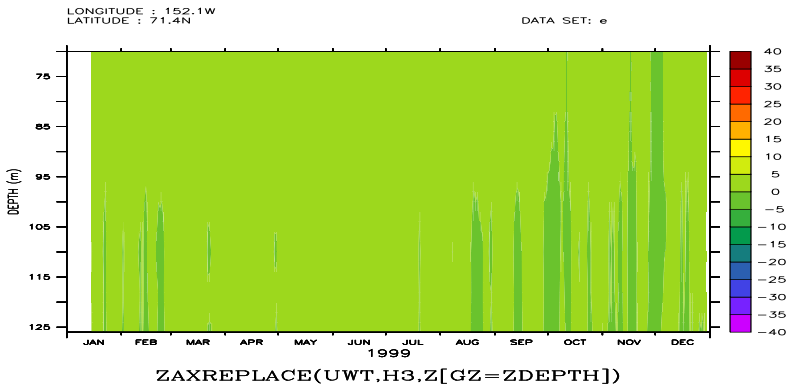


(c) velocity, u

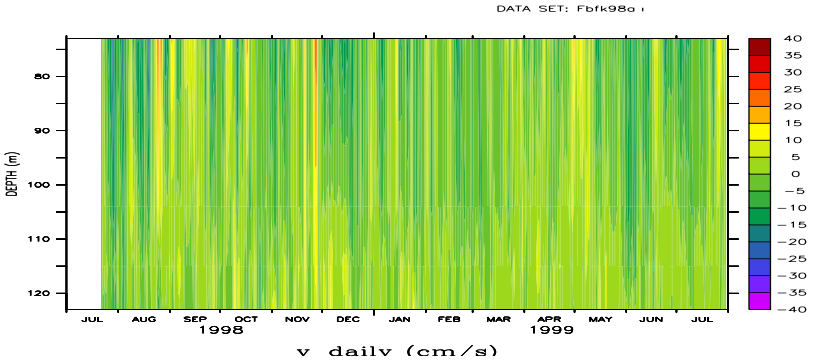


Observed

Modeled

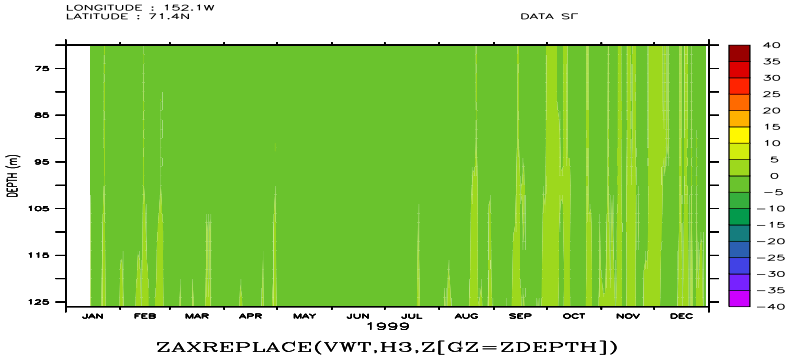


(d) velocity, v

**Figure 16. The point-to-point comparisons of the time series of temperature (upper left), salinity (upper right), velocity u (lower left), and velocity v (lower right) at BFK98 (station 10). Black curves are observation, while blue lines are modeled time series.**

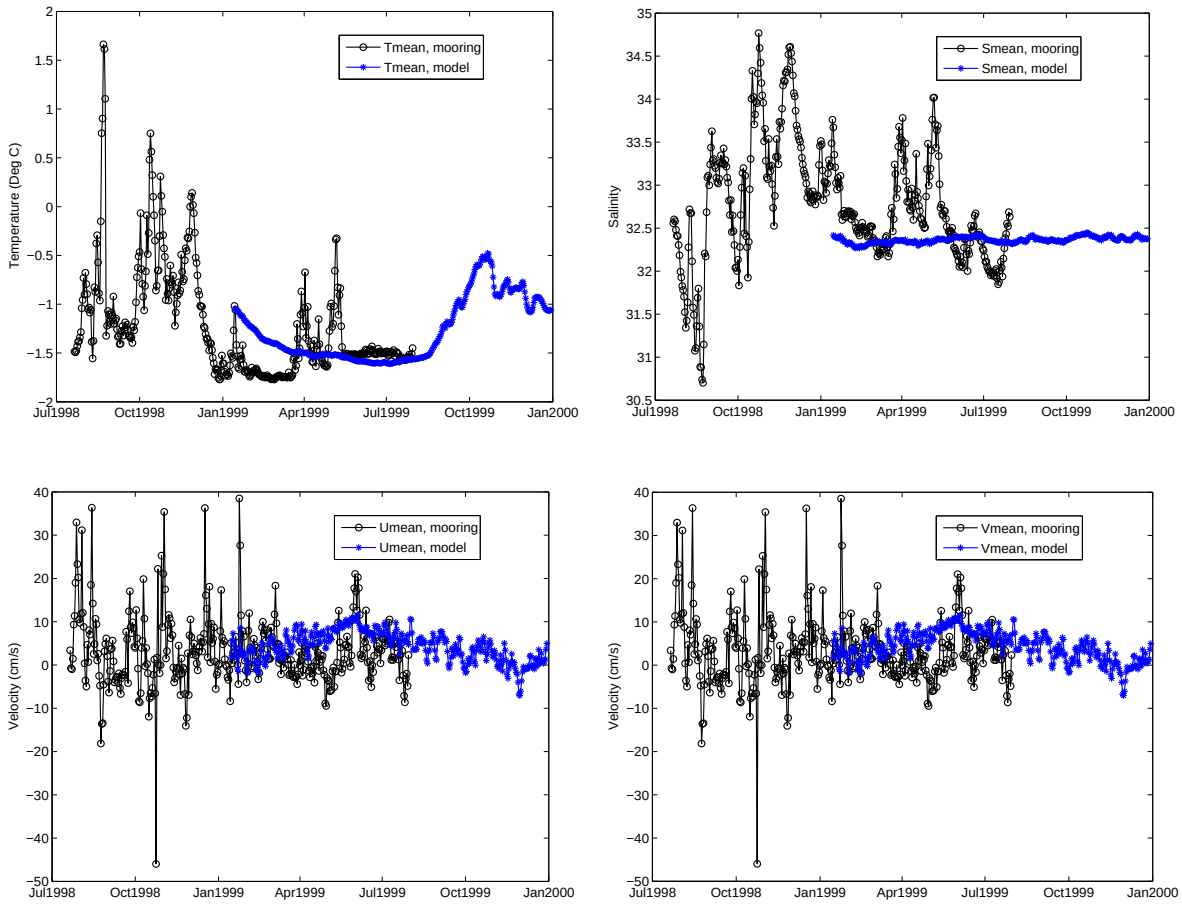

**Figure 17. Time-averaged vertical profiles of observed velocity, U and V (black) and modeled velocity, u and v (blue) at BFK98 (station 10).**

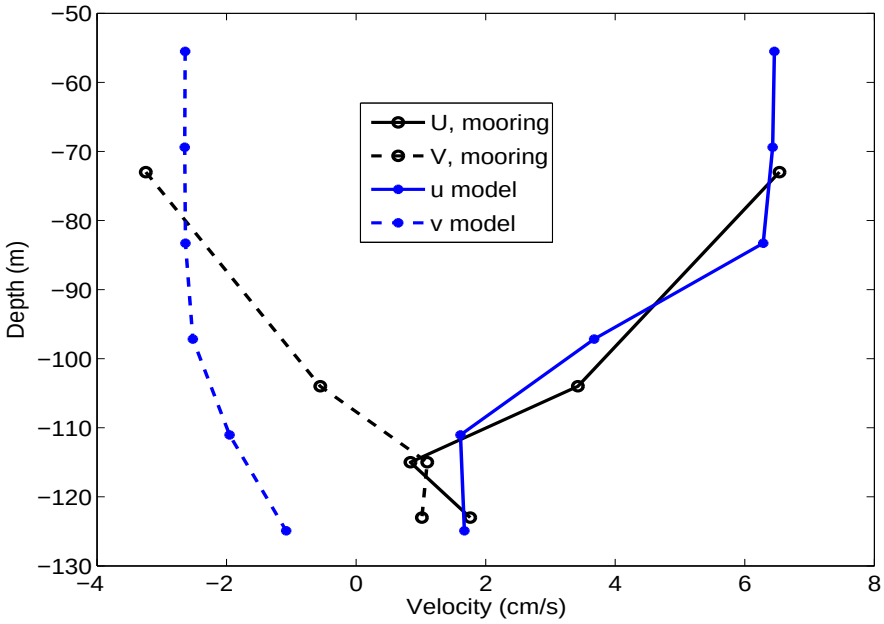

### *5.2 Validation of CIOM using satellite measurements*

#### *5.2-1 Seasonal cycle of sea ice area*

To evaluate outputs of the CIOM, we compared the simulated results with satellite measurements. Figure 18 shows the time series of the averaged sea ice area derived from SSM/I measurements between 1997 and 2005 (blue line), sea ice area in 2002 (blue line), and sea ice area in 2002 simulated by the CIOM (red line). In Figure 18, we plotted a 3-day averaged sea ice area estimated from the CIOM output, so that short-term variability, which is shown by the SSM/I measurements, is reduced. However, the CIOM accurately reproduces the seasonal cycle of sea ice in the Chukchi/Beaufort Sea, while the simulated sea ice was suddenly melted in late July due to the imposed lateral melting parameterization. The maximum sea ice area and the timing of ice melting/freezing are consistent with SSM/I measurements. Also, sea ice freezing during winter (October-December 2002) was accurately reproduced. During August, 2002, the open water area was larger in the simulation than what was measured by the SSM/I. The melting rate of sea ice from May to August and maximum sea ice retreat still need to be improved. Obviously ice melting rate is slow during May and early June and fast during late July and August, compared with the SSM/I measurements.

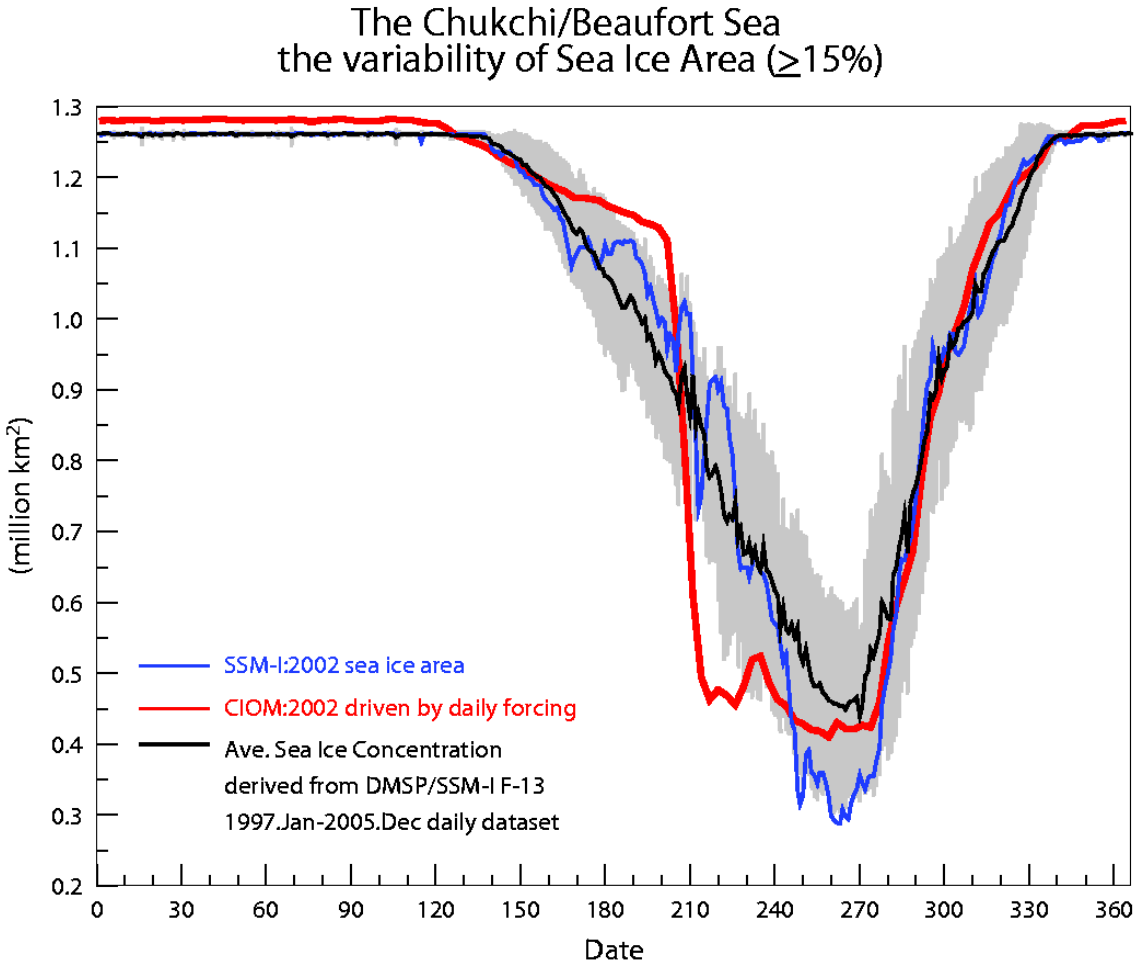


**Figure 18. Seasonal cycle of sea ice area in the Chukchi/Beaufort Sea derived from the SSM/I measurements (blue line, daily) and simulated by the CIOM (red line, 3-day averaged). Sea ice concentration less than 15 % was ignored to avoid the error of SSM/I measurement. Gray area represents the daily variance of the averaged sea ice from 1997 to 2005.**

### *5.2-2 Simulated sea ice distributions and motions during ice freezing season (January - April)*

Figure 19 shows sea ice concentration and sea surface temperature in the Chukchi/Beaufort Sea on January 15$^{th}$ to April 27$^{th}$. Red arrows represent ice velocity and black arrows represent 10-m ocean velocity. Generally, ice velocity in the Chukchi/Beaufort Sea in January (Figure19a) and February (Figure19b) is greater than that in March (Figure 19c) or April (Figure 19d) due to thinner ice cover and strong sea surface wind in early winter, while ice movement is also affected by surface ocean current. Relatively strong ice velocities along the Alaska coast on April 27$^{th}$ indicate ice advection by the Alaskan Coastal Current (Figure 19d). Those coastal currents flow in the narrow Beaufort coastal area and continue to the estuary of the Mackenzie River. On the other hand, cyclonic circulation, which has been observed (e.g., Pickart et al. 2005), was captured in the Beaufort Sea basin area during winter.

### *5.2-3 Simulated sea ice distributions and ocean circulation during ice melting season (June – September)*

The CIOM also simulated sea ice breakup/melting starting from June 2002. Figure 20 shows sea ice concentration greater than 30% (gray area), ice velocity (red arrows), sea surface temperature, and water velocity at 10 m water depth (black arrows) on June 20$^{th}$ (Figure 20a), July 20$^{th}$ (Figure 20b), August 10$^{th}$ (Figure 20c), and September 18$^{th}$ (Figure 20d).

Ice velocity is weak during winter (Figure 19). Open water started to form (i.e., ice started to break up) in the southern Chukchi Sea shelf in May or June (Figure 20a) and at the estuary of the Mackenzie River in July (Figure 20b). In August, wide open water occurred at the northern Chukchi Sea shelf and basin area (Figure 20c). Also a wide lead-like feature and landfast ice can be seen at the northern Alaska coast in the Beaufort Sea. Details of landfast ice will be discussed shortly. In September, sea ice cover is diminished, resulting in wide open water in the Beaufort Sea (Figure 20d). Mesoscale features can be found at the ice edge in the Beaufort Sea. In August and September, high water temperature of more than 8$^{o}$C was found in the Chukchi Sea. The distribution of warm water and ocean circulation represent the pathway of the Pacific Summer Water through the Bering Strait (Figure 20c, white arrows). Relatively high temperature in the Beaufort Sea is due to both river discharge of the Mackenzie River and the Alaskan Coastal Current flowing along the Alaska coast. The plume near the estuary of the Mackenzie River was well simulated. Those features are consistent with previous ship surveys.

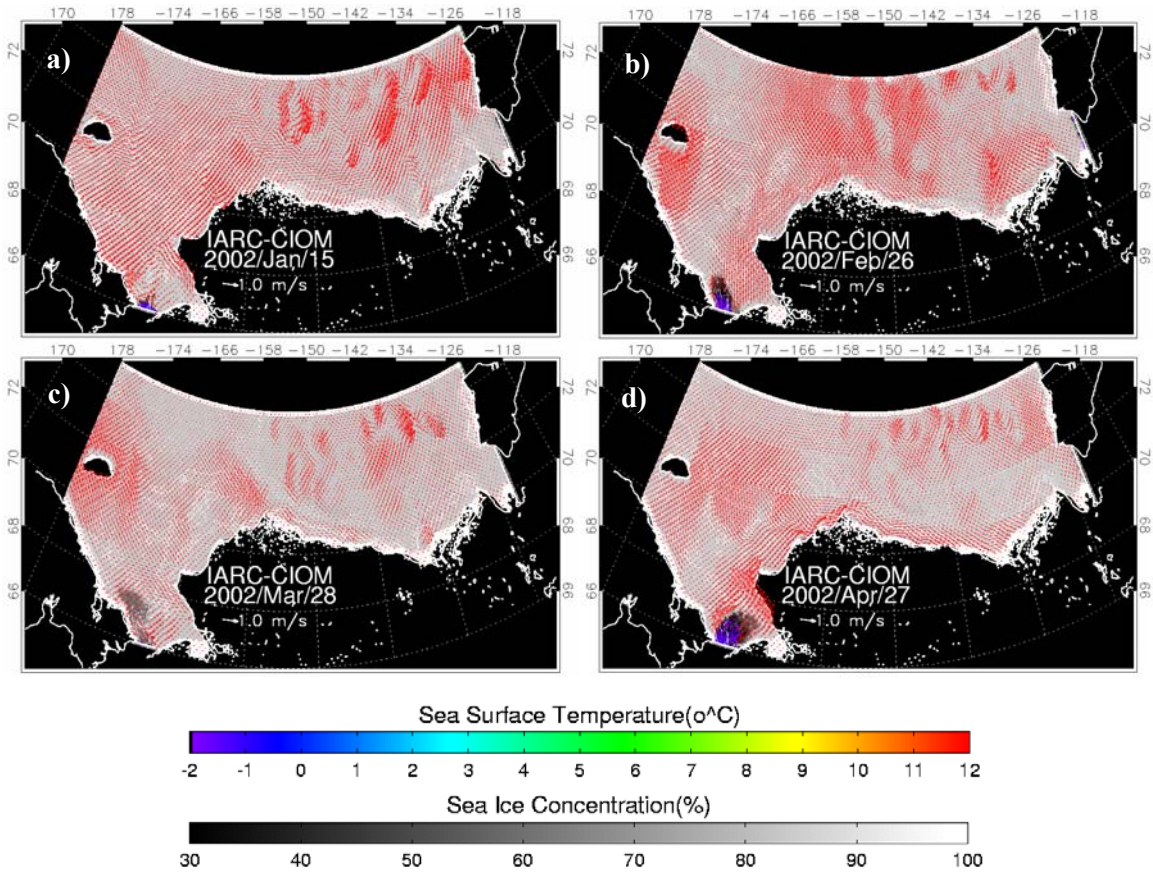


**Figure 19. Sea ice cover and motion in the Chukchi/Beaufort Sea on a) January 15th , b) Feb 26th , c) March 28th, and d) April 27th in 2002 simulated by the CIOM. Red arrows indicate ice velocity and black arrows indicate 10-m ocean velocity. Sea surface temperature is shown near the Bering Strait.**

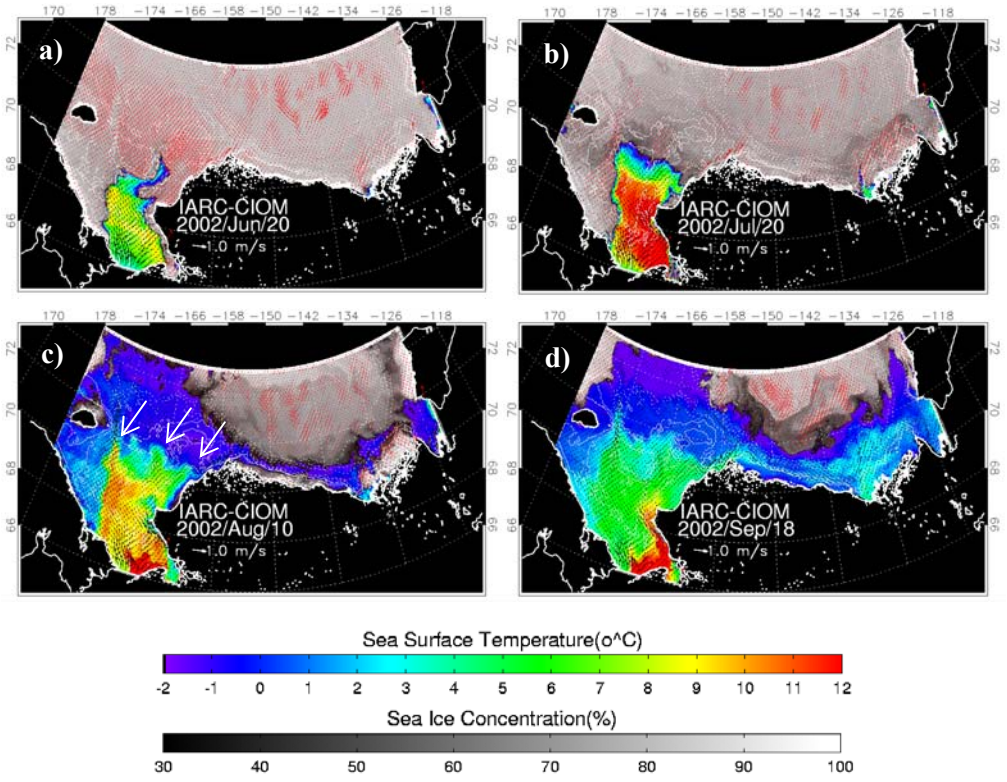


**Figure 20. Sea ice cover and motion in the Chukchi/Beaufort Sea on a) June 20th, b) July 20th, c) August 10th, and d) September 18th in 2002 simulated by the CIOM. Gray area shows sea ice concentration between 30% and 100%. Red arrows and black arrows indicate ice velocity and 10-m ocean velocity, respectively.**

Figure 21 shows remote-sensed SST and SIC in the Chukchi/Beaufort Sea. Satellite measurements indicate that open water started at the southern Chukchi Sea and at the estuary of the Mackenzie River (Figure 21a), and covered the Chukchi Sea shelf in July (Figure 21b). The relatively warm ACW can be seen in the Chukchi Sea shelf in August (Figure 21c, white arrow) and near the northern Alaska coast from Point Barrow to the Mackenzie River in September (Figure 21d, white arrows). Those features are similar to the simulated results (Figure 20). On the other hand, open water derived from satellite images is wider than that simulated by the CIOM during August and September in the Chukchi Sea. The difference between SSM/I measurements and CIOM simulation results could be due to the open boundary condition, ice-melting scheme, errors in satellite measurements, or other unidentified causes.

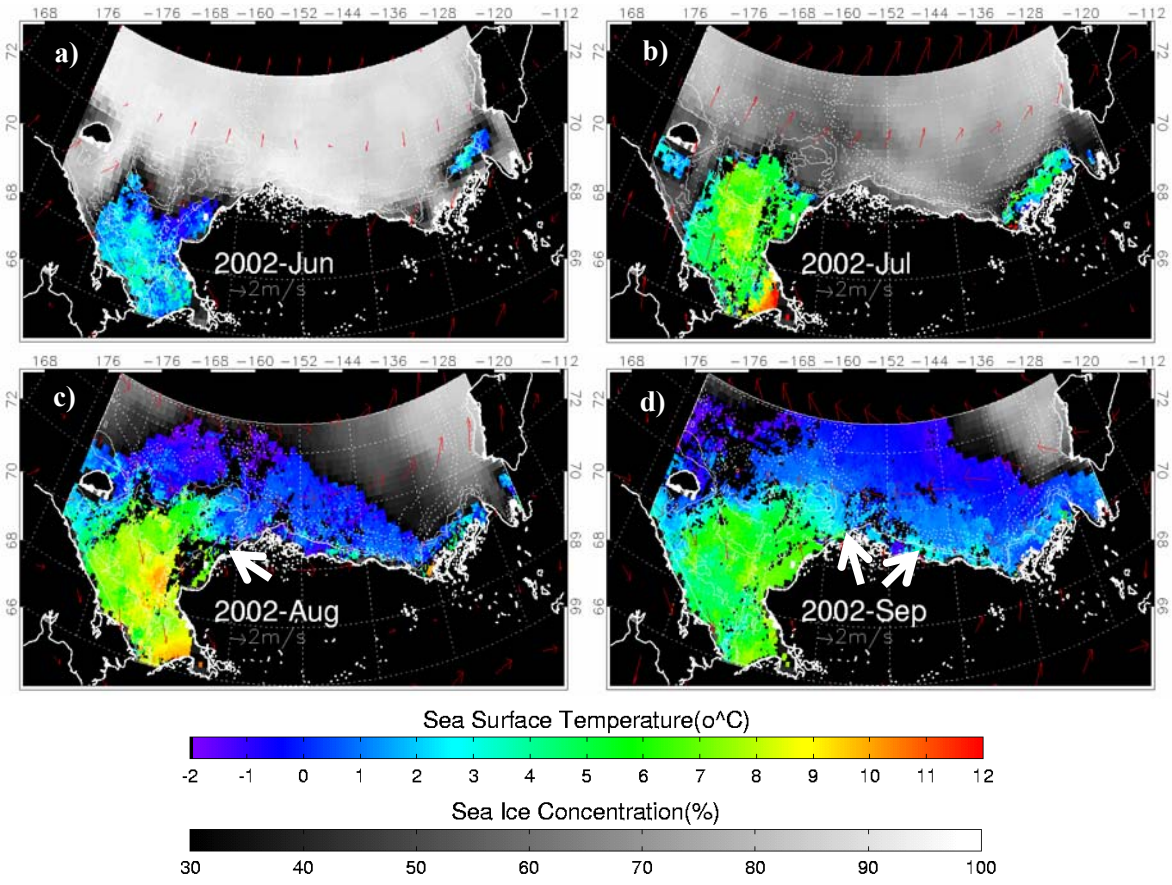


**Figure 21. Monthly mean sea ice cover and sea surface temperature in the Chukchi/Beaufort Sea between June and September 2002 derived from satellite measurements. Red arrows show NCEP/NCAR sea surface wind velocity.**

### *5.2-4 Ocean circulation in the Chukchi Sea Shelf*

In the Chukchi Sea shelf, warm Pacific water intrudes through the Bering Strait. Heat input through the Bering Strait could be a trigger of rapid sea ice reduction (Shimada et al. 2006). Figure 22 shows AVHRR daily sea surface temperature images on July 21$^{st}$ (Figure 22a), August 1$^{st}$ (Figure 22c), and September 22$^{nd}$ (Figure 22e) and ice-ocean circulation (Figures 22b, d, and f) simulated by the CIOM (same as Figure 20) in the Chukchi Sea. SST patterns are similar to the ocean temperature simulated by the CIOM. Both AVHRR SST and ocean temperature derived from the CIOM show warm water covering the Chukchi Sea in July (Figures 22a and b) and extending to the Herald Canyon, western Hanna Shoal, and southeastern Siberian coast in August (Figures 22c and d). The warm water pattern greater than 8$^{o}$C captured by the AVHRR indicates the ACW branches (Figure 22c, white arrows). Those features were well simulated by the CIOM, except for magnitude of temperature (Figure 22d, white arrows). The AVHRR SST indicates the warm Alaskan Coastal Current flowing along the Alaska coast. Warm water reached the Icy Cape in August (Figure 22c) and the Barrow Canyon in September (Figure 22e). The CIOM results are consistent with satellite measurements and previous ship surveys. Thus, the distribution of the warm Pacific water and ocean circulation in the Chukchi Sea were well simulated. The biggest difference between AVHRR images and CIOM results is the high water temperature core at the Siberian coast (Figures 22a and c). Currently, this high water temperature core is not well simulated. A similar warm core was found in July 2004. Therefore, this warm core is not due to error; however, it is hard to determine the origin. No scientific reports or papers exist showing this kind of feature. The investigation for this warm core is underway. If this warm core is a real phenomenon, it would affect the timing and pattern of sea ice freezing and melting. In this case, we will introduce it to the CIOM. A cold band at the Siberian coast in September (Figure 20e) is due to errors resulting from cloud or fog.

Note that the dates in the comparison of Figure 22 are not consistent. We tried to compare daily-basis satellite mappings and model output on the same date. But higher latitude ocean is very cloudy, i.e., it is very hard to compare them on the exact same dates. The model simulated surface data is very variable due to atmospheric conditions (i.e., wind). What we would like to say here is the CIOM can reproduce ocean circulation field, such as three branches separated from the Bering inflow, which were observed by hydrographic surveys and by satellite measurements, although there is discrepancy in dates.

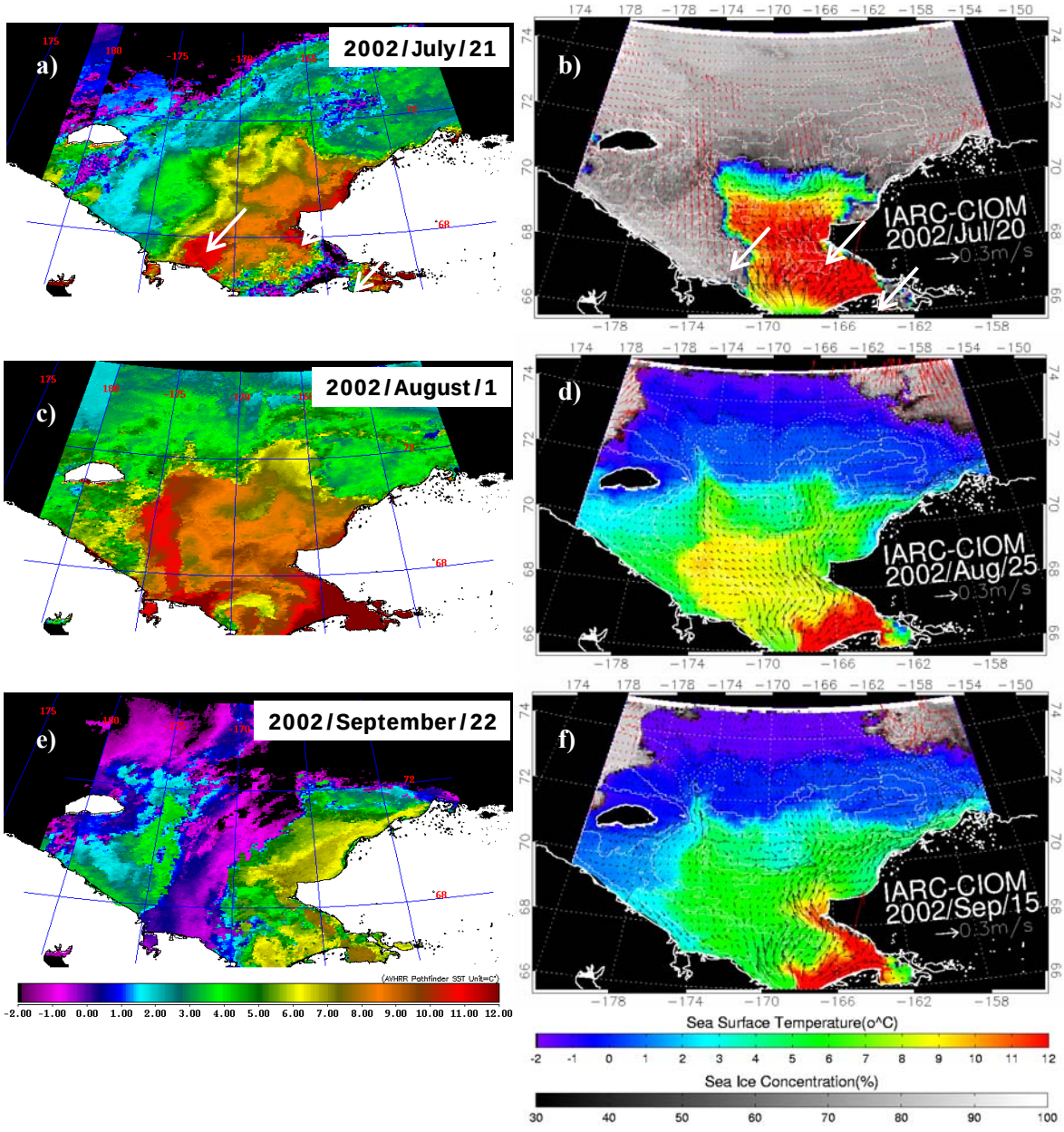


**Figure 22. AVHRR-derived daily sea surface temperature images on a) July 21st, c) August 1st, and e) September 22nd (left) and simulated ice-ocean circulations (b, d, and f) same as Fig. 20 but only for the Chukchi Sea.**

### *5.2-5 Landfast ice, ice cover, and ocean circulation in the nearshore Beaufort Sea*

The ice-ocean circulation is very complex in the nearshore Beaufort Sea. There are sea ice, the ACW coastal current, small-scale eddies, river discharge, and the Beaufort gyre. Figure 23 shows the CIOM results from August to November. Water velocity is plotted at every grid point (black arrows) because the scale of eddies is small (10-20 km) due to the fact that the Rossby radius of deformation is about 5 km. In August, open water was formed and warm Pacific water came from the Barrow Canyon. There was another source of heat, the Mackenzie River. Sea ice in the basin was melted, but the landfast ice still remained at the Alaska coast between 156$^{o}$W and 144$^{o}$W (Figures 23a, b, and c). SSM/I measurements also indicate the landfast ice along the Alaska coast in August (Figure 24). During September, wide open water and meandering of the boundary current resulting from eddies were simulated (Figures 23 d, e, f). Small-scale eddies in the Beaufort Sea will be discussed later. In October, the boundary current was close to the Alaska coast (Oct. 06, Figure 23g), and sea ice freezing started. In November, the CIOM simulated sea ice freezing and the polynya in the Beaufort basin (Figures 23 h, i). According to Figure 23, sea ice cover resulted from ice production at the coast (landfast ice) and in the basin, and ice advection from the basin to the Alaskan coast. Ice was produced at the Alaskan coast due to the shallow water depth, resulting in rapid freezing. On the other hand, SSM/I measurements show that sea ice cover is due to ice production in the basin area or advection from north or east (Figure 25). Wide landfast ice was not seen in October from SSM/I measurements possibly due to the coarse resolution (25 km), compared to the 3.8 km resolution CIOM. SSM/I measurements may also have errors because it is difficult to measure melt pond during the melting season. Due to coastal sea fog, the SSM/I measurements may also overestimate SIC along the coast by 10-15%, particularly in summer. There is a need to validate landfast ice production. The difference in the pattern of ice production between the CIOM and SSM/I measurements is under investigation.

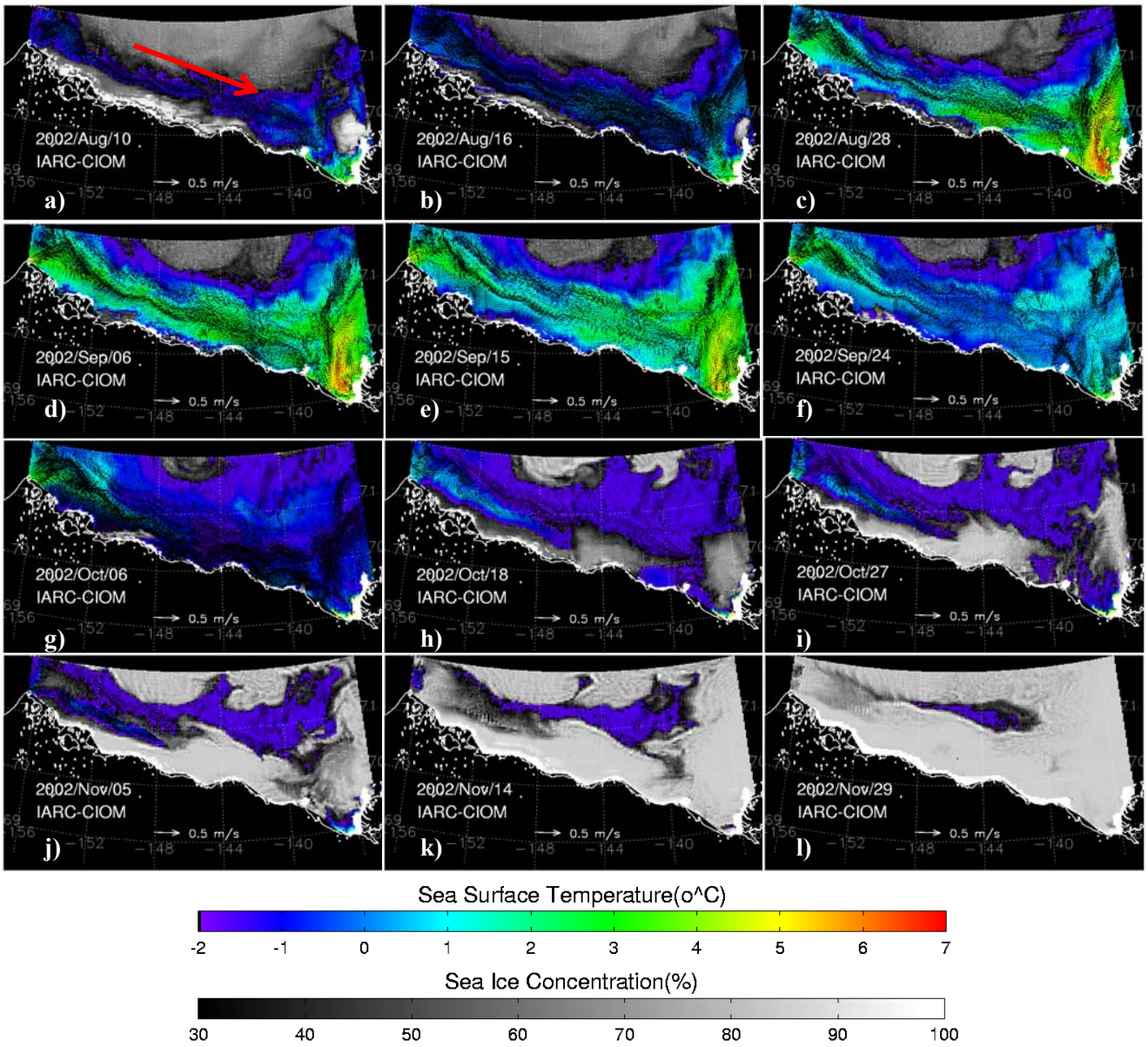


**Figure 23. Sea ice cover and ocean circulation in the Beaufort Sea coastal area on (from left to right) a) August 10th, b) August 16th, c) August 28th, d) September 6th, e) September 15th, f) September 24th, g) October 6th, h) October 18th, i) October 27th, j) November 5th, k) November 14th, and l) November 29th in 2002 simulated by the CIOM. Gray area shows sea ice concentration between 30% and 100%. Black arrows indicate water velocity (10 m water depth) at every grid point.**

**Figure 24. SSM/I sea ice concentration images in the Beaufort basin area on a) August 10th, b) August 16th, and c) September 6th. Note that the resolution is 25 km.**

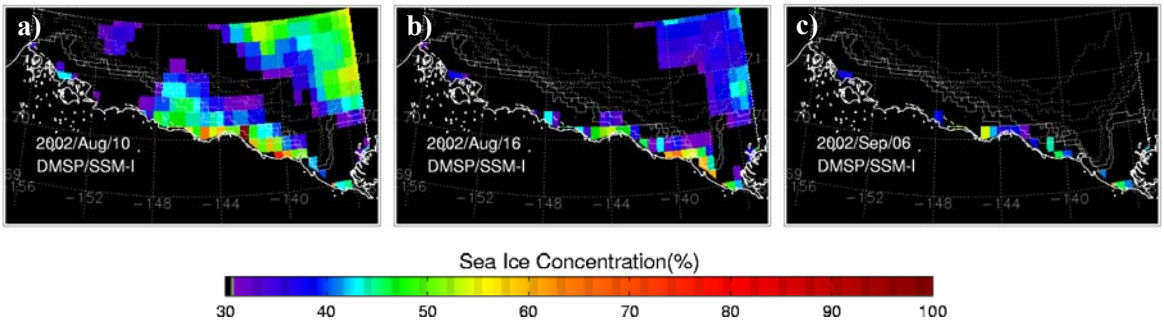


**Figure 25. SSM/I sea ice concentration images in the Beaufort basin area on a) October 6th, b) October 14th, and c) October 16th.**

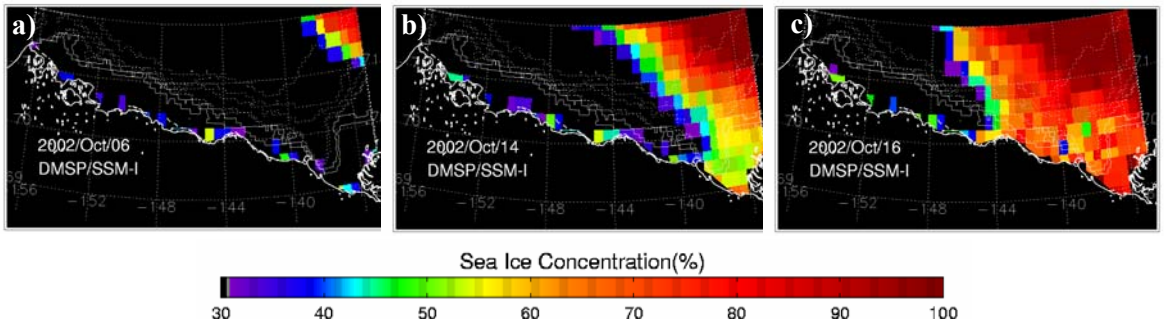


Figure 26 shows the 10-year (1994-2004) climatology (mean) of minimum, mean, and maximum landfast ice extents in the Beaufort Sea, measured by SAR and SSM/I by Eicken et al. (2005). During the period, the Arctic Oscillation (AO) was weakened (Wang and Ikeda 2000, 2001) and the Arctic Dipole Anomaly (DA; Wu et al. 2006; Watanabe et al. 2006) was intensified. The positive DA-derived anomalous meridional wind stress along the Trans-polar Drift Stream (TDS) toward the eastern Arctic produced anomalous open water in the Alaskan Beaufort Sea, and thus the anomalously less landfast ice along the coast. This is why there was little landfast ice in October (freezing season) and July (melting season). In other words, during the positive phase of DA, there is less landfast ice extent due to the offshore wind anomalies and during the negative phase of DA, there is more landfast ice extent due to the onshore wind anomalies.

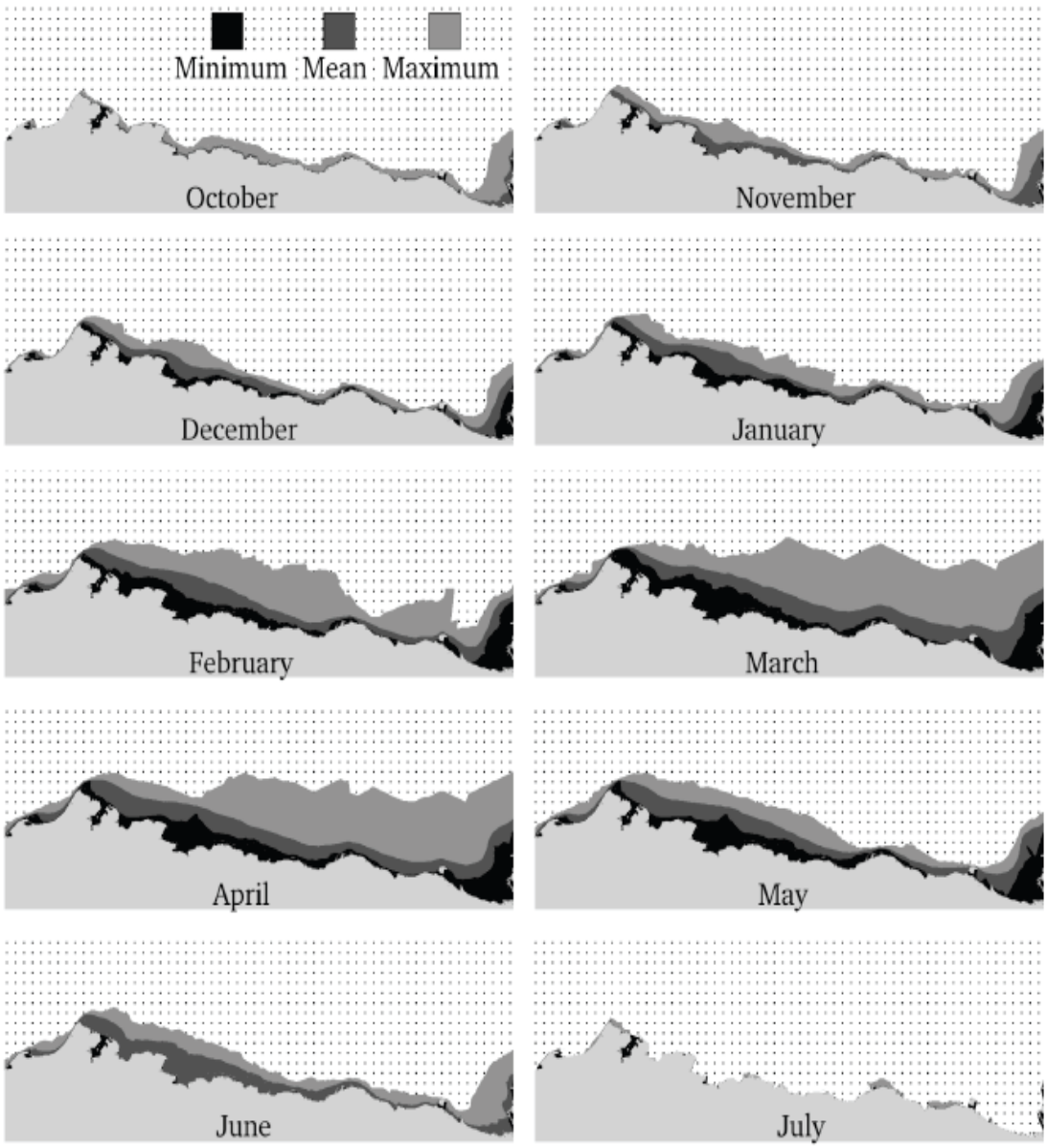


**Figure 26. Minimum, mean, and maximum monthly landfast sea ice extents showing the change in landfast ice distribution in the study area through the annual cycle. The dotted area indicates where landfast ice was never observed. From Eicken et al. (2005).**

During the open water period, small-scale eddies have been observed in the Beaufort Sea basin area (e.g., Muench et al. 2002). Figure 27 shows the simulated result on September 24th. Red boxes indicate the eddy field. There are two main streams of warm Pacific water having a north-south component in water velocity, implying a small-scale eddy field. Eddies also can be found near ice-edge. The CIOM has the potential to investigate the eddy field in the Beaufort Sea. Nevertheless, a higher resolution model (e.g., 1-km resolution) will be better than the current 3.8-km CIOM. We will implement the nesting approach in the future.

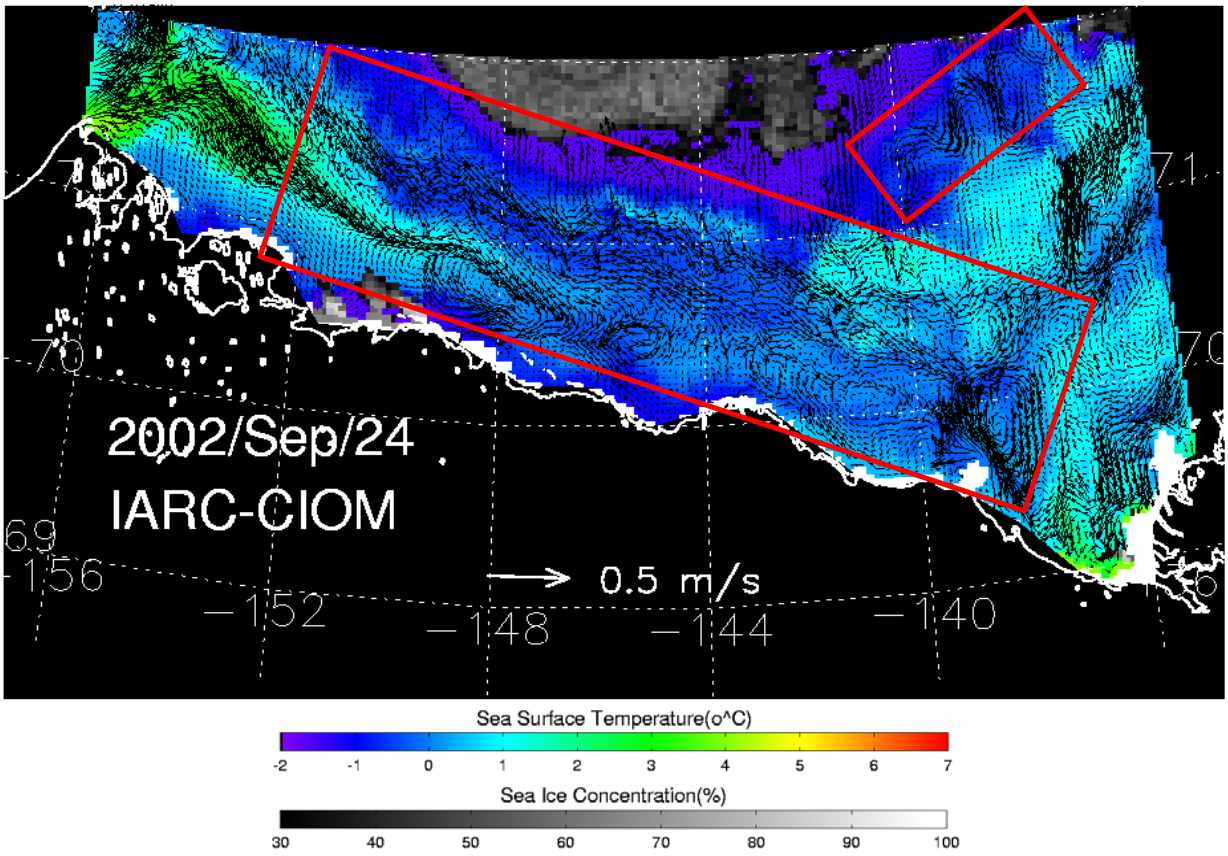


**Figure 27. A snapshot of the CIOM simulation in the Beaufort Sea (September 24, 2002). Black arrows represent water velocity at 10-m water depth at each grid cell.**

## 6. Multiple year (1990-2006) simulations using daily forcing

We have conducted multiple year simulations from 1990 to 2006 to investigate the interannual variability. Summer ice concentration (or open water) in the Alaskan Beaufort Sea measures interannual variability not only in the atmosphere, but also in the ice-ocean system (Wang and Ikeda 2001; Maslanik et al. 2007). Figure 28 shows only the year-to-year spatial variability on August 1 (almost end of melting season) and Figure 29 shows the same on November 14 (freezing season) from 1990 to 1995. There are obvious interannual variabilities in SIC (grey) and SST (color). We can see that there exists landfast ice along the Beaufort coast in 1990, 1991, and 1994, while there are ice free conditions in the same region in 1992, 1993, and 1995 (Fig. 28a).

Wu et al. (2006) and Watanabe et al. (2006) point out that the Arctic Dipole Anomaly (DA), as defined by the second EOF mode of SLP, has more efficient impact on driving sea ice out of Arctic (i.e., driving sea ice from the Western Arctic to the East Arctic) than the Arctic Oscillation (AO, the first EOF mode). The key mechanism here is that DA's wind anomaly is meridional, from Western to Eastern Arctic during positive phase and from East Arctic to Western Arctic during negative phase, while AO's wind anomaly is cyclonic during its positive phase and anticyclonic during its negative phase. Furthermore, the DA's anomaly action region is along the Trans-polar Drift Stream (TDS), adding more sensitivity of sea ice transport to the DA's wind anomaly. Figure 30 shows the first three modes of SLP from a global GCM, called K1 (Watanabe et al. 2006), and NCEP reanalysis. From 1990 to1995, we found that 1990 was a negative DA year, while 1995 was a positive DA year, both indices being larger than one standard deviation. From Figure 28, note that there was more open water in 1995, which was extended all the way along the Canadian Archipelago, than in1990 because of the ice covered conditions in the Canadian Archipelago.

Figure 29 shows the freezing season (November 14) for all six years. Again, there was more open water in 1995 than in 1990 due partly to the preconditioning of the summer open water. It is observed that sea ice freezing in 1994 was faster than in other years. Landfast ice formed not only along the Beaufort coast, but also along the Chukchi coast. During the positive DA year of 1995, there was no landfast ice along the Chukchi coast on November 14, compared to that in 1990 (negative DA year) and other years. Nevertheless, AO also plays an important role when DA is negative. For example, in 1993, there was comparable open water on August 1 than 1995. The reason is that AO index was about 0.75 and DA index was -0.25. The cyclonic anomalous wind stress reduces the strength of the Beaufort Gyre, producing anomalous divergence that

also creates open water in the Alaskan Beaufort coast. Therefore, there is significant interannual variability in both melting and freezing seasons, whereas the DA does play a key role in the interannual variability of sea ice in the study region, while AO-associated divergence in wind stress anomaly is also important when DA is negative.

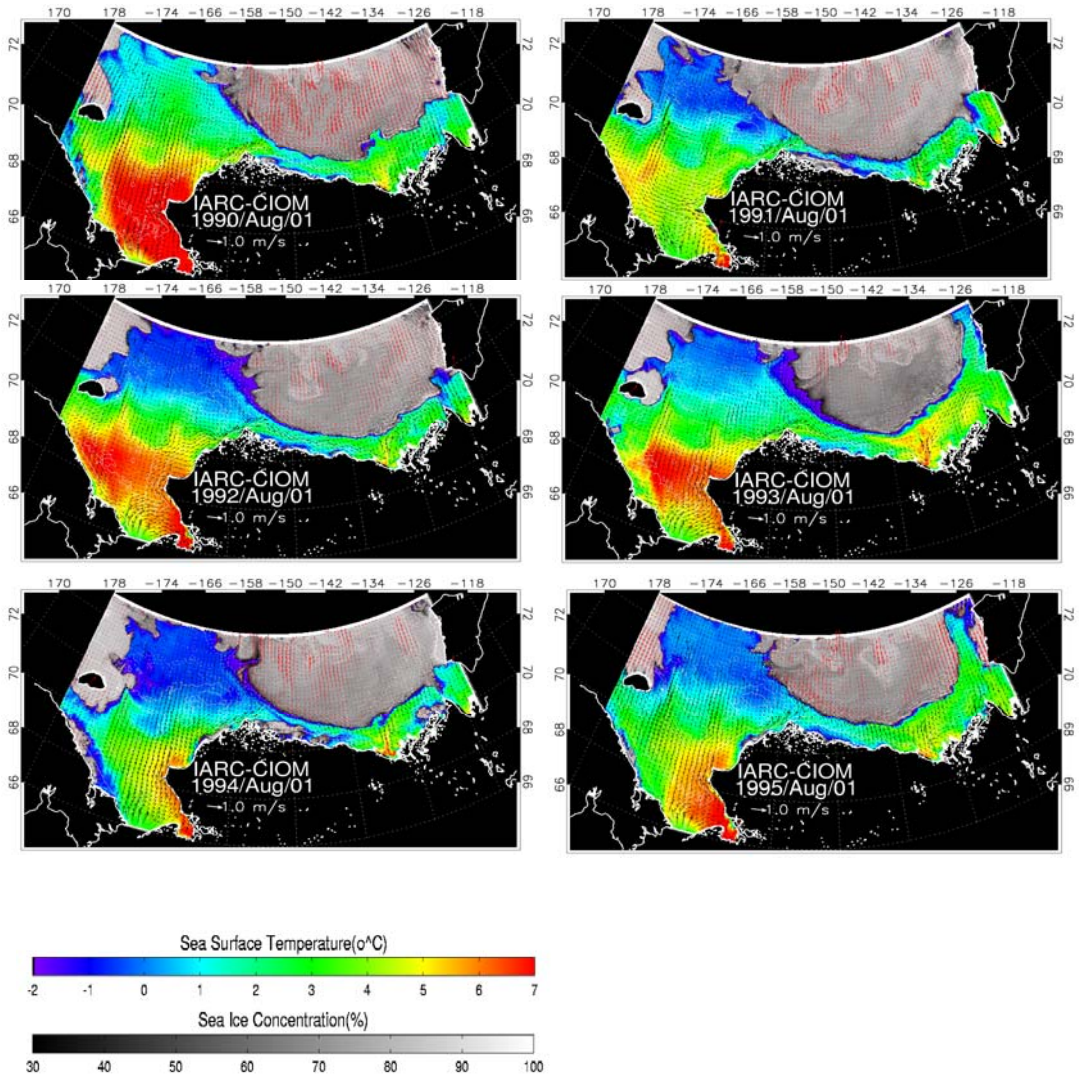


**Figure 28. Sea ice cover and ocean circulation in the Beaufort Sea coastal area on August 1, a melting season, in 1990, 1991, 1992, 1993, 1994, and 1995, simulated by the CIOM. Gray area shows sea ice concentration between 30% and 100%. Black arrows indicate water velocity (10-m water depth), red arrows ice velocity, and areal colors indicate the SST with the same scale of Figure. 29.**

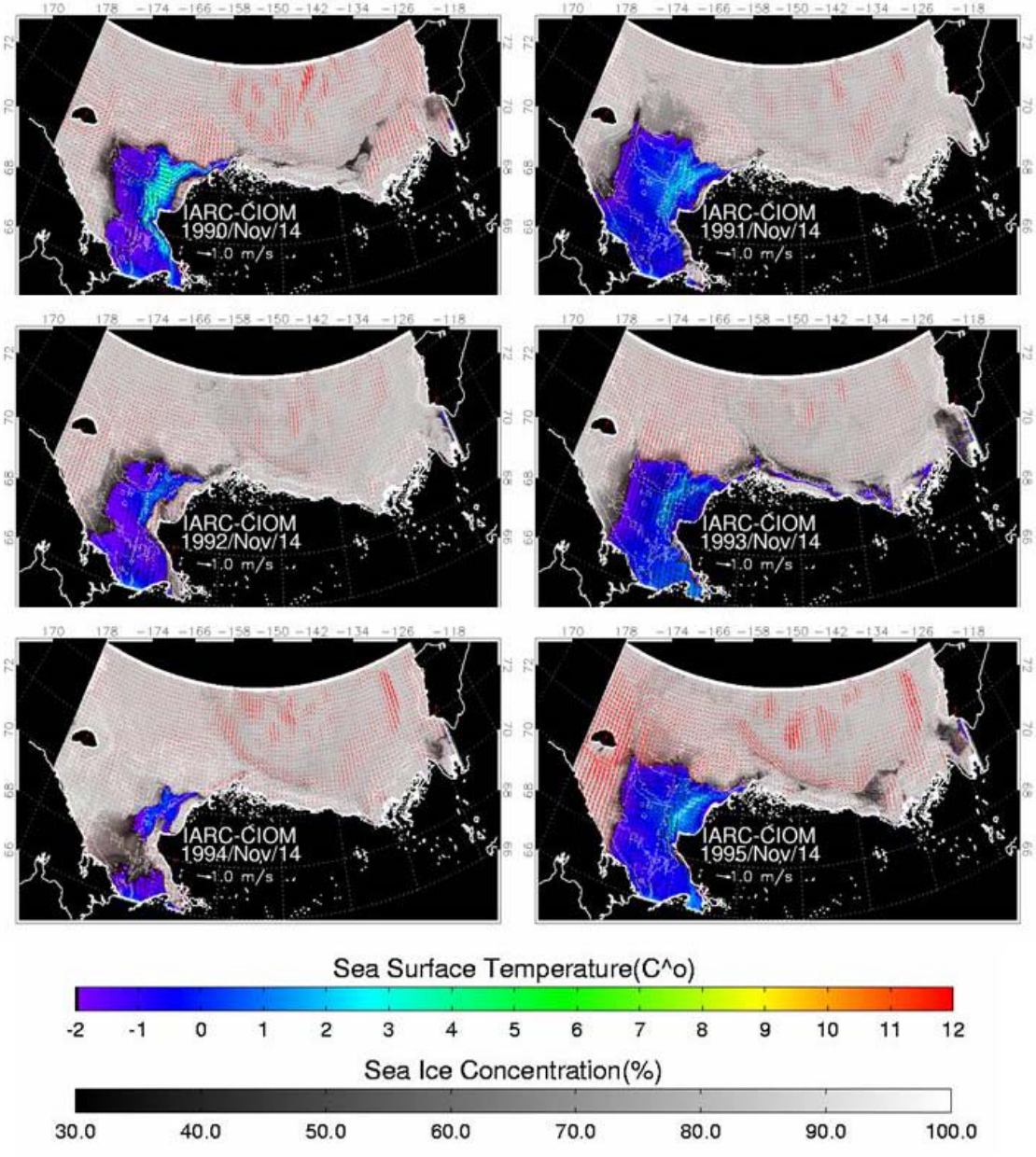


**Figure 29. Same as Figure 28, but for November 14, a freezing season. Gray area means sea ice concentration between 30% and 100%. Black arrows indicate water velocity (10-m water depth), red arrows ice velocity, and areal colors indicate the SST.**

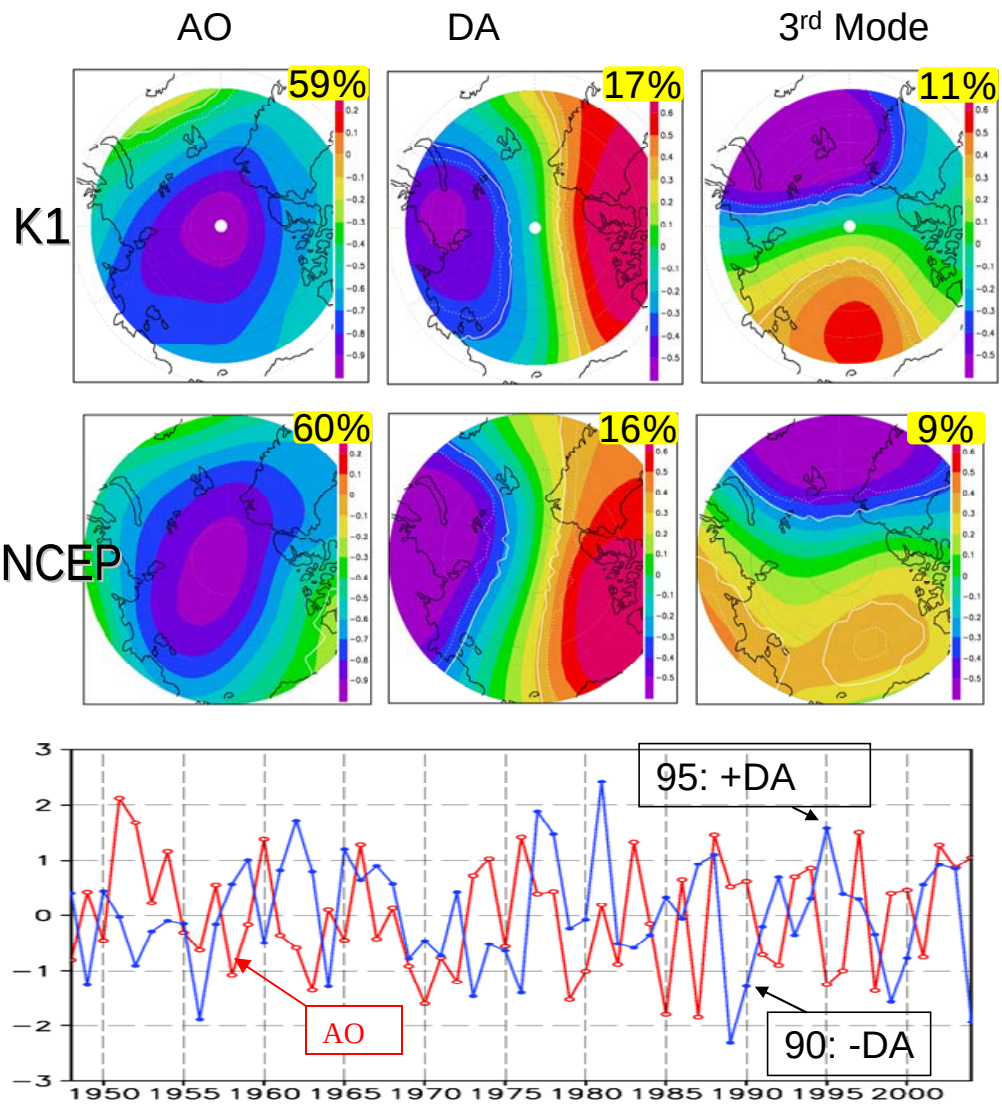


**Figure 30. The EOF analysis of SLP: First mode (AO), second mode (DA), and the third mode derived from a high-resolution global climate model (K1; Watanabe et al. 2006; first row) and NCEP Reanalysis (second row) for period 1948-2004. The lower panel show the AO (in red) and DA's (in blue) eigenvectors (time series) of NCEP reanalysis.**

## 7. Ice-associated oilspill model simulations

An oil spill is a major environmental risk of offshore oil exploration and production. Since we do not know when, where, or how an oil spill will occur, a numerical oil spill trajectory model is an important tool to assess the possible impacts on the environment under various hypothetical oil spill scenarios.

We developed a subgrid-scale, turbulent-dispersion model that includes surface-wind drift, SIC, sea ice flow, and surface current simulated from the circulation model. We used the subgrid model to simulate the surface trajectory of passive particles, based on a previous model that did not consider sea ice impact (Wang 1999; 2001). The Lagrangian motion of a particle in a two-dimensional plane in the presence of a mean flow (u, v), a turbulent velocity (u', v'), and surface wind (Wx, Wy) is described with the following equations:

$$\frac{dx}{dt} = u_{oil} = u + u' + \alpha b W_x ,$$

$$\frac{dy}{dt} = v_{oil} = v + v' + \alpha b W_y ,$$

where x and y are the particle trajectory coordinates at time t after the particle is released at a location ($x_0$, $y_0$) at time ($t_0$). $\alpha$ is the wind factor of 0.025 in our model (typically between 0.02 and 0.03). b is the ice factor, b=1-$C_{ice}$, for normal cases that implies that the oil would adhere to ice and move only with ice, b=1 represents an open water condition, and $C_{ice}$ is ice concentration. The turbulent velocity (u', v') is the complex and inherent motion that occurs at spatial and temporal scales much smaller than the predominant scales of the coastal current and the wind-driven surface current. With sea ice cover, (u', v') will be calculated by only surface current velocity. This velocity is calculated by a random number generator obeying a Gaussian-distribution with a mean of zero and variance of unity. The turbulent velocity has only statistical meaning in contrast to the deterministic large-scale mean flow and wind-driven flow. The random flight model can be described as follows:

$$du' = -\frac{1}{T} u' dt + K^{1/2} dw$$

where T is the turbulent decorrelation time, $K = 2\delta^2 / T$ (or $K=(\Delta x)^2/(2T)$) is the turbulent diffusion coefficient, $\delta$ is the variance of turbulence, and *dw* is the stochastic kick received by the particle. More details on this random flight statistic approach and its applications to atmospheric and oceanic pollution dispersion can be found in Thomson (1986), Dutkiewicz et al. (1993), and Wang (1999, 2001).

The surface current (u, v) can be chosen as sea surface current in open water, ice flow in full ice-cover, or a combination of both. One special case is if oil spill occurs on landfast ice along the Beaufort Sea coast in winter. Then, the oil spill would stay with the ice, and the prediction is much easier as long as the fast ice does not break up before the oil can be removed. Actually, fast ice needs a higher resolution model than our present one to resolve both horizontally and vertically, which is what we plan to do in the next phase. For example, the scale of Barrier Islands is about several to tens of kilometers, which serve as a barrier to anchor landfast ice. So, the simulations in this study only consider oil spill on moving ice or water. In a case in which the ice concentration is between 0 and 1, the oil could be on water, ice, or under ice. The model cannot predict if an oil particle is on water or stuck on or under ice. We assume that the oil spill particles spread evenly in space, so the portion of particles stuck with ice is proportional to ice concentration, and the surface current driving the oil spill can be expressed statically as the combination of sea surface velocity ($u_{water}$, $v_{water}$), and ice velocity ($u_{ice}$, $v_{ice}$) weighed by ice concentration ($C_{ice}$):

$$u = u_{water}(1 - C_{ice}) + u_{ice}C_{ice}$$

$$v = v_{water}(1 - C_{ice}) + v_{ice}C_{ice}$$

Sea surface current and ice velocity fields are very similar, especially at high ice concentration conditions.

We only present two cases in 2002. All the forcings are identical: particles are released on March 15, 2002 on the landfast ice region (grid) off Prudhoe Bay, driven by ocean current and sea ice velocity that are simulated by CIOM using daily NCEP wind forcing. The difference is that case I (Figure 31) has no direct wind forcing on the particles (about 2.5% of the wind speed), while case II (Figure 32) includes the direct wind forcing on the particles.

By April 15 (one month from releasing on the surface of landfast ice), the trajectories mainly stay on the landfast ice surface near the coast, which gives sufficient time for the authority to respond to such a hypothetical oilspill event. The cleaning effort can be conducted on the landfast zone. The worst scenario for cleaning effort is that the oilspill particles are released and trapped at the bottom of the landfast ice, although the oilspill trajectories may be, by and large, similar to those on the surface.

The oilspill particles stay mainly with the landfast ice until July when the landfast ice start to break up and melt. After landfast ice melts, the ocean current plays a major role in advecting the particles. The difference is that with a direct wind effect, the oilspill particles can be advected to the East Siberian coast (Figure 32) before winter arrives, while without the wind effect, the particles are only advected to the Chukchi Sea off Barrow Canyon (Figure 31).

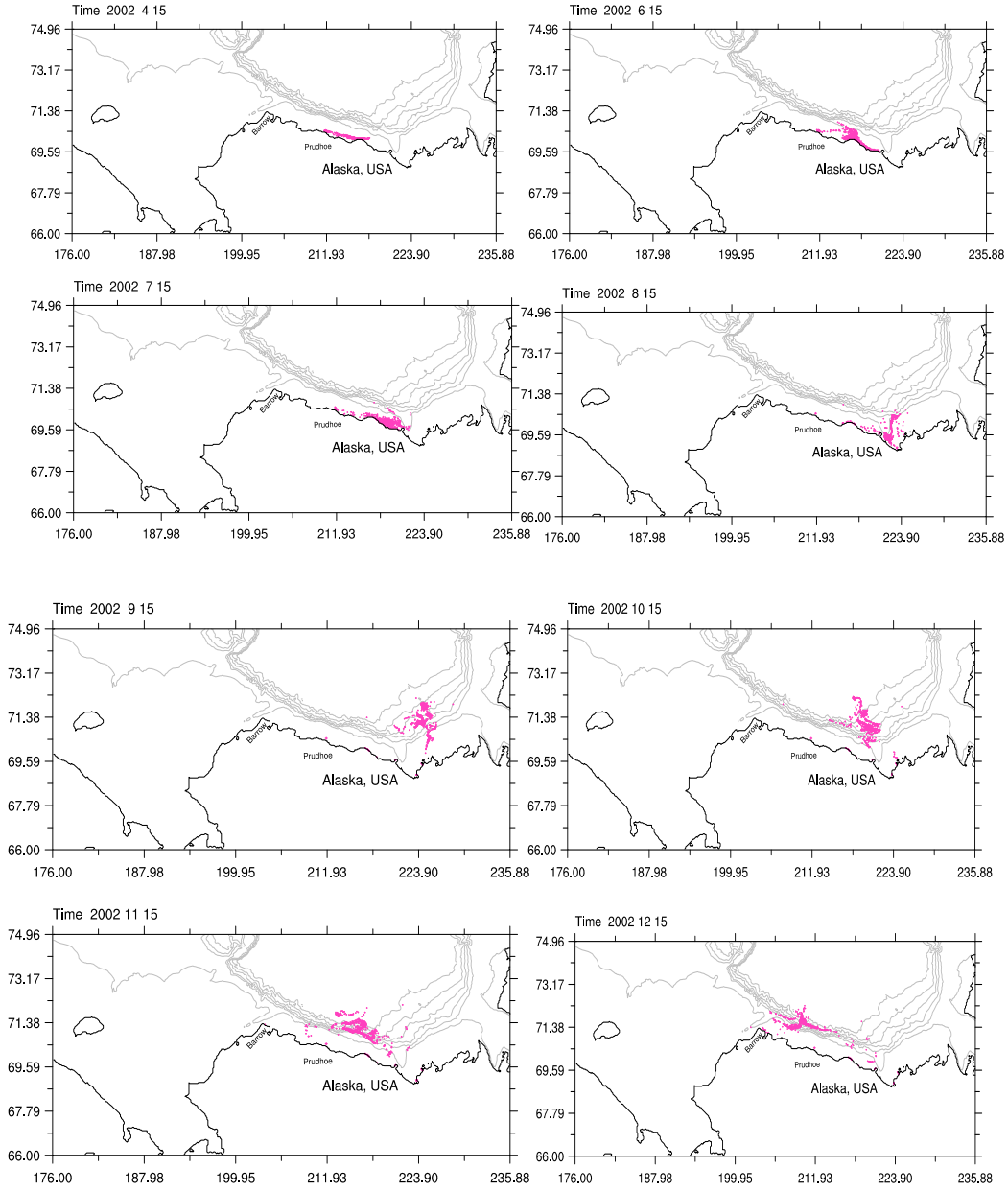


**Figure 31. Oilspill trajectories released off Prudhoe Bay landfast ice on March 15, 2002, driven by the ocean and sea ice current, but with no direct wind contribution to the particles.**

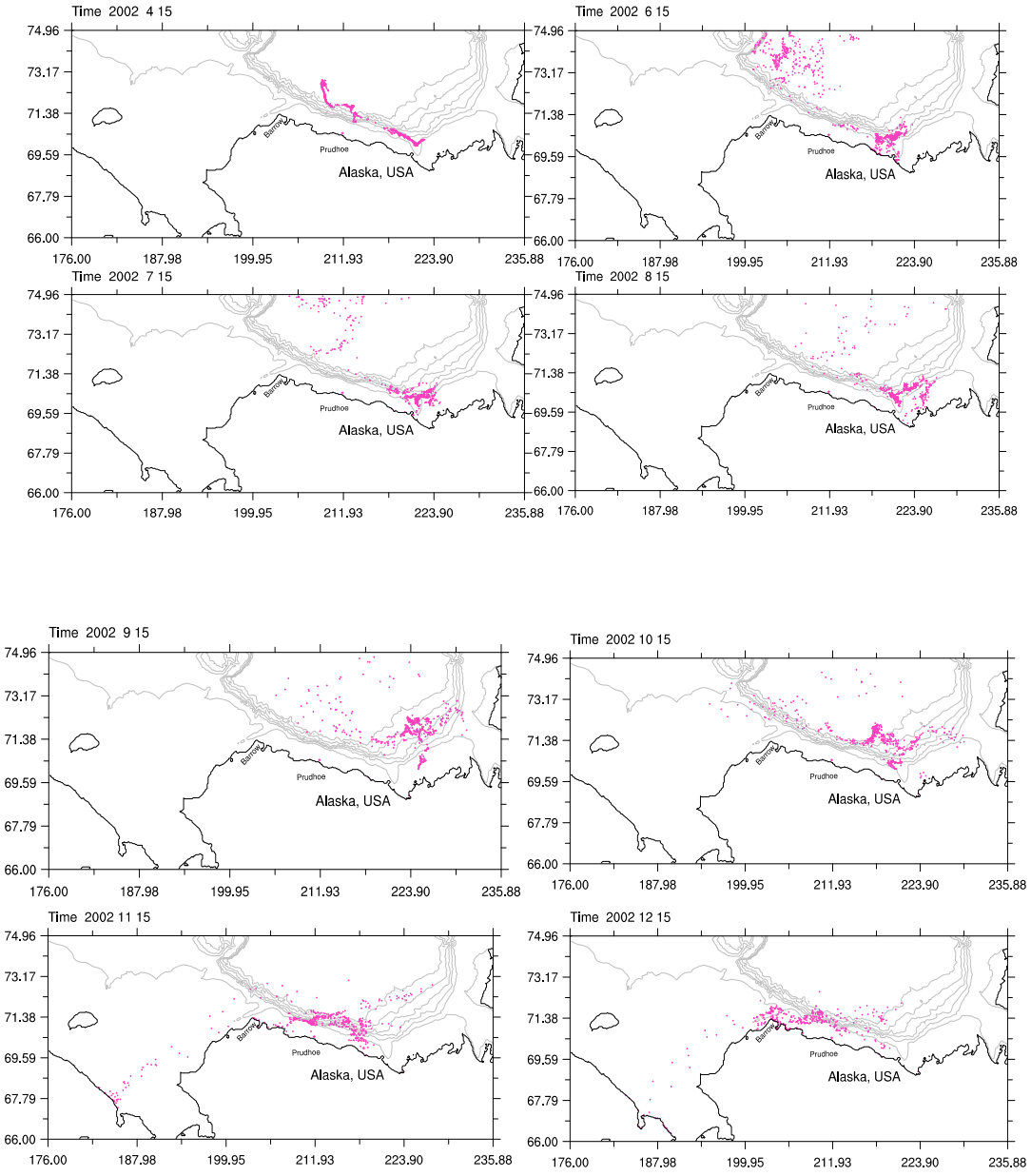


**Figure 32. Oilspill trajectories released off Prudhoe Bay landfast ice on March 15, 2002, driven by the ocean and sea ice current, with direct wind contribution to the particles.**

## 8. Sensitivity studies

We conducted a series of sensitivity studies to investigate different physical processes. We focus on the mechanisms for landfast ice formation, maintenance, and decay along with nearshore circulation and sea ice because we are mostly concerned with sea ice variability in the nearshore Beaufort and Chukchi seas that has a potential impact on nearshore hypothetical oilspill events. The following sensitivity experiments, with year 2002 as control run, were conducted to test the corresponding hypotheses:

1) ***No wind forcing during the growth/freezing (September-December) and decay/melting (May-September) periods of landfast ice:*** The onshore wind component induced by the anticyclonic Beaufort High pressure is the most important factor forming the landfast ice. Note that the onshore winds impose an opposite forcing to the Pacific-Arctic sea-level pressure-head induced Bering Strait inflow (Woodgate et al. 2005). In other words, the onshore winds would slow down the Bering Strait inflow. Thus, without the onshore wind forcing during the formation period, an extreme case of the weakened wind stress, the Bering Strait inflow would be enhanced, advecting more oceanic heat to the Beaufort Sea (Figure 33, upper right). Thus, landfast ice would be reduced in the melting season. However, during the melting season, without the continuous piling-up of sea ice along the coast by onshore wind-pushing, less landfast ice would exist than the control run, consistent with the observation (Mahoney et al. 2007a).

There is no pronounced anomaly during the melting season (Aug. 1, upper right panel of Figure 33) that distinguishes it from the control run. The reason is that the Bering inflow is enhanced without the opposite wind forcing, leading to above-normal melting. However, during the freezing season, without wind forcing, less ice forms along the coast (Figure 34, upper right panel), because the pile-up process is removed. For example, on November 14, 2002, a freezing season for both landfast ice and pack ice, there is little landfast ice formation along the Beaufort coast without the onshore wind forcing derived from the anticyclonic Beaufort Gyre.

2) ***No sea ice advection term:*** We simply turned off the sea ice advection term in the sea ice dynamic equations to test that sea ice dynamics is a key factor. Without the non-linear term, sea ice is controlled by the thermodynamic process.

Without the sea ice advection (or non-linear term), more sea ice and landfast ice exist in the nearshore Beaufort Sea during the melting season (Figure 33, lower left panel) and during the freezing season (Figure 34, lower left panel), compared to the control run. Without the ice advection, landfast ice forms faster than the control run. This indicates that sea ice formation and decay controlled only by the thermodynamic process cannot reproduce open water along the Alaskan Beaufort coast. Thus, sea ice dynamics is not negligible.

3) ***No Bering Strait inflow:*** We simply zeroed the Bering Strait inflow with the same temperature and salinity boundary conditions to investigate the Bering inflow impact on landfast ice and coastal current in the Beaufort and Chukchi seas. The reason is that this inflow advects the warm Bering water (i.e., transports heat) to the Chukchi Sea (Woodgate et al. 2005; Weingartner et al. 2005) and enhances both bottom and lateral melting (Ohshima and Nihashi 2005) all the way to the Beaufort Sea.

Thus, without this inflow, it is assumed that the coastal-trapped current is significantly weakened and thus, the pile-up process by the right-pointing Coriolis force would be reduced. This is why less landfast ice would stay along the Beaufort coast during the melting season (Aug. 1, see Figure 33, lower right panel). The local melting dominates, in particular, near the Mackenzie Delta where the SST is higher than that in the Barrow Canyon area. Nevertheless, in the control run, both the Barrow Canyon area and Mackenzie Delta experience high SST, because in the former, oceanic heating is advected from the Bering inflow.

In contrast, there is a more pronounced impact on sea ice without this inflow during the freezing season. The freezing process is enhanced (Figure 34, lower right panel), because the local cooling dominates thermodynamically in the relatively shallow shelf compared to the advection, while local winds dominate dynamically, leading to enhanced onshore piling-up process (Mahoney et al. 2007).

We also conducted the sensitivity studies of doubling Bering inflow, halving Bering inflow, and annual mean Bering inflow (suggested by Dr. W. Johnson of MMS, personal comm.), which further confirm our finding here.

The following experiments are being conducted (the delay was due to reallocation of J. Wang and K. Mizobata) and will be added to publications submitted to refereed journals:

4) ***No ocean heat advection:*** We simply turned off the ocean temperature advection term (i.e., non-linear term) to test the hypothesis that ocean heat advection contributes significantly to both bottom and lateral melting. Without this term, the landfast ice along the Beaufort Sea shelf would stay over summer.

5) ***No lateral melting processes during the spring-summer period***: From section 4, we hypothesize that without lateral melting, sea ice would stay along the Beaufort coast over summer, because this process is twice as large as bottom melting. Thus, without the lateral melting, we anticipate that sea ice would over-summer the Beaufort coast.

6) ***With ocean tides***: Ocean tides, as high frequency forcing near the inertial (f or Coriolis) frequency in high latitudes, play a crucial role in sea ice ridging and rafting, velocity shear, divergence/convergence, non-linear interactions within sea ice dynamics and with the ocean, and ocean mixing. It is assumed that ocean tides would enhance sea ice dynamic growth through ridging and rafting during the growth season, while they would speed up the melting

during the melting season due to vertical entrainment of warm water beneath the sea ice via tide-induced vertical mixing. We would like to obtain a quantitative dynamic impact of tides on sea ice growth and decay, compared to the control run in terms of percentage.

In summary, wind forcing, ice advection, and Bering inflow all are important to landfast ice formation and stability, and melting along the Beaufort coast, compared to the control run. However, during the melting season when the advected ocean heat is increased, all the factors are involved, leading to very complex picture, i.e., it is difficult to interpret the implicit causes and effects. In contrast, during the freezing season when the oceanic heat flux advection is weakened, the local cooling and wind forcing dominate the landfast formation.

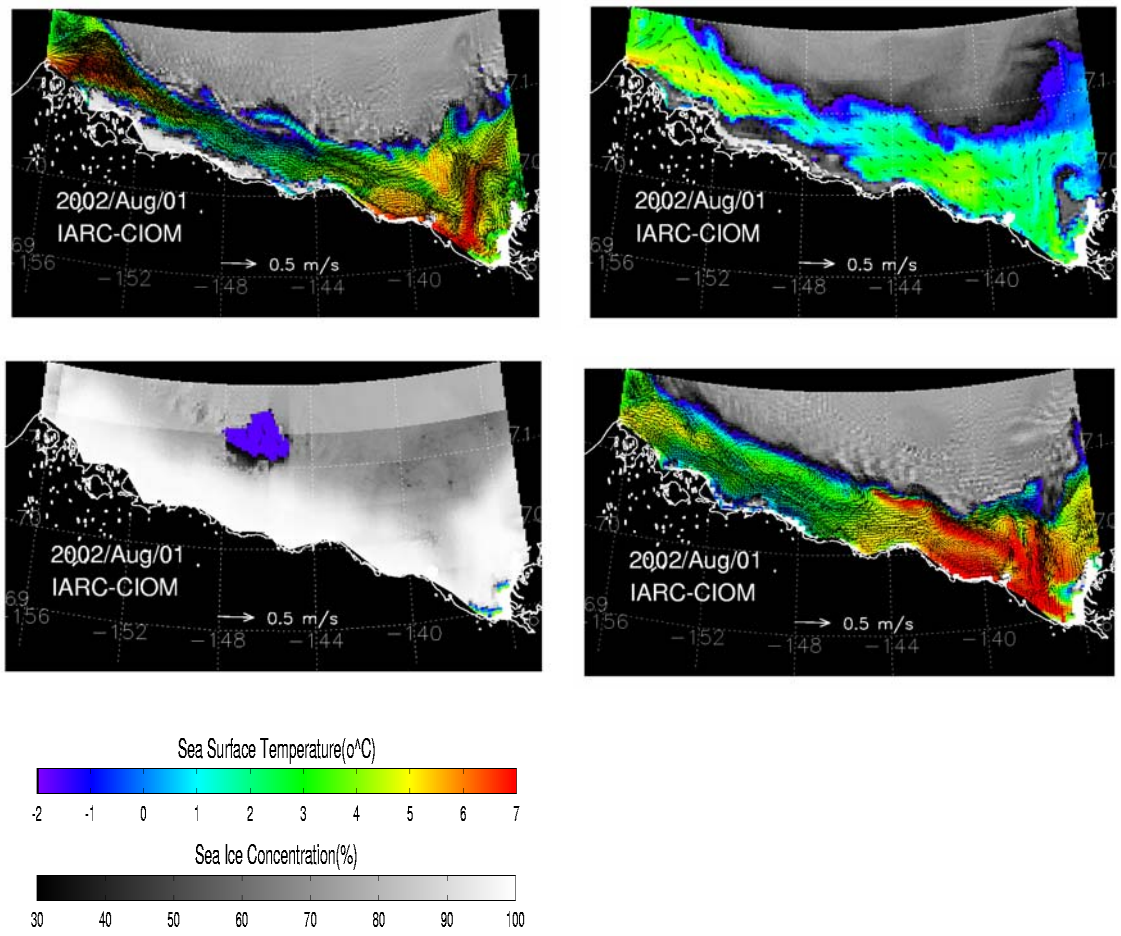


**Figure 33. The CIOM-simulated sea ice concentration during the melting season on August 1, 2002 for 1) the control run (upper left), 2) no wind during the melting season (May-Sep, upper right), 3) no sea ice advection (lower left), and 4) no Bering Strait inflow.**

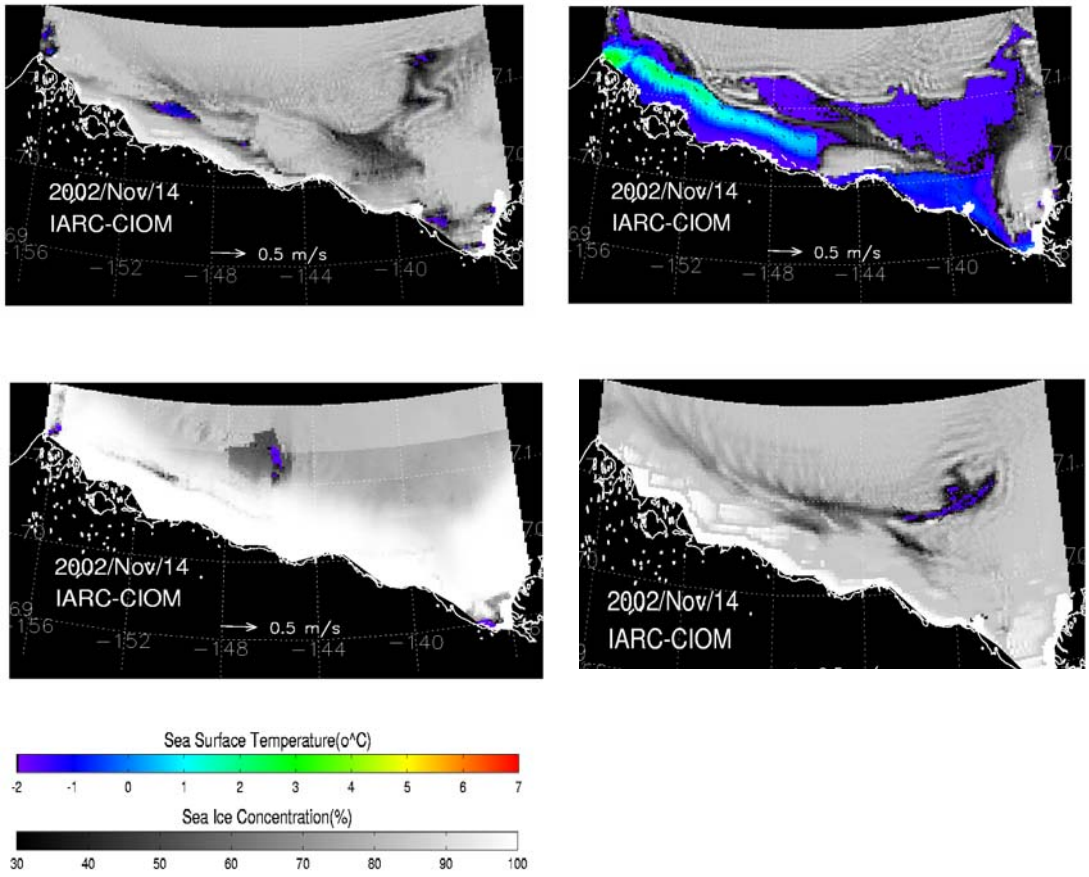


**Figure 34. Same as Figure 33, except for the freezing season on November 14, 2002.**

## 9. Process studies: The Bering Sea inflow and its contribution to volume transports in the Chukchi Sea

Observations show that there is annual Bering inflow of 0.8 Sv via the Bering Strait, which separates into three branches: Barrow Canyon ACW current has ~0.3 Sv, Herald Valley branch has ~0.3 Sv (Woodgate et al. 2005), and the Central Channel branch is of ~0.2 Sv (Weingartner et al. 2005). These transport estimates are based on limited measurements with sparse moorings. Thus, the estimate of the transport using CIOM should be more systematic, and this process study focusing on the Chukchi Sea is CIOM's strength in terms of resolution and coverage, compared to the measurements.

Figure 35 shows the domain that is used to estimate the transports along the three open boundaries. Figure 36 shows the Bering inflow (positive) indicating strong seasonal variation with summer transport being the largest. The Barrow transect also has similar seasonality: strong Barrow Canyon outflow (negative) in summer, and a weak one in other seasons with many reversals (positive) due to wind forcing (Woodgate et al. 2005). The 2002 annual average transports are estimated to be -0.14 (outflow) Sv for the Wrangel section, -1.92 Sv (inflow) for the Northwind section, and 1.12 Sv (outflow) for the Barrow section, respectively, which sums up to be 0.94 Sv. With an inflow of 0.86 Sv from Bering Strait, the error of the transport estimate (0.94 Sv) is about 0.08 Sv, i.e., there is an error of ~10% in the estimate. Our estimates also further confirm the partitioning of the Bering inflow transport into three branches in the Chukchi Sea: ACW current has ~0.08 Sv, Central Channel Current is ~ 0.23 Sv, and Herald Valley Current is ~ 0.39 Sv, consistent with, but differing in quantity from, measurements. Furthermore, our model also estimates an outflow of 0.07 Sv across the Long Strait and an outflow of 0.072 Sv north of Wrangel Island, making up a total outflow of 0.84 Sv, which originates from the Bering Strait inflow of 0.86 Sv. In other words, the model estimate error is only 2%.

Based on the CIOM's estimates (Figures 36-37), we observed that strong seasonal variations exist in the Barrow Canyon outflow, following those in the Bering inflow by one month (Figure 37) consistent with the measurement (Shimada personal commun.), with the Bering inflow being the strongest in summer (Woodgate et al. 2005). Current reversals were found in other seasons. We found little seasonal variation in the Wrangel outflow. We found current reversals in all three branches in the Chukchi Sea, due to the wind forcing. Local wind forcing caused short-term variations, while the Pacific-Arctic pressure-head driven Bering inflow had a seasonal cycle due to the sea-level (i.e., sea-level pressure) seasonal cycle in both the North Pacific and the Arctic Ocean. Land-ocean contrast drove the Pacific-Arctic pressure head. The statistics are shown below:

**Table 2. The statistics for the simulated 2002 annual mean transports.**

| Annual | Bering | Northwind | Wrangel | Barrow |
|---|---|---|---|---|
| Transport (Sv) | 0.86 | -1.92 | -0.14 | 1.12 |
| STDs | 0.28 | 1.15 | 0.11 | 1.15 |
| Max | 1.31 | 4.96 | 0.75 | 0.25 |
| Min | 0.42 | -0.75 | -0.50 | -0.54 |

**Figure 35. The domain and sections in the Chukchi Sea used for estimating volume transports.**

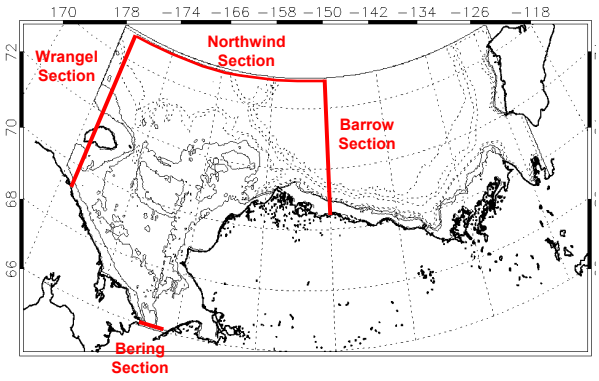

**Figure 36. The 2002 seasonal cycle of volume transport for the Bering inflow (blue diamonds), outflows from Wrangel (black triangles), Northwind (red squares), and Barrow (green crosses) sections (see Fig. 35), respectively. Note that legend "7 per Mov Avg" stands for 7-day moving average.**

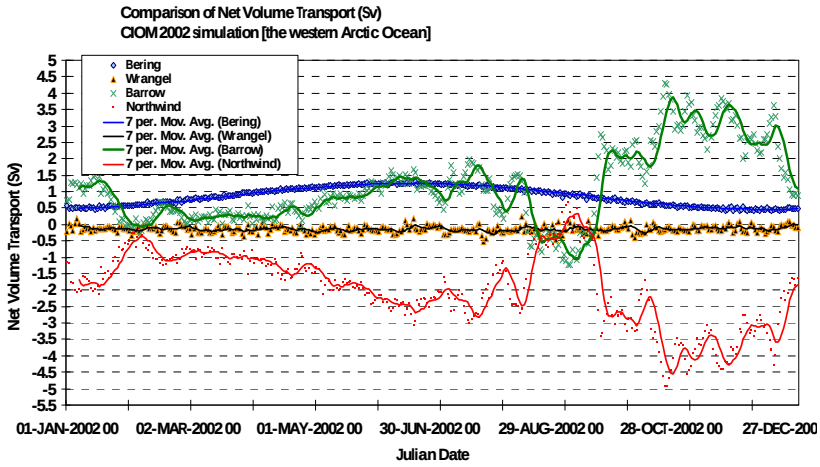


**Figure 37. Seasonal cycle of volume transport of the Bering inflow (red, positive) and the model-estimated volume transport of Barrow section outflow (blue, negative; here a sign change was applied). Note that the Barrow section outflow maximum lags the Bering inflow maximum by about one month.**

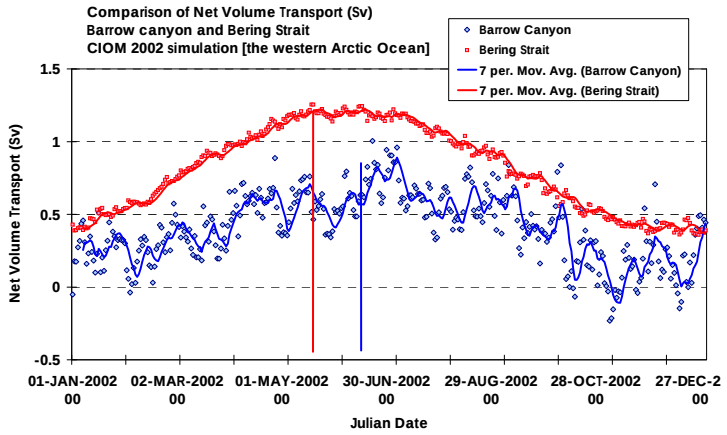

## 10. Conclusions and future efforts

Because of our efforts and also through lessons learned from Phase I, we have successfully improved the CIOM and conducted a realistic simulation for the last three years (Phase II). Simulation results were compared to available ship surveys and satellite measurements.

The major improvements and parameterizations are as follows:

i) modify boundary conditions by combining global GCM outputs with modification using historical data and satellite measurements to conserve transport with radiation property along the open boundaries.

ii) in addition to previous ice-bottom melting processes, a lateral melting parameterization, which is twice as large as the bottom melting, was implemented into this new version of CIOM during the melting season.

iii) Wind-wave mixing parameterization was added to the surface ocean.

Based on the above investigations including the sensitivity studies, the following major conclusions can be drawn:

1) The Chukchi-Beaufort seas coastal current was well reproduced: ACW coastal current, and the other two branches: the Central Channel and Herald Valley. The ESC was also captured with a cold and fresh water mass.
2) The ocean circulation, such as the Beaufort Gyre and the imbedded mesoscale eddies with anticyclones outnumbering cyclones along with the seasonal cycle were very well simulated.
3) The seasonal cycle of sea ice was well reproduced with some discrepancy from the satellite measurements. Without lateral melting, the CIOM produces more sea ice along the Beaufort coast in summer, leading to an excess of sea ice; while with the lateral melting, the sea ice seasonal cycle with ice-free conditions in September along the Beaufort coast was well reproduced.
4) Surprisingly, the landfast ice, for the first time, was reproduced under both monthly and daily atmospheric forcing. Sensitivity experiments suggest the most important factors affecting landfast ice are wind, the Bering inflow, sea ice advection, ocean heat

advection, and the lateral melting process. Tides are weak and less important in modifying landfast ice distribution.

5) Sea ice ridging, cracks, arching, and other downscaling characteristics were captured.

The following important downscaling processes were captured and the corresponding conclusions can be drawn:

6) In the Chukchi Sea, the CIOM captures and reproduces the overwintering of the Bering Inflow water (or Pacific water). The year-to-year accumulation (or change) of the overwintering Pacific water is an important source in melting sea ice in the Western Arctic (Shimada et al. 2006).
7) The summer saline layer was reproduced by CIOM that compares well to the summer observations (Weingartner et al. 1998). Furthermore, our model can explain how this cold, saline layer forms during autumn, winter, and spring when the formation of sea ice injects salt to the upper ocean surface, leading to dense water formation along the shelf (Wang et al. 2004). The dense water cannot sink all the way to the bottom, because of the warmer but still saltier Atlantic water underneath.
8) A strong winter Beaufort High can produce surface Ekman drift, advecting Beaufort Alaska freshwater water originally from the Mackenzie River into the center of the Beaufort Sea. At the same time, the subsurface upwelling due to Ekman pumping (Yang 2006) can bring the Atlantic Water to the surface layer. The CIOM confirms this mechanism.

Nevertheless, the CIOM and SIOMS are far from perfect. As we strive forward, new problems emerge that challenge our capability and model limitations. The following are the problems, challenges, and future efforts we are facing today:

1) High resolution model of the Beaufort Sea coastal area. In the Chukchi and Beaufort Seas, mesoscale, small scale eddies (less than 4~8 km radius) are a ubiquitous feature. The current CIOM has 3.8-km resolution that is still too coarse to resolve small scale eddies. To reveal small eddy dynamics, the CIOM resolution should be increased to ~ 1-2 km. Nevertheless, the 3.8-km sea ice model almost breaks the limit of an isotropic sea ice model. The reason is that we often encountered a similar problem: in some years,

CIOM's sea ice model blows up with no reasonable warning, i.e., sea ice velocity and thickness are normal in previous time step (archive) before it suddenly blows up. When the resolution is reduced to 1 km, the isotropic limit is anticipated to break down. Furthermore, model integration would demand more computing resources. Thus, an anisotropic model should be used or an alternative sea ice model such as a granular Lagrangian model may be used, which, nevertheless, still has its intrinsic problem.

2) A sea ice melting scheme, including melt ponds in summer that have been confirmed to be a factor speeding up the melting process (Inoue et al. 2006), is an important positive feedback between the sea ice and ocean.
3) Replace the present VP ice model with EVP ice model.
4) Ship-based survey. To validate the CIOM, the present in-situ data are not sufficient. During the IPY (International Polar Year 2007-2009), we will join three cruises to collect more hydrographic data. In 2007, we joined the T/S *Oshoro-Maru* (Hokkaido University, Japan) summer cruises in the Chukchi Sea. We will also join the R/V *Mirai* cruise and other cruises in the western Arctic Ocean in 2008.
5) Data assimilation. To achieve more realistic 3-D simulation results, we plan to conduct near real-time data assimilation starting with the nudging method (Wang 2001). We will assimilate satellite measurements (sea surface temperature, sea ice concentration, and sea level anomaly) and in-situ measurements, if possible.
6) Implementation of the ecosystem model. The CIOM has reproduced oceanic circulation in the Chukchi and Beaufort Seas, even though the ice model needs to be improved. We will couple an ecosystem model to the CIOM, for understanding dynamics of lower trophic levels (e.g., phytoplankton, zooplankton).

## Acknowledgments

We are sincerely thankful for support from the University of Alaska Costal Marine Institute (CMI) and Minerals Management Service (MMS) and IARC/JAMSTEC Cooperative Agreement. JW wants to thank Drs. Dick Prentki and Walter Johnson of MMS for valuable guidance and for discussion during the course of this research. Thanks also go to Drs. Ron Lai and Caryn Smith of MMS for their inputs. JW also wants to thank Dr. Vera Alexander, former CMI director, for providing research vision in the Beaufort and Chukchi seas. This is NOAA GLERL Contribution No. 1475.

## References

Blumberg, A.F. and G.L. Mellor. 1987. A description of 3-D coastal ocean circulation model. In Heaps, N.S. (Ed.), Coastal and Estuarine Sciences 4: 3-D Coastal Ocean Models. American Geophysical Union, Washington DC, pp 1-16.

Cavalieri, D., P. Gloersen, and J. Zwally. 1990. DMSP SSM/I daily and monthly polar gridded sea ice concentrations, [1990 Jan 1st to 2006 December 31st ]. Edited by J. Maslanik and J. Stroeve. Boulder, Colorado USA: National Snow and Ice Data Center. Digital media.

Chao, S.-Y. and P.-T. Shaw. 2002. A numerical investigation of slanted convection and subsurface anticyclone generation in an Arctic baroclinic current system. *J. Geophys. Res.,*107(C3), 3019, doi:10.1029/2001JC000786.

Comiso, J. 1990. DMSP SSM/I daily and monthly polar gridded sea ice concentrations. Edited by J. Maslanik and J. Stroeve. Boulder, Colorado USA: National Snow and Ice Data Center. Digital media.

Dutkiewicz, S., A. Griffa, and D.B. Olson. 1993. Particle diffusion in a meandering jet. *J. Geophys. Res.*, 98, 16487-16500.

Eicken, H., L.H. Shapiro, A.G. Gaylord, A. Mahoney, and P.W. Cotter. 2005. Mapping and characterization of recurring spring leads and landfast ice in the Beaufort and Chukchi seas. U.S., Department of Interior, Minerals Management Service (MMS), Alaska Outer Continental Shelf Region. Anchorage, Alaska, 141 pp.

Ford, J.M., J. Wang, and R.T. Cheng. 1990. Predicting the vertical structure of tidal current and salinity in San Francisco Bay, California. *Water Resources Res*., 26(5): 1,027-1,045.

Fu, G., K.S. Baith, and C.R. McClain. 1998. "SeaDAS: The SeaWiFS Data Analysis System," Proceedings of "The 4th Pacific Ocean Remote Sensing Conference." Qingdao, China, July 28-31, 1998, pp 73-79.

Grebmeier, J.M., J.E. Overland, S.E. Moore, E.V. Farley, E.C. Carmack, L.W. Cooper, K.E. Frey, J.H. Helle, F.A. McLaughlin, and S.L. McNutt. 2006. A major ecosystem shift in the Northern Bering Sea. Science, doi: 10.1126/science.1121365, **311**, 1461-1464.

Hibler, W.D. III. 1979. A dynamic and thermodynamic sea ice model. *J. Phys. Oceanogr*., 9, 15,959-15,969.

Hibler, W.D. III. 1980. Modeling a variable thickness sea ice cover*. Mon. Wea. Rev., 108,* 1943-1973.

Hibler, III, W.D. and K. Bryan. 1987. A diagnostic ice-ocean model. *J. Phys. Oceanogr., 17,* 987-1015.

Hu, H. and J. Wang. 2008. Modeling the ocean circulation in the Bering Sea. *Ocean Modeling* (under revision).

Hunke, E. C. and J. K. Dukowicz. 1997. An elastic-viscous-plastic model for sea ice dynamics. *J. Phys. Oceanogr*., 27, 1849-1867.

Inoue, J., T. Kikuchi, D.K. Perovich, J.H. Morison. 2005. A drop in mid-summer shortwave radiation induced by changes in the ice-surface condition in the central Arctic. *Geophys. Res. Lett.*, 32 (13): Art. No. L13603.

Kantha, L.H. and G.L. Mellor. 1989. Application of a two-dimensional coupled ocean-ice model to the Bering Sea marginal ice zone. *J. Geophys. Res., 94*, 10,921-10,936.

Kantha, L.H. and C.A. Clayson. 1994. An improved mixed layer model for geophysical applications. *J. Geophys. Res*., 99(C12), 25,235-25,266.

Kowalik, Z. and A. Proshutinsky. 1994. The Arctic Ocean Tides, In: The Polar Oceans and Their Role in Shaping the Global Environment: Nansen Centennial Volume. *Geoph. Monograph* 85, AGU, pp 137-158.

Mahoney, A., H. Eicken, A.G. Gaylord, and L. Shapiro. 2007a. Alaska landfast sea ice: Links with bathymetry and atmospheric circulation. *J. Geophys. Res.*, 112, C02001, doi:10.1029/2006JC003559.

Mahoney, A., H. Eicken, and L. Shapiro. 2007b. How fast is landfast ice? A study of the attachment and detachment of nearshore ice at Barrow, Alaska. *Cold Regions Science and Technology*, 47, 233-255.

Manley, T.O. and K. Hunkins. 1985. Mesoscale eddies of the Arctic Ocean. *J. Geophys. Res*. 90:4911–4930.

Maslanik, J., S. Drobot, C. Fowler, W. Emery, and R. Barry. 2007. On the Arctic climate paradox and the continuing role of atmospheric circulation in affecting sea ice conditions. *Geophys. Res. Lett.*, 34 (3): Art. No. L03711.

Melling, H. 1993. The formation of a haline shelf front in wintertime in an ice-covered sea. *Continen. Shelf. Res.,* 13, 1123-1147

Mellor, G.L. 2004. Users guide for a 3-D, primitive equation, numerical ocean model. Atmospheric and Oceanic Sciences Program, Princeton Univ. (Princeton, NJ 08540), 39 pp.

Mellor, G.L. and L. Kantha. 1989. An ice-ocean coupled model. *J. Geophys. Res., 94*, 10,937-10,954.

Mizobata, K., S.-I. Saitoh, and J. Wang. 2008. Summer biological enhancement in relation to the mesoscale eddy at the shelf break in the vicinity of the Pribilof Islands. *Deep Sea Res.* II, doi:10.1016/j.dsr2.2008.03.002

Muench R.D., J.T. Gunn, T.E. Whitledge, P. Schlosser, and W. Smethie. 2002. An Arctic Ocean cold core eddy. *J. Geophys. Res.*, 105 (C10): 23,997-24,006.

Münchow, A. and E.C. Carmack. 1997. Synoptic flow and density observations near an arctic shelf break. *J. Phys. Oceanogr., 27*, 1402–1419.

Nihoul, J.C.J, P. Adam, P. Brasseur, E. Deleersnijder, S. Djenidi, and J. Haus. 1993. Three-dimensional general circulation model of the northern Bering Sea's summer ecohydrodynamics. *Continen. Shelf Res.,13*, 509-542.

Ohshima, K.I. and S. Nihashi. 2005. A simple ice-ocean coupled model for the Antarctic ice melt season. *J. Phys. Oceanogr*., 35, 188-201.

Pickart, R.S. 2004. Shelfbreak circulation in the Alaska Beaufort Sea: Mean structure and variability. *J. Geophys. Res.,* 109, C04024 doi: 10.1029/2003JC001912.

Pickart, R.S., T.J. Weingartner, L.J. Pratt, S. Zimmermann, and D.J. Torres. 2005. Flow of winter-transformed Pacific water into the Western Arctic. *Deep-Sea Res*., Part II, 52 (24-26): 3175-3198.

Shimada, K., T. Kamoshida, M. Itoh, S. Nishino, E. Carmack, F. McLaughlin, S. Zimmermann, and A. Proshutinsky. 2006. Pacific Ocean inflow: Influence on catastrophic reduction of sea ice cover in the Arctic Ocean. *Geophys. Res. Lett.*, 33, L08605, doi:10.1029/2005GL025624.

Shuert, P.G. and J.J. Walsh. 1993. A coupled physical-biological model of the Bering-Chukchi seas. *Continen. Shelf Res.,13*, 543-573.

Steele, M., R. Rebecca, and W. Ermold. 2001. PHC: A global ocean hydrography with a high-quality Arctic Ocean. *J. Climate, 14,* 2079-2087.

Thorndike, A.S., D.A. Rothrock, G.A. Maykut, and R. Colony. 1975. The thickness distribution of sea ice. *J. Geophys. Res*., 80, 4,501-4,513

Thomson, D.J. 1987. Criteria for selection of stochastic models of particle trajectories in turbulent flow. *J. Fluid Mech*. 180:529–556.

Vazquez et al. 1998. "NOAA/NASA AVHRR Oceans Pathfinder Sea Surface Temperature Data Set User's Reference Manual Version 4.0." 10 April 1998, JPL Publication D-14070.

Wang, J., L.A. Mysak, and R.G. Ingram. 1994a. A numerical simulation of sea-ice cover in Hudson Bay, *J. Phys. Oceanogr., 24,* 2515-253.

Wang, J, L.A. Mysak, and R.G. Ingram. 1994b. Interannual variability of sea-ice cover in Hudson Bay, Baffin Bay and the Labrador Sea. *Atmosphere-Ocean*, *32(2):* 421-447.

Wang, J. 1998. A two-channel laterally averaged estuarine circulation model (LAECIM). *J. Geophys. Res*., 103: 18,381-18,391.

Wang, J. 1999. A nowcast/forecast system for coastal ocean circulation (NFSCOC). International Arctic Research Center-Frontier Research System for Global Change. IARC/Frontier Tech. Rep. No. 99-1. University of Alaska Fairbanks, 97 pp.

Wang, J., V. Patrick, J. Allen, S. Vaughan, C.N.K. Mooers, and M. Jin. 1999. Modeling seasonal ocean circulation of Prince William Sound, Alaska using freshwater of a line source. In *Coastal Engineering and Marina Development*, eds. C.A. Brebbia and P. Anagnostopoulos. WIT Press, Southampton-Boston, pp 55-66.

Wang, J. and M. Ikeda. 1997. Diagnosing ocean unstable baroclinic waves and meanders using quasi-geostrophic equations and Q-vector method. *J. Phys. Oceanogr*. 27(6): 1158-1172.

Wang, J. and M. Ikeda. 2000. Arctic Oscillation and Arctic Sea-Ice Oscillation. *Geophys. Res. Lett.* 27, 1287-1290.

Wang, J. 2001. A nowcast/forecast system for coastal ocean circulation (NFSCOC) with a simple nudging data assimilation. *Journal of Atmospheric Oceanic Technology,18(*6), 1037-1047.

Wang, J. and M. Ikeda. 2001. Arctic Sea-Ice Oscillation: Regional and seasonal perspectives. *Annals of Glaciology*, *33*, 481-492.

Wang, J., M. Jin, V. Patrick, J. Allen, D. Eslinger, C. Mooers and T. Cooney. 2001a. Numerical simulation of the seasonal ocean circulation patterns and thermohaline structure of Prince William Sound, Alaska. *Fisheries Oceanogr., 10 (*Suppl. 1), 132-148.

Wang, J., Q. Liu, M. Jin. 2001b. A nested coupled ice-ocean model for the Beaufort Sea. Annual Report No. 8. University of Alaska, MMS/Alaska OCS Region. Anchorage, Dept. of the Interior, pp 80-94.

Wang, J., Q. Liu, and M. Jin. 2002a. A User's Guide for a Coupled Ice-Ocean Model (*CIOM*) in the Pan-Arctic and North Atlantic Oceans. International Arctic Research Center-Frontier Research System for Global Change, Tech. Rep. 02-01, 65 pp.

Wang, J., Q. Liu, and M. Jin. 2002b. A nested coupled ice-ocean model for the Beaufort Sea. Annual Report No. 8. University of Alaska, MMS/Alaska OCS Region, Anchorage, Dept. of the Interior, pp 80-94.

Wang, J. 2003. Proceedings of a Workshop on Small-Scale Sea-Ice and Ocean Modeling (SIOM) in the Nearshore Beaufort and Chukchi Seas. Final Report, Coastal Marine Institute, University of Alaska, OCS Study MMS 2003-043, 56pp.

Wang, J., M. Jin, M. Ikeda, K. Shimada, and J. Takahashi. 2003a. Validation of a nested coupled ice-ocean model in the Beaufort Sea. Annual Report No. 9. University of Alaska, MMS/Alaska OCS Region, Anchorage, Dept. of the Interior, pp 19-31.

Wang, J., R. Kwok, F.J. Saucier, J. Hutchings, M. Ikeda, W. Hibler III, J. Haapala, M.D. Coon, H.E.M. Meier, H. Eicken, N. Tanaka, R. Prentki, and W. Johnson. 2003b. Working towards improved small-scale sea ice and ocean modeling in the Arctic seas. *EOS*, AGU, Vol . 84 (34), 325, 329-330.

Wang, J., M. Ikeda and F. Saucier. 2003c. A theoretical, two-layer, reduced-gravity model for descending dense water flow on continental slopes. *J. Geophys. Res.,* 108(C5), 3161, doi: 10.1029/2000JC000517.

Wang, J., M. Jin, M. Ikeda, K. Shimada, and J. Takahashi. 2003d. The validation of a nested coupled ice-ocean model in the Beaufort Sea. Annual Report No. 9. University of Alaska, MMS/Alaska OCS Region, Anchorage, Dept. of the Interior.

Wang, J., B. Wu, C. Tang, J.E. Walsh, and M. Ikeda. 2004. Seesaw structure of subsurface temperature anomalies between the Barents Sea and the Labrador Sea. *Geophys. Res. Lett., 31*, L19301, doi: 10.1029/2004GL019981.

Wang, J., Q. Liu, M. Jin, M. Ikeda and F.J. Saucier. 2005. A coupled ice-ocean model in the pan-Arctic and the northern North Atlantic Ocean: Simulation of seasonal cycles. *J. Oceanogr*., 61, 213-233.

Wang, J., H. Hu, K. Mizobata, and S. Saitoh. 2008. Seasonal variations of sea ice and ocean circulation in the Bering Sea: A model-data fusion study. *J. Geophys. Res.* (accepted with revision)

Watanabe, E., J. Wang, T. Sumi, and H. Hasumi. 2006. Arctic Dipole and its contribution to sea ice export from the Arctic in the last 20th century. *Geophys. Res. Lett*., 33, L23703, doi:10.1029/2006GL028112.

Weingartner, T.J., D.J. Cavalieri, K. Aagaard, and Y. Sasaki. 1998. Circulation, dense water formation, and outflow on northeast Chukchi shelf. *J. Geophys. Res.,* 103, 7647-7661.

Weingartner, T.J., S. Danielson, Y. Sasaki, V. Pavlov, and M. Kulakov. 1999. The Siberian Coastal Current: a wind and buoyancy-forced arctic coastal current. *J. Geophys Res.*, 104: 29,697–29,713.

Weingartner, T.J., K. Aagaard, R. Woodgate, S. Danielson, Y. Sasaki, and D.J. Cavalieri. 2005. Circulation on the north central Chukchi Sea shelf. *Deep Sea Res. II,* 3150-3174.

Winsor, P. and D. Chapman. 2004. Pathways of Pacific water across the Chukchi Sea: A numerical model study. *J. Geophys. Res.*, 109, C03002, doi:10.1029/2003JC001962.

Woodgate, R., T.J. Weingartner, and K. Aagaard, 2005. A year in the physical oceanography of the Chukchi Sea: Moored measurements from autumn 1990-1991. *Deep Sea Res. II,* 3116-3149.

Wu, B., J. Wang, and R. Zhang. 2004. Effects of intraseasonal variations of the Arctic Oscillation on the Barents Sea. *Polar Meteorolo. Glaciol*., 18, 82-95.

Wu, B., J. Wang, and J.E. Walsh. 2006. Dipole anomaly in the winter Arctic atmosphere and its association with Arctic sea ice motion. *J. Clim., 19(2), 210-225. DOI: 10.1175/JCLI3619.1*

Yang, J. 2006. The seasonal variability of the Arctic Ocean Ekman transport and its role in the mixed layer heat and salt fluxes. *J. Clim.*, 19, 5366-5387.

Yao, T., C.L. Tang, and I.K. Peterson. 2000. Modeling the seasonal variation of sea ice in the Labrador Sea with a coupled multi-category ice model and the Princeton Ocean Model. *J. Geophys. Res*., 105 (C1), 1153-1165.

Zhang, X., J.E. Walsh, J. Zhang, U.S. Bhatt, and M. Ikeda. 2004. Climatology and interannual variability of Arctic cyclone activity, 1948-2002. *J. Clim.* 17: 2300-2317.


**The Department of the Interior Mission**

As the Nation's principal conservation agency, the Department of the Interior has responsibility for most of our nationally owned public lands and natural resources. This includes fostering sound use of our land and water resources; protecting our fish, wildlife, and biological diversity; preserving the environmental and cultural values of our national parks and historical places; and providing for the enjoyment of life through outdoor recreation. The Department assesses our energy and mineral resources and works to ensure that their development is in the best interests of all our people by encouraging stewardship and citizen participation in their care. The Department also has a major responsibility for American Indian reservation communities and for people who live in island territories under U.S. administration.


**The Minerals Management Service Mission**

As a bureau of the Department of the Interior, the Minerals Management Service's (MMS) primary responsibilities are to manage the mineral resources located on the Nation's Outer Continental Shelf (OCS), collect revenue from the Federal OCS and onshore Federal and Indian lands, and distribute those revenues.

Moreover, in working to meet its responsibilities, the **Offshore Minerals Management Program** administers the OCS competitive leasing program and oversees the safe and environmentally sound exploration and production of our Nation's offshore natural gas, oil and other mineral resources. The MMS **Royalty Management Program** meets its responsibilities by ensuring the efficient, timely and accurate collection and disbursement of revenue from mineral leasing and production due to Indian tribes and allottees, States and the U.S. Treasury.

The MMS strives to fulfill its responsibilities through the general guiding principals of: (1) being responsive to the public's concerns and interests by maintaining a dialogue with all potentially affected parties and (2) carrying out its programs with an emphasis on working to enhance the quality of life for all Americans by lending MMS assistance and expertise to economic development and environmental protection.